EXPERIMENTAL EVALUATION OF ASYMMETRIC BLEED ACTUATION FOR ROTATING STALL AND SURGE CONTROL

by

AHMED FAHIM

Ingénieur Civil Mécanicien et Electricien,
Diplomé de l'Ecole Polytechnique de l'Université Libre de Bruxelles, 1996

Submitted to the Department of Aeronautics and Astronautics
in partial fulfillment of the requirements for the degree of

MASTER OF SCIENCE IN AERONAUTICS AND ASTRONAUTICS

at the

MASSACHUSETTS INSTITUTE OF TECHNOLOGY

February 1998

© Massachusetts Institute of Technology 1998. All rights reserved.

Author ______________________________
Department of Aeronautics and Astronautics
January 6, 1998

Certified by ______________________________
Professor James D. Paduano
C. R. Sodberg Associate Professor of Aeronautics and Astronautics
Thesis Supervisor

Accepted by ______________________________
Professor Jaime Peraire
Associate Professor of Aeronautics and Astronautics
Chair, Graduate Office

MAR 09 1998

LIBRARIES

EXPERIMENTAL EVALUATION OF ASYMMETRIC BLEED ACTUATION FOR ROTATING STALL AND SURGE CONTROL

by

AHMED FAHIM

Submitted to the Department of Aeronautics and Astronautics
on January 6, 1998, in partial fulfillment of the
requirements for the degree of
Master of Science in Aeronautics and Astronautics

ABSTRACT

Active control concepts using compressor exit bleed valves were studied and experimentally tested on a high-B multi-stage compressor. Actuation consisted of a moderate number (four) of circumferentially distributed bleed valves. The effectiveness of the bleed valves was improved by the use of a long downstream duct added to the existing compression system. A non-linear model with distortion included was developed and used to assess the high bandwidth requirement (50 Hz.) as well as the duct length (3 ft.) necessary for the purpose of control. The downstream duct and the high-speed bleed valves were then designed, tested and implemented on the system with results matching the design requirements. Based on a two-dimensional version of the Moore-Greitzer compressor model modified with the addition of the two-dimensional bleed actuation, sensor location (hot-wires) upstream of the actuation was implemented. System transfer function measurements were taken and successfully validated the model. Forced response of the first harmonic demonstrated the quantitative 2D effect of the actuation. A proportional control system on the first harmonic was tested. It significantly damped the first mode and 3% range extension was achieved. Recommendations for future research conclude this thesis.

Thesis Supervisor: Professor James D. Paduano
Title: C. R. Sodberg Associate Professor of Aeronautics and Astronautics

ACKNOWLEDGMENTS

First, I wish to thank my family for giving me their support throughout my stay in the United States, far from home but close to my heart.

I would like to thank my advisor, Professor Paduano, for expressing his confidence and offering me this project. His knowledge and capacity throughout this work were invaluable. I also wish to thank Professor Epstein who gave me valuable advice for the important design part of this work.

I am also indebted to John Protz and Shengfang Liao for their unmeasurable help throughout this research.

Victor Dubrowski, Mike Hutt, Al Chandler, Jimmy Letendre and Bill Ames helped me so much in advice, hardware assembly and constructions that I would like to thank them for their great and nice assistance.

I must also thank all of the students and staff of the GTL for making the work here that much more enjoyable.

Finally, these thanks would not be complete if I did not add particular thanks to Fabienne, Omar, Leo, Arnaud and last but not least, the Mousquetaires, Jacques, Jeremie and Stephane, for making my MIT experience much more than academic.

This project was supported by a Fellowship of the Belgian American Educational Foundation (B.A.E.F.) and by AFSOR grant #F49620-95-1-0409 managed by Dr. Marc Jacobs. These supports are gratefully acknowledged.

CONTENTS

List of Figures 11

List of Tables 15

1 Introduction 17

1.1 Previous work 18

1.2 Motivation for Asymmetric Bleed Actuation 19

1.3 Objectives and Approach 20

2 Actuation Design and Testing 23

2.1 Requirements and constraints 23

2.1.1 Constraints 23

2.1.2 Requirements 24

2.1.3 Parameters available 25

2.2 Preliminary design 26

2.2.1 Simulations to determine downstream duct length 26

2.2.2 Second simulations and bandwidth requirement 30

2.3 Mechanical Design 34

2.4 Tests of the real valve 37

2.4.1 Bandwidth measurement 37

2.4.2 Rate limit 39

2.4.3 Mass Flow Capacity – Leakage – Calibration Curves 40

3 Experimental facility and procedure 47

3.1 History of the rig 47

3.2 The compression system 50

3.2.1 The compressor 50
3.2.2 The valves, actuation ring and downstream duct 50
3.2.3 The exhaust plenum and throttle 52
3.3 Instrumentation 54
3.3.1 Steady sensors 55
3.3.2 Unsteady sensors 56
3.4 Data acquisition and control 57
3.5 Calibration and Measurement Technique 59
3.5.1 Calibration Procedure 59
3.5.2 Stalling Mass Flow Measurement 61
3.5.3 Unsteady Mass Flow Measurement 62

4 Theoretical Model **63**
4.1 General 2D Bleed Model 63
4.1.1 Upstream Duct - Upstream Flow Field 64
4.1.2 Downstream Duct - Downstream Flow Field 65
4.1.3 Across the compressor 65
4.1.4 Bleed Valve relation 66
4.1.5 Plenum-throttle relations 67
4.1.6 Overall system of equations 68
4.1.7 Surge Dynamics Analysis 70
4.1.8 Rotating Stall Analysis 72
4.2 Transfer Functions Results - Sensor Locations 74
4.2.1 Surge Transfer Functions 74
4.2.2 Rotating Stall Transfer Functions 76

5 Experimental Results **81**
5.1 Open-loop behavior of the unactuated system 81
5.1.1 Steady Behavior – Speedlines 81
5.1.2 Unsteady Behavior – Transients Analysis 84
5.2 Forced Response of the actuated compression system 91

5.2.1 Identification Methodology 91

5.2.2 Zeroth mode – surge mode 92

5.2.3 First mode 94

5.3 Closed-loop behavior of the actuated compression system 96

6 Summary and Conclusions **101**

6.1 Future research 102

A Bleed Valves, Actuation Ring and Downstream Duct Drawings **105**

Bibliography **121**

LIST OF FIGURES

1-1 Illustration of rotating stall and surge 17

2-1 Experimental Compression System 24
2-2 Sketch of the compression System 26
2-3 Simulation of the surge for the system without actuation 29
2-4 Type of simulations 32
2-5 Inefficient and efficient actuation as seen on simulations 33
2-6 Bandwidth requirements 34
2-7 Valve and valve casing design 35
2-8 Transfer function for a system motor–$I = 2\ 10^{-5} kg.m^2$ 36
2-9 Transfer function for the system motor-valve and 4^{th} order model in dashed lines 37
2-10 Final valve design 38
2-11 High amplitude motor-valve response 39
2-12 Rate limit and step response 40
2-13 Calibration Test Bench 41
2-14 Calibration Test Results at p=.4psi 42
2-15 Calibration Test Results at p=.6psi 42
2-16 Calibration Test Results at p=.8psi 43
2-17 Calibration Test Results at p=1.psi 43
2-18 Calibration Test Results at p=1.25psi 44
2-19 Calibration Test Results at p=1.5psi 44
2-20 Calibration Test Results for the mass flow 45
2-21 Calibration Test Results for the discharge coefficient 45

3-1 View of the actuation ring 50
3-2 View of one actuator (system motor-valve) 51
3-3 View of the system 52
3-4 Sensor Locations 54
3-5 Data acquisition system 58
3-6 Throttle Calibration Curve 60

4-1 Sketch of the compression System 64
4-2 Bleed region 66
4-3 Pole-Zero Map: Surge dynamics 75
4-4 Pole-Zero Map Zoomed: Surge dynamics 75
4-5 Pole-Zero Map with throttle closing (Upstream sensing) 78
4-6 Pole-Zero Map with throttle closing (Downstream sensing) 79

5-1 Compressor speedline & Plenum pressure – Fully closed bleed valves . 82
5-2 Compressor speedline & Plenum pressure – Fully open bleed valves . 82
5-3 Comparison between experimental and model pressure rise across the fully open bleed valves 83
5-4 Open-loop system transients with time 84
5-5 Open-loop system transients in a $\Phi - \Psi$ plane 85
5-6 Hot-wire traces for open-loop compressor. 86
5-7 PSD of open-loop compressor prior to the stability limit. Solid and dashed lines represent forward and backward traveling waves respectively. 87
5-8 Surge mode PSD 88
5-9 First mode PSD 89
5-10 Second mode PSD 90
5-11 Opening of the valves (zeroth mode) 93
5-12 Surge mode forced response. Solid and dashed lines represent experimental and model transfer functions respectively. 93
5-13 Pole-Zero Map Comparison: Surge dynamics 94
5-14 Opening of the valves (first mode) 95

5-15 First mode forced response. Solid and dashed lines represent experimental and model responses (after parameters are tuned to values in Table 4.5 respectively. 96
5-16 PSD of closed-loop compressor prior to the open-loop stability limit. Solid and dashed lines represent forward and backward traveling waves respectively. 98
5-17 Speedlines and closed-loop stall points (*). 99
5-18 PSD of closed-loop compressor prior to the closed-loop stability limit. Solid and dashed lines represent forward and backward traveling waves respectively. 100

A-1 Assembly drawing 107
A-2 Valve 108
A-3 Valve casing – Part I 109
A-4 Valve casing – Part II 110
A-5 Valve casing – Part III 111
A-6 Actuation Ring – Overall View 112
A-7 Actuation Ring – Detail 1 113
A-8 Actuation Ring – Detail 2 114
A-9 Actuation Ring – Side View 115
A-10 Actuation Ring – Section G-G 116
A-11 Downstream Duct – Outer Duct 117
A-12 Downstream Duct – Outer Duct Detail 118
A-13 Downstream Duct – Inner Duct 119
A-14 Downstream Duct – Inner Duct Detail 120

LIST OF TABLES

3.1 GTL-LS3 design parameters 49

4.1 Separation of variables in the model 68

4.2 Surge linearization 72

4.3 Surge model parameters 74

4.4 Rotating stall notation 77

4.5 Higher mode analysis parameters 77

CHAPTER 1

INTRODUCTION

Over the last few decades, gas turbines have evolved and their performance has increased greatly. However, their performance is still strongly limited by the existence of inherent fluid dynamic instabilities in the compressor. These instabilities, *rotating stall* and *surge* (Figure 1-1) happen when axial compressors are driven to higher pressure ratios and lower mass flow. A comprehensive review of the flow instabilities present in compression systems is given by Greitzer [10].

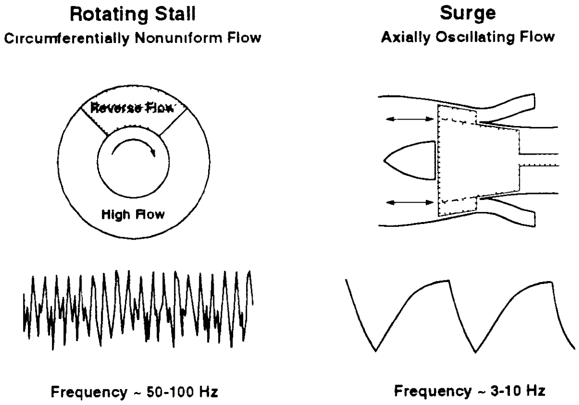
Rotating Stall
Circumferentially Nonuniform Flow
Surge
Axially Oscillating Flow
Reverse Flow
High Flow
Frequency ~ 50-100 Hz
Frequency ~ 3-10 Hz

Figure 1-1: Illustration of rotating stall and surge (from [10]). A sketch of the transient signatures that would be given by high response pressure probes in the compressor (for rotating stall) or in the combustor, or other volume downstream of the compressor (for surge).

Surge is a large amplitude, circumferentially uniform pulsation of the mass flow through the overall pumping system. Surge is usually very violent and can lead to severe damage to the compressor structures. In a jet engine, surge may also cause the combustor flame to blow out. One can usually recover from surge by simply unloading the compressor; but, by the time such recovery has been effected, severe engine damage may have occurred.

Rotating stall refers to a dynamic instability that occurs when a non-axisymmetric flow pattern develops in the blade passages of a compressor stage and travels around the annulus at a fraction of the rotor speed. Rotating stall leads to a dramatic drop in pressure rise and efficiency and may cause the burner of a jet engine to overheat. Unlike surge, rotating stall may be unrecoverable in an engine. Indeed, there is a significant mass flow hysteresis associated with rotating stall. If the compressor is trapped in rotating stall, it may have to be unloaded to the point that the turbine must be shutdown. Such cases require a full engine shutdown and restart.

As gas turbine engines have become better understood and better designed, increasing performance has begun to press the limits of what can be achieved without some type of control. The desire for still higher performance and greater efficiency, as well as the emergence of improved sensing, actuation, and computation, have driven research into active control techniques.

1.1 Previous work

Surge and Stall were first studied theoretically by Greitzer in [9] where a 1D model was analytically developed and experimentally tested. Moore developed a 2D model of rotating stall in [20] using actuator disk theory. Moore and Greitzer combined their efforts in [21] to develop the well-known Moore-Greitzer model of rotating stall and surge. Many contributions were then added, by different authors, to the initial Moore-Greitzer model; these are surveyed by Longley in reference [18].

After this successful understanding and modeling of the so-called surge and rotating stall instabilities, a new era was open: the one of active control. In [4], Epstein et al. suggested that active control could be used to improve the stall margin and increase the stable operating range of compression systems. The door was then open for researchers to study experimentally active control schemes.

Pinsley [24] and Simon [29] successfully implemented linear surge control on centrifugal pumps. Paduano [22] demonstrated control of rotating stall, for the first time, in a single stage low-speed axial compressor. Haynes extended this work and successfully implemented active control of rotating stall on a three-stage axial compressor.

Other theoretical and experimental studies, for instance with distortion at the compressor inlet, were done by Van Schalkwyk [27] and Setiawan [28] and non linear control was also investigated, for instance by Mansoux [19], Liaw & Abed [17] and Protz [26].

On the actuation side, Pinsley successfully implemented linear surge control using a 1D bleed valve on a centrifugal compressor. Liaw and Abed proposed a nonlinear control law that used plenum bleed to eliminate stall hysteresis [17]. Eveker et al. extended the Liaw-Abed control law to avoid surge and implemented the control law experimentally [5]. 1D Bleed valve control of rotating stall with continuous air injection in an axial compressor is presently being studied experimentally by Yeung and Murray [32].

1.2 Motivation for Asymmetric Bleed Actuation

As seen in the previous section, there has been much work on improving compression system operability using active control concepts. However, a lot of these previous research projects addressed rotating stall or surge independently; either controlling rotating stall in an axial flow machine in operating regimes incapable of surge, or controlling surge in centrifugal compression systems for which rotating stall were inconsequential. These efforts have been successful in enhancing the stability of such compression systems in laboratory environments. However, there has been little work in the area of addressing compression systems which demonstrate strong interaction between rotating stall and surge. This type of coupling is very common in modern aeroengines.

Furthermore, all the strategies studied so far have to be implemented in some way on a real aeroengine. So far, all the attempts to stabilize rotating stall were done with an array of actuators (IGV's (12 vanes) or Injectors (24 injection ports) to cite them). Therefore, more industrially applicable (i.e. lower complexity) ways to control the instabilities seem to be the next step.

Single-dimensional bleed valves were previously successfully implemented in preventing surge in centrifugal compressors and circumferentially distributed actuation using IGV's or injectors was also successfully implemented. This research looks for synergies between 1D,2D, linear and nonlinear control.

A circumferentially distributed array of bleed valves (asymmetric bleed actuation) is used for control in this research. But this number is kept low to assess its industrial applicability. The fact that bleed valve actuation needs no recirculation (cf. injection) makes it a very simple type of actuation which is also very interesting for industrial purposes. This thesis presents the first attempt to use 2D bleed valve actuation for control since, so far, only 1D control using bleed valves has been investigated.

1.3 Objectives and Approach

The objective of the research presented here is to experimentally evaluate the use of a moderate number of compressor exit bleed valves (CEBV) for the purpose of controlling a compression system in which rotating stall and surge are highly coupled.

The process chosen is the following:

1. Design the actuation.
2. Build, test and implement the actuation on the existing three-stage compressor rig.

3. Develop 1D and 2D models of the compression system with actuation.
4. Use the model to find the best sensor location strategy.
5. Identify the 1D system experimental dynamics and use these to validate the 1D model.
6. Identify the 2D system experimental dynamics and use these to validate the 2D model.
7. Evaluate the 2D stabilizing effect of the actuation scheme.
8. Propose new ideas and remarks for continuing research.

The thesis is organized as follows. Chapter 2 describes the design and testing of the valve and actuation system, and provides insights on the factors which limit the performance of the actuators. Chapter 3 details the experimental facility and test procedures. Chapter 4 then gives a description of the theoretical model of the compression system with 2D bleed actuation. Experiment results, namely system identification, model validation and active control results, as well as a the evaluation of the 2D stabilizing effect of the bleed actuation scheme, are presented in Chapter 5. Finally, a summary, conclusions and suggestions for future research are given in Chapter 6. The Appendix gives the design details (complete drawings) of the rig modifications.

CHAPTER 2

ACTUATION DESIGN AND TESTING

The first important step preliminary to a successful design is the determination of the important requirements and constraints. After that, it is necessary to determine the parameters available to achieve the requirements while taking into account the different constraints. Finally, the use of the theory is the last step in the iterative design process to get to a good and practical design. Here, one must keep in mind that stating the right assumptions to simplify the calculation is crucial. For this Chapter, the design process described above is detailed for the bleed valve actuation system. Following this are the results of the valve and actuation system testing with a description of the limiting factors of such an actuator.

2.1 Requirements and constraints

2.1.1 Constraints

The MIT three-stage compression system was chosen for this research project. The initial compression system to take into account is depicted in Figure 2-1.

This system was modified by J.M. Protz in order to present surge and rotating stall instabilities coupled together. The geometric constraints that this setup imposes are the following:

- Since the exhaust plenum could not be moved, any "downstream duct" (see Section 2.2.1) must be placed *inside* the plenum, but not too close to the end wall of the box, to be sure that the air will flow in the plenum in a free manner.

- The actuation had to be simple enough and easily interfaced with the existing compression system.

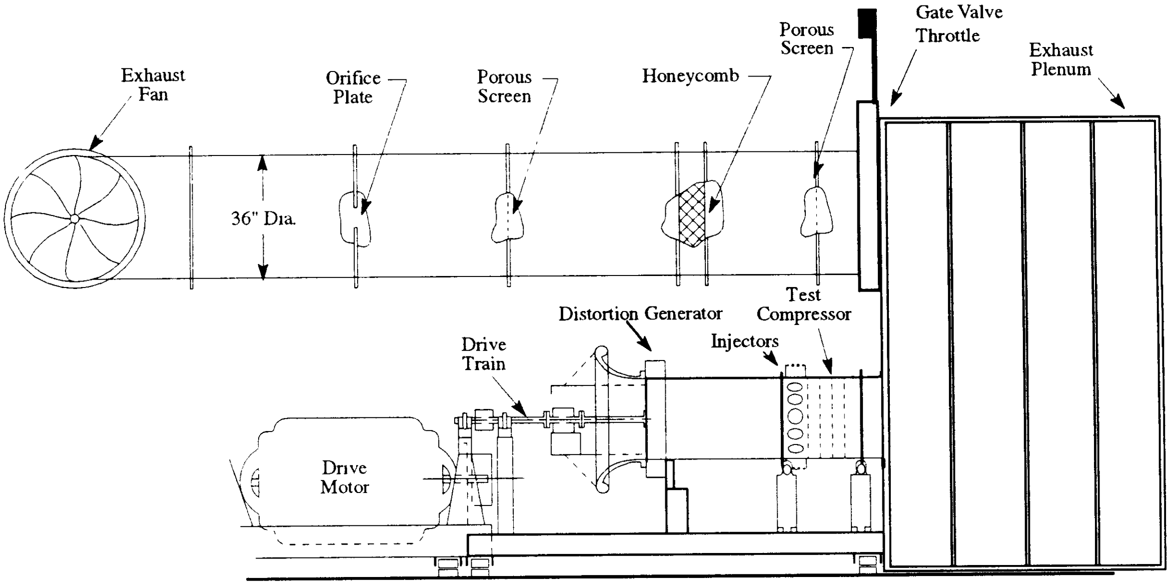

Exhaust Fan
Orifice Plate
Porous Screen
Honeycomb
Porous Screen
Gate Valve Throttle
Exhaust Plenum
36" Dia.
Test Compressor
Distortion Generator
Injectors
Drive Train
Drive Motor

Figure 2-1: Experimental Compression System

2.1.2 Requirements

Efficient Actuation

The obvious first requirement is to have efficient actuation. Bleed valve actuation is the chosen scheme for this research project. To be an efficient actuator, a bleed valve must have a high mass flow capacity and be fast. In order to increase the bleed capacity, a downstream duct was added to the actual system. This duct was there indeed to act like an impedance (resistance) to the flow downstream of the valves such that more air could be bled through the valves. Notice that other possibilities such as the addition of a screen downstream of the bleed valves could be used to even more increase the bleed capacity of the valves.

Ability to surge

An efficient actuation is indeed needed but surging the compressor when the actuation is not used was also a requirement. Indeed, as stressed in the introductory Chapter, strong coupling between rotating stall and surge, typical of modern aeroengines, is desired in the experimental setup. The work done by J. M. Protz [26] led to design a plenum to have a "surgeable" system. Since adding a long downstream duct leads to a higher inertia for the system and therefore a weaker trend to surge, it was important to know quantitatively the trade-off between efficient actuation and surge behavior.

Simplicity

Simple actuator design and simple implementation are crucial. This requirement seems obvious to anybody doing experimental work, but the ability to make easy minor changes to the system was not the only thing sought by this simplicity requirement. It was also strongly believed that the use of a moderate number of easily implemented actuators is very important for a practical solution and implementation for industrial purposes.

2.1.3 Parameters available

The main design parameters available to reach the requirements under the constraints stated above were the downstream duct length, the number, area and inertia of the valves.

2.2 Preliminary design

All the constraints, requirements and design parameters taken into account, a classic model of the system considering the upstream distortion screen (0-1 in Figure 2-2), the upstream duct (1-2), the compressor (2-3) , the bleed valves (3), the downstream duct (3-4), the plenum (4) and the downstream throttle (4-atmosphere) was considered. This system model could be sketched as it is in the Figure 2-2 and is the model that will be used in all the modeling parts of this project, during the design phase of the project as well as the control phase.

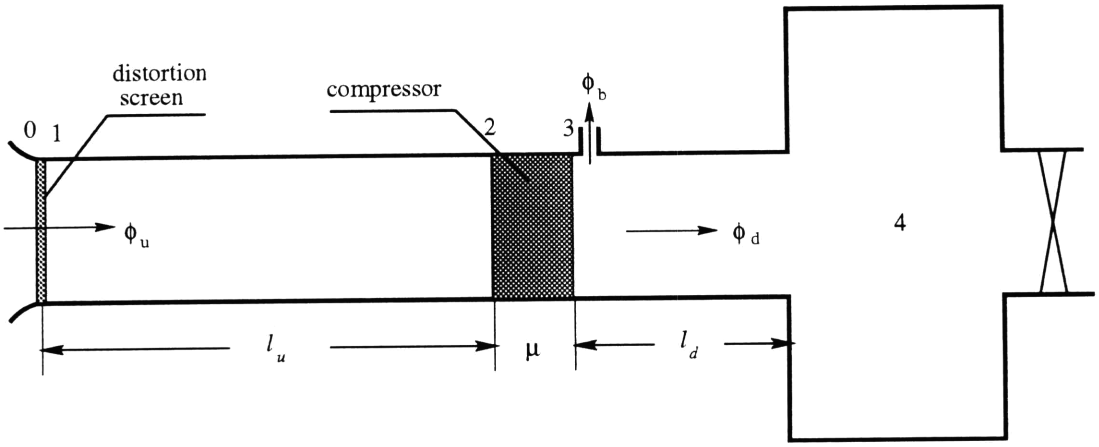

Figure 2-2: Sketch of the compression System

2.2.1 Simulations to determine downstream duct length

The purpose of these first non linear single-dimensional simulations was to find the maximum total length $L_{tot} = l_u + \mu + l_d$ (see Fig. 2-2) of the system, still allowing it to exhibit surge behavior without actuation[1]. Based on model analyses (see Chapter 4), 1D simulation is valid for this purpose since the downstream duct length has no 2D effect on the system. The model used was the one explained in detail by Greitzer in [9]. 1D distortion was added to the model (considering it equally circumferentially distributed) to represent the pressure loss effect of distortion. The simulation was based on the non-dimensionalized equations, written below.

---

[1] all the bleed valves kept closed

The following variables are used for nondimensionalization:

-R = mean rotor radius, nondimensionalizes lengths

-A_c = compressor annulus area

-U = rotor wheel speed, nondimensionalizes speeds

-ρU^2 = rotor referenced dynamic head, nondimensionalizes pressures

-$\rho U A_c$ = rotor referenced mass flow, nondimensionalizes mass flows

The following parameters (see also Figure 2-2) are used in the derivation:

-$l_u = L_u$/R = nondimensional upstream duct length

-$l_d = L_d$/R = nondimensional downstream duct length

-μ = nondimensional cumulative blade-row length (see Ref. [21])

-$l_c = (l_u + l_d + \mu)$ = nondimensional total compression system length

-a = dimensional speed of sound

-V_p = dimensional plenum volume

-B = Greitzer B parameter (see below)

-$\omega_h = \frac{U}{R}$ = pulsation nondimensionalizes time $(t_{nondim} = \omega_h t)$[2]

-$\tilde{\tau} = \omega_h \tau$ = compressor flow-field time constant (see Ref. [9]), with $\tau = \frac{N 2\pi R}{U}$ and N = 2.5 for this compressor (N = number of rotor revolutions needed for the development of a stall cell)

The following nondimensional flow variables are defined for the derivation:

-$\phi_u = C_x$/U, the nondimensional upstream mass flow (in this case, it is equal to the downstream mass flow)

---

[2] from now on, t_{nondim} is simply written t

-ψ = the nondimensional plenum pressure

-$\psi_{c_{ss}}$ = steady state total-to-static compressor pressure rise

-ψ_c = actual compressor pressure rise

-ϕ_t = the nondimensional throttle mass flow

-ψ_{dist} = the nondimensional 1D distortion pressure drop (negative value)

The assumption of no dynamics in the throttle duct downstream of the plenum was made. Then, the system of equations to solve takes the following form (see Ref. [9]).

$$\left\{\begin{aligned} \frac{d\phi_u}{dt} &= \frac{1}{l_c}(\psi_c + \psi_{dist} - \psi) \\ \frac{d\psi}{dt} &= \frac{1}{4l_c B^2}(\phi_u - \phi_t) \\ \frac{d\psi_c}{dt} &= \tilde{\tau}(\psi_{c_{ss}}(\phi_u) - \psi_c) \end{aligned}\right. \tag{2.1}$$

with the "steady" relation between the throttle mass flow and plenum pressure,

$$\psi = \frac{K_t {\phi_t}^2}{2} \tag{2.2}$$

In equations 2.1, downstream duct length enters both as $1/l_c$ and as a factor effecting the Greitzer B parameter:

$$B = \frac{U}{2a}\sqrt{\frac{V_p}{A_c L_c}} \tag{2.3}$$

Since l_c is the only parameter we will vary in this study, and since B and l_c are directly related, design studies were done by vary B and substituting $l_c = f(B)$ wherever l_c appears above.

The initial condition for all the simulations was taken at the peak of the compressor curve and time evolution of the mass flow and plenum pressure was resolved. The numerical method used to solve this system was a 4^{th} order Runge-Kutta method.

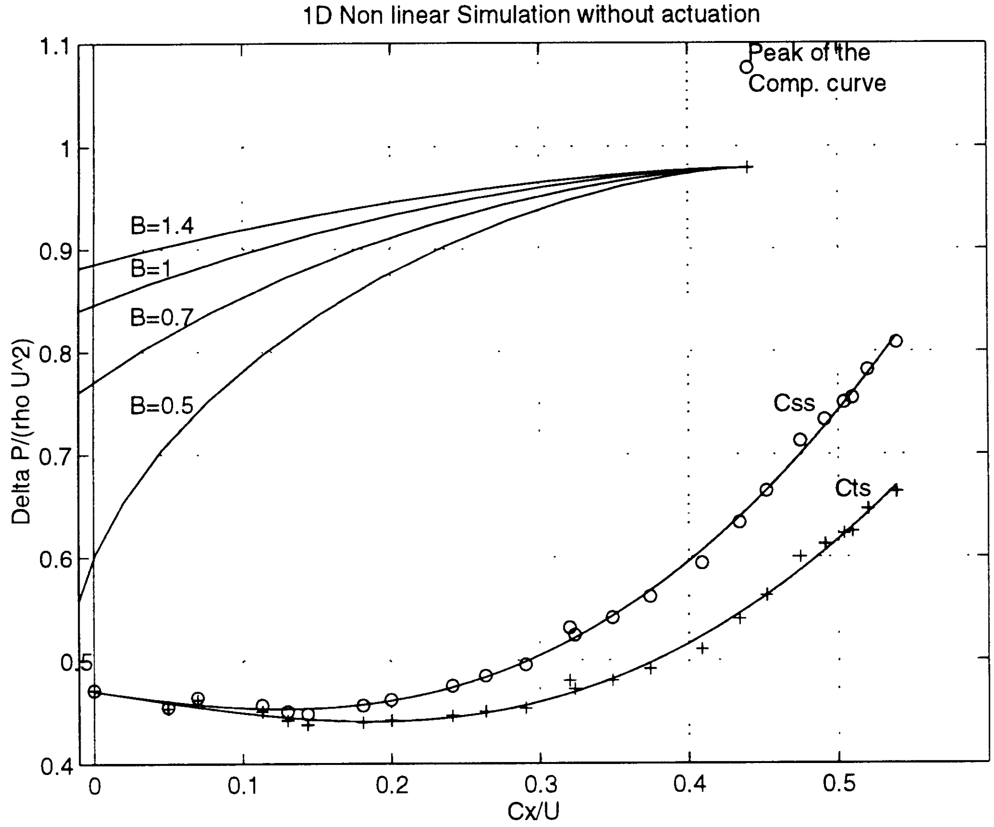

Figure 2-3: Simulation of the surge for the system without actuation

The results can be shown in a (ψ, ϕ) graph (Figure 2-3) where one can see the evolution of the plenum pressure with an initial condition at the peak of the compressor map and a one-dimensional distortion of one rotor dynamic head (1 D.H.= $\rho U^2/2$). The curves C_{ss} and C_{ts} represent curve fits to the measured (see Ref. [16]) static-to-static and total-to-static compressor pressure rise while in stall condition and were the values used in the simulations. The criterion to determine the maximum acceptable duct length is that the system must demonstrate deep surge; that is, backward flow behavior must be seen. From the Figure 2-3, a reasonable value B of 0.7 was chosen as a value which exhibited both reverse flow and a mass flow drop characteristic of deep surge. Based on this value of B, the maximum allowable downstream duct length, l_d, was found to be 1.9 m.

2.2.2 Second simulations and bandwidth requirement

The goal of these simulations is to determine the bandwidth requirement for the valves in order to assure that the system surge mode can be stabilized. The approach here uses the same single-dimensional Greitzer's surge model as in the previous section with the additional effect of actuation. The assumption of no dynamics in the throttle duct downstream of the plenum (see Figure 2-2) remains. The new set of equations were then integrated in time using the same Runge-Kutta algorithm as used in Section 2.2.1.

$$\left\{\begin{array}{rcl} \dfrac{d\phi_u}{dt} & = & \dfrac{1}{l_c}(\psi_c + \psi_{dist} - \psi + l_d\dot{\phi}_b) \\ \dfrac{d\psi}{dt} & = & \dfrac{1}{4l_cB^2}(\phi_u - \phi_b - \phi_t) \\ \dfrac{d\psi_c}{dt} & = & \tilde{\tau}(\psi_{c_{ss}}(\phi_u) - \psi_c) \end{array}\right. \tag{2.4}$$

with the "steady" relation between the throttle mass flow and plenum pressure,

$$\psi = \frac{K_t{\phi_t}^2}{2}$$

In this case, there is one more variable (ϕ_b) to take into account and in order to simulate it, an additional equation for the actuation dynamics must be added to the present model. A second-order system was chosen to model the bleed flow which added two more states to the previous model. The equation for ϕ_b can be written:

$$\ddot{\phi}_b + 2\xi\overline{\omega}_n\dot{\phi}_b + \overline{\omega}_n{}^2\phi_b = U \tag{2.5}$$

with U being the command of the second-order system.

The simulation was done using the peak of the compressor curve as the initial condition with a 1D distortion of one dynamic head (1D.H.). The criterion for the effectiveness of the bleed valves as actuation is that it had to prevent the system from surging. In the simulation itself, a command of fully open valve (maximum mass flow through the valves) was applied. That means that the valves try to be open completely as commanded at the initial conditions.
The command was calculated by assuming that the valves would have a maximum mass flow (when fully open) of about 20% of the compressor mass flow at the peak of the compressor curve. This value was taken from the literature (see Ref. [32]) as the maximum bleed level one is likely to implement in a real system.

The second-order equation 2.5 can then be split into two first-order equations after a change in variables:

$$\left\{\begin{array}{lcl} x_4 & = & \phi_b \\ x_5 & = & \dot{\phi}_b\ , \end{array}\right. \tag{2.6}$$

and equation 2.5 becomes:

$$\left\{\begin{array}{lcl} \dot{x_4} & = & x_5 \\ \dot{x_5} & = & -2\xi\overline{\omega}_n x_5 - \overline{\omega}_n{}^2 x_4 + U \end{array}\right. \tag{2.7}$$

Equations 2.7 can now be added to the system of equations 2.4 and solved using the 4^{th} order Runge-Kutta method. The parameters varied in the simulations were $\overline{\omega}_n$ and B. Many simulations were then run for different values of ($\overline{\omega}_n$,B). For each value of B, the valve bandwidth necessary to control the surge was found. Two types of simulations were done:

1. with distortion added at t=0 (initial condition at the peak of the compressor curve) – see Figure 2-4 (b),
2. with distortion already present before the inception point (already there as before t=0) – see Figure 2-4 (a)

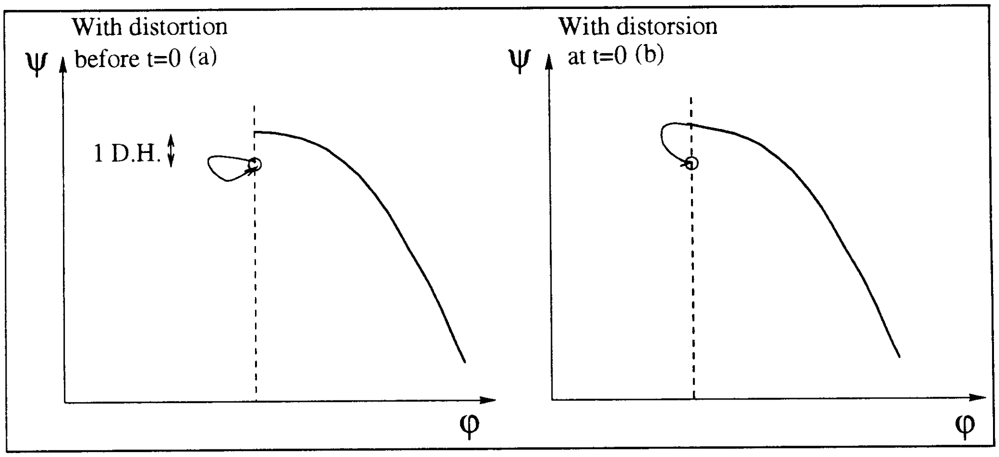

Figure 2-4: Type of simulations

For each type of simulation and for each value for B, the simulation showed either stabilizing actuation (see Figure 2-5 (b)) or inefficient actuation (see Figure 2-5 (a)) depending on the value of the valve-motor system bandwidth.

With this criterion, it was possible to find the bandwidth requirement for each value of B and relate the value of B to the corresponding total length of the compression system. Since the upstream duct length is constant, the value of ω_n required to control the compression system for each value of the downstream duct length was found from these simulations. Figure 2-6 show the results for the case without distortion before t=0 and with distortion before t=0 respectively. It is the case without distortion before t=0 that is the one to take into account for design. Indeed, it provides the conservative case since it gives the largest initial perturbation to the system.

The curve in these two plots gives the relation between B and l_d. From these plots,

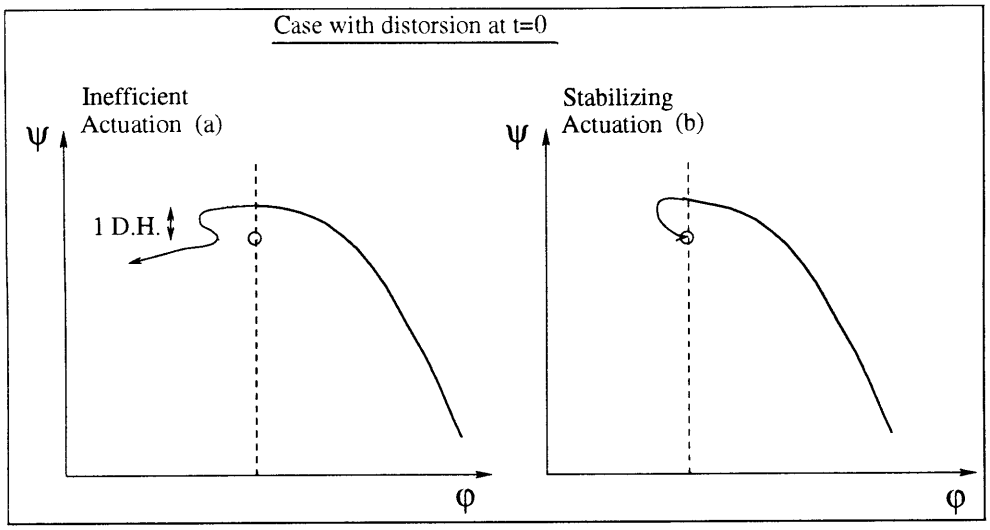
Case with distorsion at t=0
Inefficient Actuation (a)
Stabilizing Actuation (b)
ψ
ψ
1 D.H.
φ
φ

Figure 2-5: Inefficient and efficient actuation as seen on simulations

we see that for each bandwidth of the valve, the domain where the actuation is efficient is under the horizontal line giving the maximum B reachable by the "controlled" compression system. The intersection of this line with the curve $B = f(l_d)$ gives the necessary downstream duct length to achieve a stabilizing effect of the actuation. For instance, the right (conservative) plot in Figure 2-6 shows that with a valve-motor system having a natural frequency ($f_n = \omega_n/2\pi$) of 100Hz, a downstream duct of at least 0.41m should be added to the compression system in order to get enough actuation power to control the system.

For the design, a downstream duct of $0.9m$ (which satisfies the constraint of $l_d < 1.9m$; cf section 2.2.1) was chosen such that a reasonable goal for the valve-motor bandwidth was assessed. Figure 2-6 gives the bandwidth requirement to take into account for the design of the valve: the natural frequency must be higher than 50 Hz.

After these simulations and with a first "guess" of the total bled mass flow of 20% of the compressor mass flow at the peak of the compressor curve and of the limited number of valves (3 or 4), a first design of the valve was done which gave its design area and inertia.

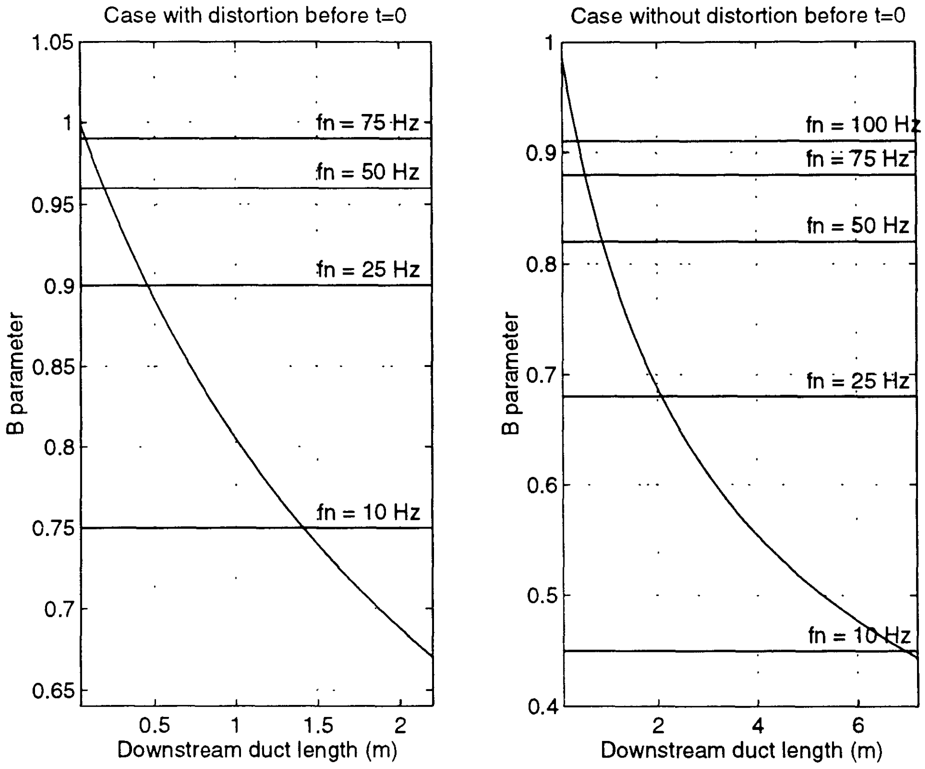

Figure 2-6: Bandwidth requirements for different values of B to control

2.3 Mechanical Design

The problem now is to physically design the valves, the actuation ring and the downstream duct in an easy, implementable and cost effective way.

The valves need to be designed such that the mass flow required can be achieved when all the valves are fully open.
The leakage of the same valves, that is, when the valves are fully closed, must be minimized.
The valves must work properly, that is, the problems of rubbing that was previously experienced with other types of valves must be avoided.
Use of existing servo-motors as the valve actuator of a custom made valve was chosen as a cost effective solution.
Figure 2-7 shows the chosen design for the valve. The area of the valves was calculated

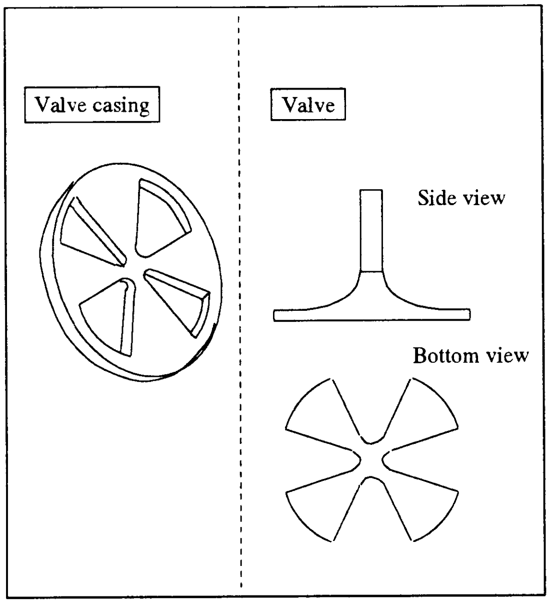

Figure 2-7: Valve and valve casing design

with the choice of three valves for the required "20% mass flow", using the relation:

$$\dot{m} = \sqrt{\rho} A_b C_d \sqrt{2 \Delta p} \tag{2.8}$$

and with the discharge coefficient $C_d = 0.63$ found from Reference [14]. The clearance between the valve and the valve casing (see Figure 2-7) acceptable for this choice of valve, was also determined with the tables of C_d in Ref. [14]. This clearance was also a major concern since it is a trade-off between machining precision (flatness, perpendicularity and parallelism), desire for low leakage and the importance of no rubbing.

The valve needs to be strong enough to support high amplitude and frequency opening commands. There is a trade-off between this last constraint and a low inertia feature for a good bandwidth of the system motor-valve, which is critical. To determine the inertia the system could afford in order to reach the "very critical" bandwidth requirement (see Section 2.2.2), a bandwidth test of the system equivalent[3] to the system valve-motor was done. The inertia tested was I=2 $10^{-5} kg.m^2$.

---

[3] in terms of inertia

The dynamic behavior of the actuator was measured by inputing frequency sweeps from 0 to 200 Hz with an amplitude giving a $\Delta\theta$ of +/- 4^o as motor command and measuring the encoder position. The resulting computed transfer function is plotted in Figure 2-8 and shows a resonant frequency of 55 Hz, which was a good first result, considering that the PID motor controller parameters (gain, zero location, etc.) were not very well optimized.

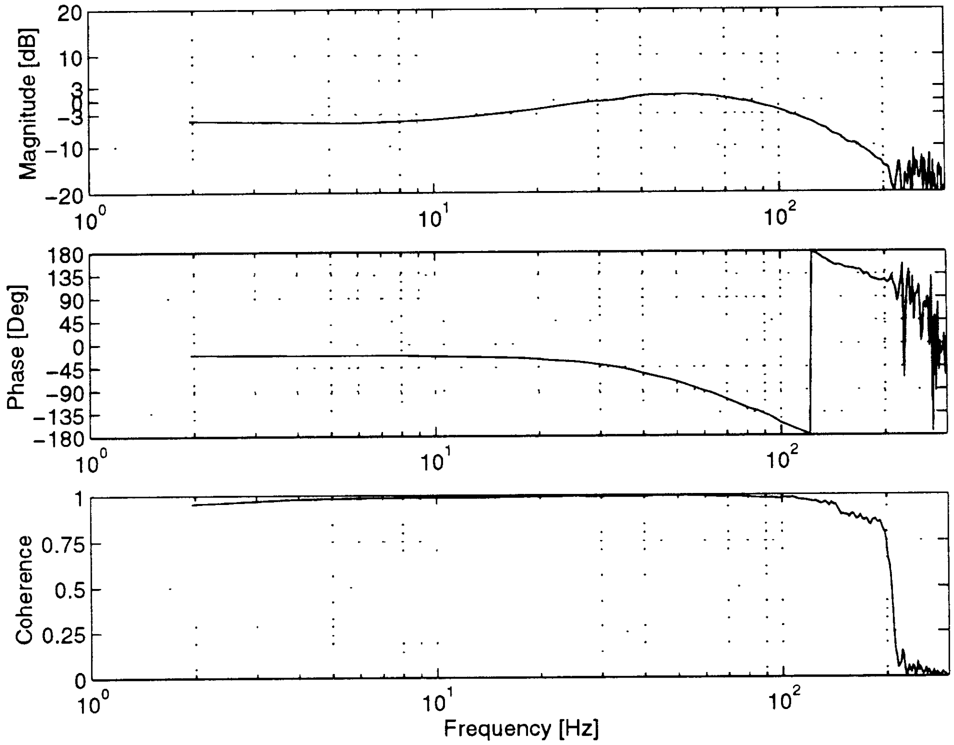

Figure 2-8: Transfer function for a system motor-$I = 2\ 10^{-5} kg.m^2$

One can also see that there is a dc offset which is due to the bad optimization done by the automatic tuning tool of the PID controller code. In Section 2.4 we will see that a better dynamic behavior of the system valve-motor can be achieved with a "by hand" tuning. A more detailed description of the transfer function measurement procedure can be found in Refs. [31] & [2].

2.4 Tests of the real valve

After the machining of one valve, different tests needed to be done on this valve.

2.4.1 Bandwidth measurement

The first test was the dynamic response test of the system valve-motor. Tuning the PID controller by hand gave a much better response. The parameters of the PID controller were the following:

$$GN = 17\ ;\ Zr = 239\ ;\ PL = 0\ ;\ KI = 0$$

The input consisted of sweeps from 0 to 200 Hz at an amplitude of $\Delta\theta$ of +/- 4^o.

The measured transfer function between the angle command and shaft angle is plotted in Figure 2-9.

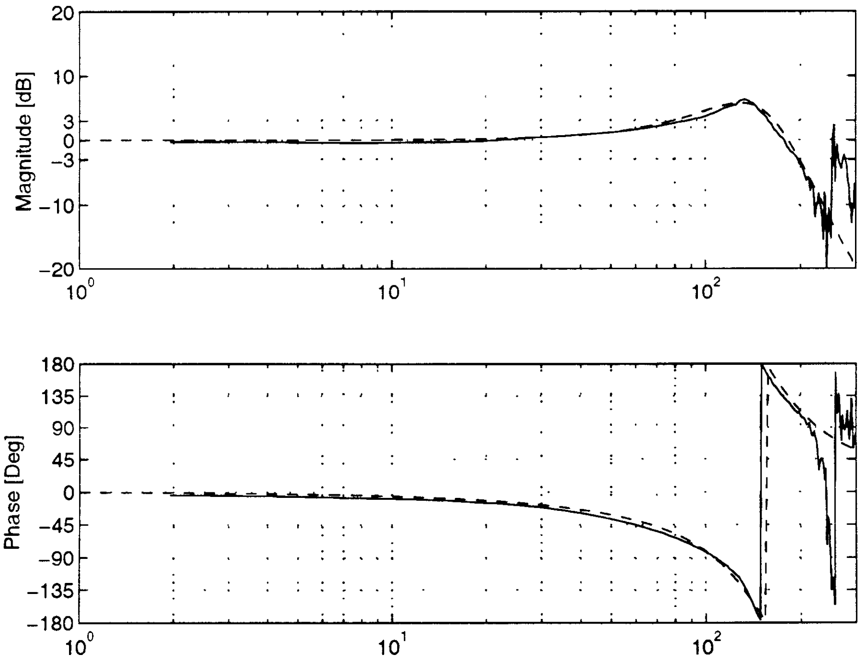

Figure 2-9: Transfer function for the system motor-valve and 4^{th} order model in dashed lines

These results show that, compared to the last result (see Figure 2-8), the response can be improved. However, this was done for a low amplitude angle position input which means that another frequency response was to be taken at a higher amplitude.. A fourth order system was fitted to the previous measured transfer function:

$$F(s) = \left[\frac{{\omega_n}^2}{s^2 + 2\xi\omega_n s + {\omega_n}^2}\right]^2 \qquad (2.9)$$

Since the whole valve was made in aluminum and since the shaft was very thin, fatigue problems were expected to arise which was actually experienced after some cycles of bandwidth testing.

To avoid that problem in the future, a steel shaft, which added an insignificant contribution to the inertia, was added to the previous design, such that the final valve layout is depicted in Figure 2-10.

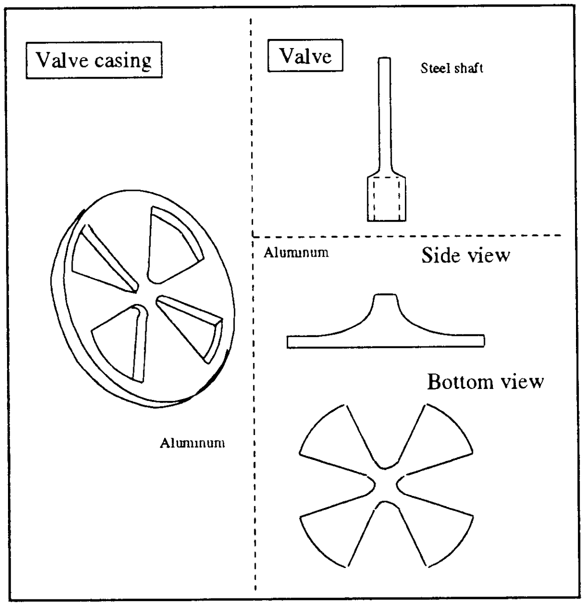

Figure 2-10: Final valve design

With this robust valve, actual high amplitude response was done and the gain and zero of the motor-valve PID controller was re-optimized. Problems of motor-valve-controller system limit cycling were experienced for an amplitude of $\Delta\theta$ of $+/-$ 22°

such that the amplitude had to be limited to $\Delta\theta$ of +/- 14°. The PID controller parameters were then fixed at the following values for the remainder of the thesis:

$$GN = 6 \; ; \; Zr = 250 \; ; \; PL = 0 \; ; \; KI = 0$$

The corresponding motor-valve response is depicted in Figure 2-11.

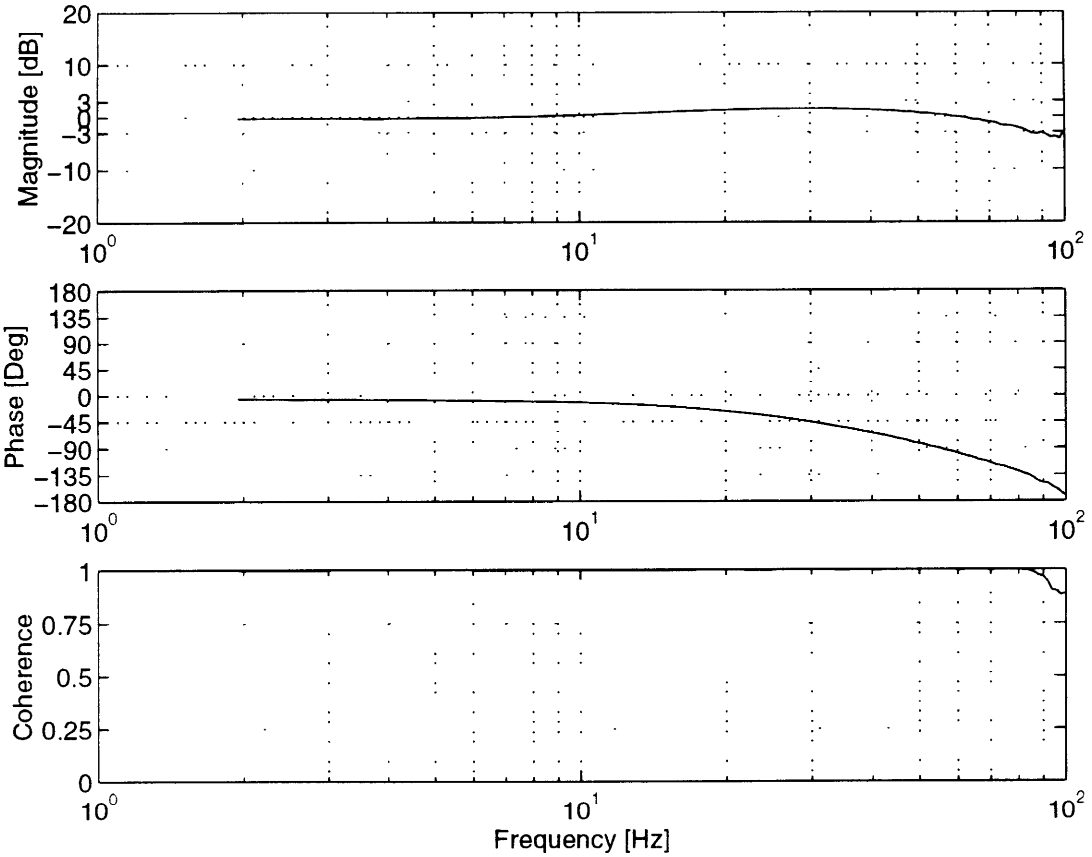

Figure 2-11: High amplitude motor-valve response

2.4.2 Rate limit

The bandwidth is not the only requirement for an efficient actuation. According to Yeung & Murray [32], the rate limit is also a serious limiting factor for an efficient bleed actuation.

It is defined as the maximum slope in terms of degrees/seconds that the servomotor can achieve and this limit can easily be found by inputing a step to the servodynamics and measuring its step response (see Figure 2-12).

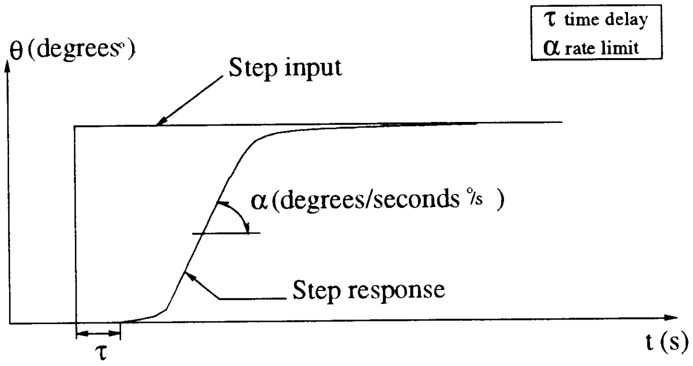

Figure 2-12: Rate limit and step response

The measurement gives a rate limit of $450^o/s$.

2.4.3 Mass Flow Capacity – Leakage – Calibration Curves

The system valve-casing was then tested in terms of mass flow capacity (fully open valve) and leakage (fully closed valve). Calibration curves were also measured for the same system.

The test bench built and used for all the mass flow measurements for different angle positions of the valve and different supply pressures is depicted in the following Figure 2-13.

Closing angles between 0 to 45 degrees were tested and with a tank pressurized at 0.4; 0.6; 0.8; 1; 1.25 and 1.5 psig. 0^o corresponds to a fully open valve and 45^o to a fully closed valve. The mass flow is measured by the rotometer with the relation:

$$\dot{m}_{fullscale} = \rho_{stp}.(SCFM)_{fullscale}$$

$$\dot{m} = (R).\dot{m}_{fullscale}.\sqrt{\frac{\rho_{rot}T_{stp}}{\rho_{stp}T_{rot}}}, \tag{2.10}$$

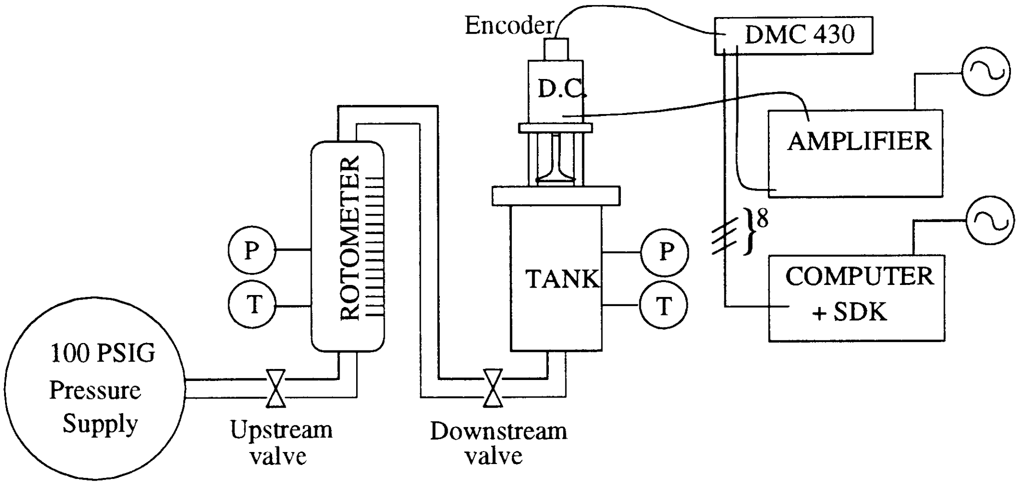
Encoder
DMC 430
D.C
AMPLIFIER
8
COMPUTER
+ SDK
ROTOMETER
P
T
TANK
P
T
100 PSIG
Pressure
Supply
Upstream
valve
Downstream
valve

Figure 2-13: Calibration Test Bench

where ρ_{stp}, T_{stp} are the standard density and temperature conditions at which the rotometer was calibrated; $SCFM$ is the full scale standard cubic feet per minute passed by the rotometer; R is the fraction of full scale (0 to 1) reading on the rotometer; ρ_{rot} and T_{rot} are the measured rotometer conditions at the time of the reading R.

The discharge coefficient is deduced from the mass flow charts 2-14 to 2-19 and the relation 2.8.

All these plots can be viewed in a complete 3D plot for the mass flow and the discharge coefficient.

From Figures 2-14 to 2-19, one can see that leakage ($\dot{m}$ at 45^o) was measured to a value less than 1% of the total mass flow capacity of the valve.

From Figures 2-20 and 2-21, one can see that mass flow through the valve is quite linear with the opening angle, the pressure supply being constant. It can also be seen that the discharge coefficient stays constant for a wide range of angles (approximately 78% of the 45^o angle range).

The value of C_d at $1psi$ and for an angle opening of $12deg$ will be used in the model (see Chapter 4).

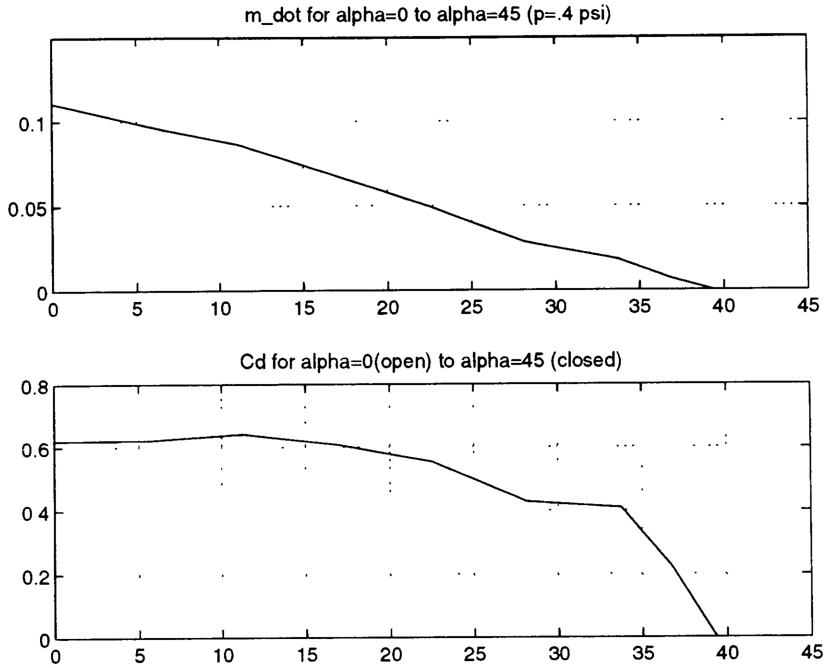

Figure 2-14: Calibration Test Results at p=.4psi

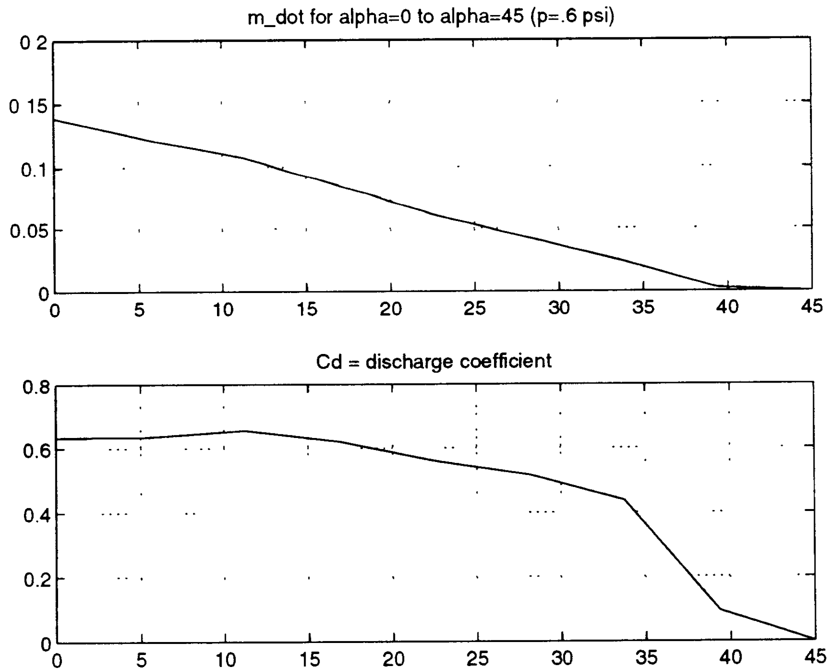

Figure 2-15: Calibration Test Results at p=.6psi

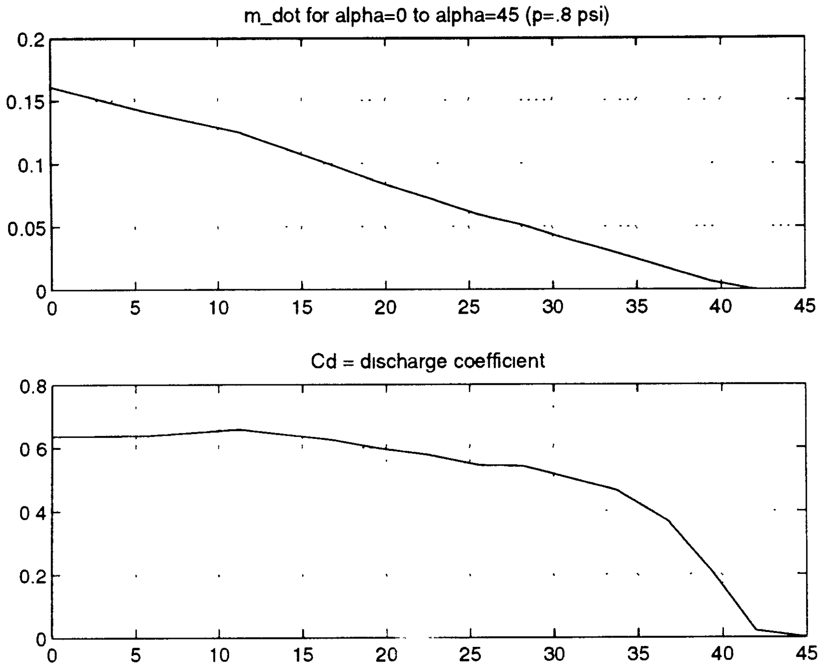

Figure 2-16: Calibration Test Results at p=.8psi

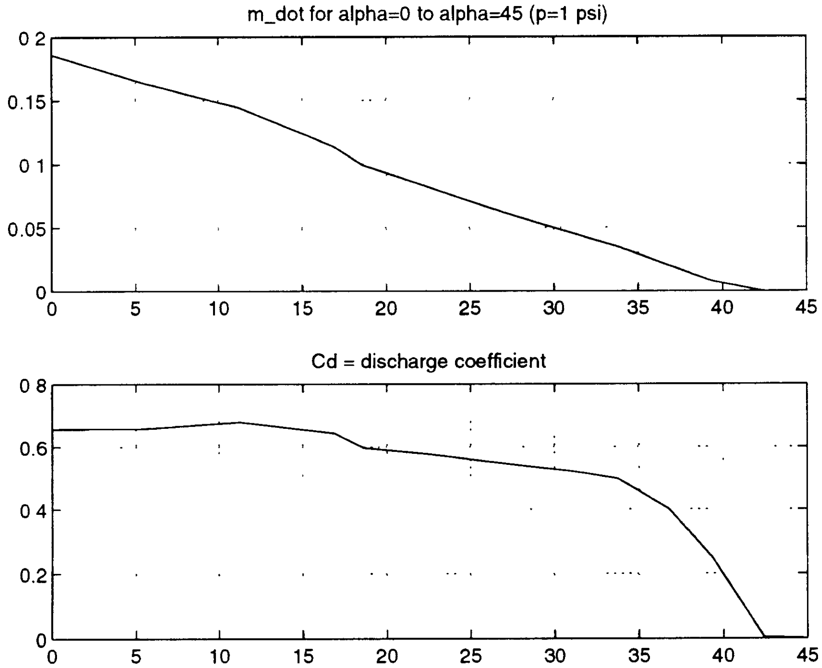

Figure 2-17: Calibration Test Results at p=1.psi

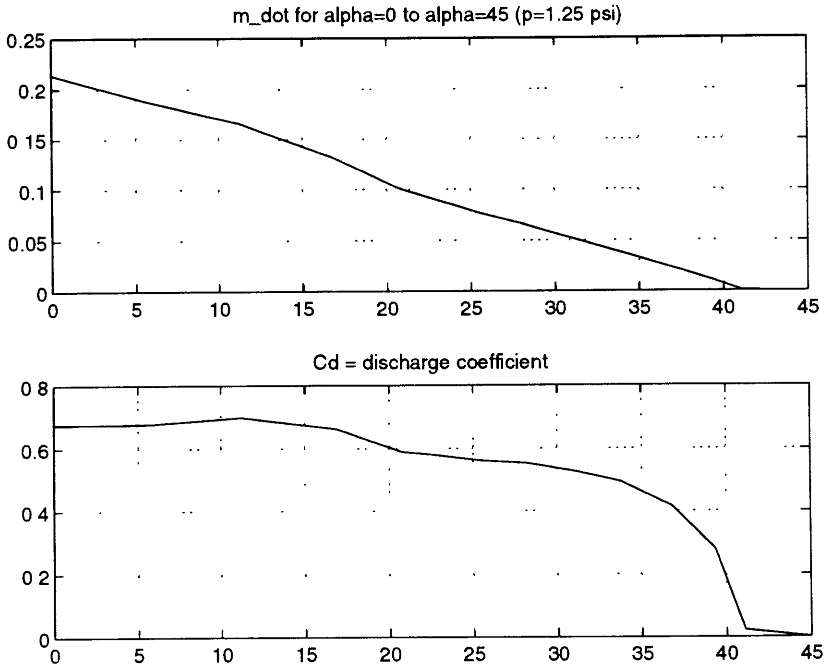
m_dot for alpha=0 to alpha=45 (p=1.25 psi)

Cd = discharge coefficient

Figure 2-18: Calibration Test Results at p=1.25psi

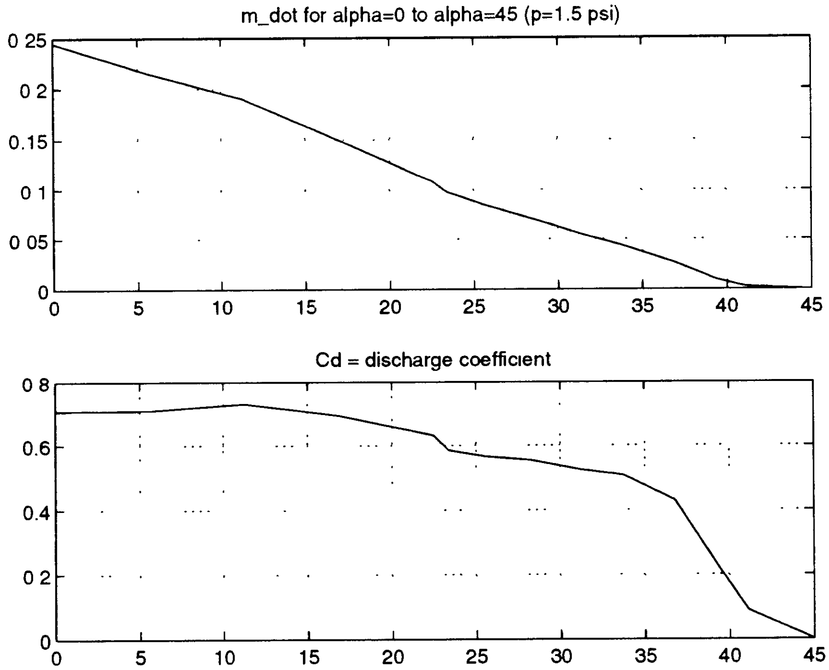
m_dot for alpha=0 to alpha=45 (p=1.5 psi)

Cd = discharge coefficient

Figure 2-19: Calibration Test Results at p=1.5psi

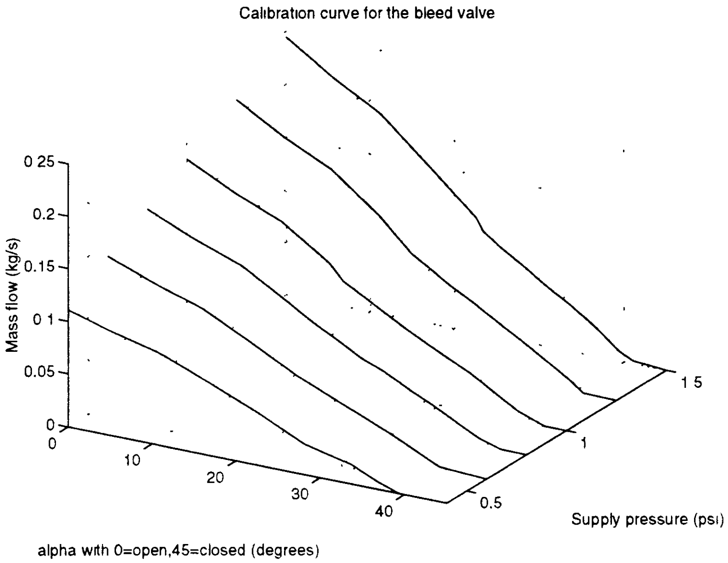

Figure 2-20: Calibration Test Results for the mass flow

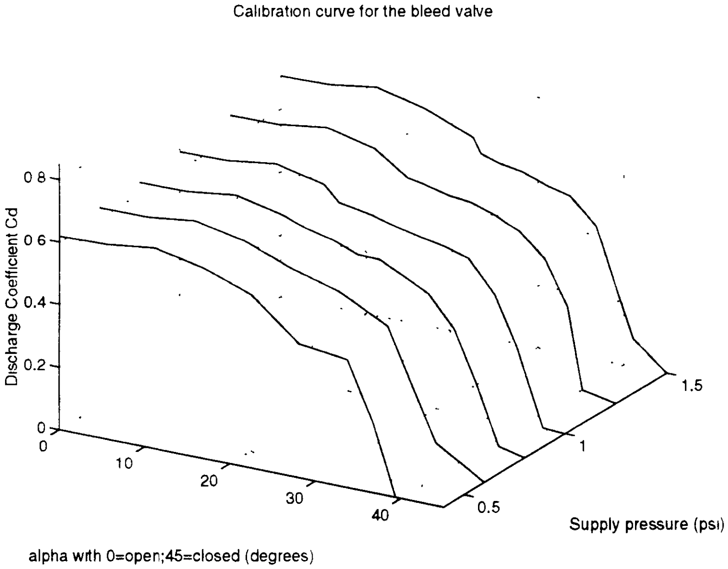

Figure 2-21: Calibration Test Results for the discharge coefficient

CHAPTER 3

EXPERIMENTAL FACILITY AND PROCEDURE

The experimental studies were all done on the MIT Gas Turbine Laboratory three-stage low-speed axial compressor rig. This chapter describes the compression system facility and the instrumentation. It also discusses the different measurement techniques and data reduction procedures.

3.1 History of the rig

The three-stage compressor was originally designed by United Technologies Research Center to study blading concepts for the JT9D. The compressor geometry and design parameters are presented in Table 3.1. This compressor was used by Eastland [3] to study rotating stall performance, then by Gamache [7] to look at reverse flow characteristics and Garnier [8] to investigate rotating stall inception. Haynes [11] gives a more detailed insight into the history and blading design of the compressor facility. Active control was first implemented on this rig by Haynes using twelve independent servo guide vanes equally distributed around an actuator ring, sandwiched between the IGV blade row and the first rotor of the compressor. Van Schalkwyk [27] added an extension to the compressor inlet to accommodate a slowly rotating distortion screen and investigated active control concepts with distortion added to the system.

The actuation ring was then modified for the installation of jet actuators and active control using jet actuators was tested by Vo [31]. Protz [26] added the plenum to experience and control rotating stall coupled with surge, using the same actuation scheme but in a non-linear way.

Facility Physical Parameters		**Compressor parameters**	
Density of air	$2.377e-03$ [$\frac{slug}{ft^3}$]	Tip Radius	12.000 [in]
Speed of Sound	$1.083e+03$ [$\frac{ft}{s}$]	Hub Radius	10.558 [in]
Atmospheric Pressure	14.696 [psig]	Mean Radius	11.279 [in]
Atmospheric Temperature	70.000 [deg F]	Rotor Frequency	2600.000 [rpm]
Bleed Valve parameters		Mean Wheel Speed	255.912 [ft/s]
Number of Valves	4 [nondim]	Rotor Dynamic Head	1.081 [psig]
Bleed Valve Area	3.4 [in^2]	Flow Velocity at Peak	125.44 [$\frac{ft}{s}$]
Bleed Valve Inertia	2.915e-02 [$kg.in^2$]	Mass Flow at Peak	5341.2208 [scfm]
Bleed Valve Diameter	3.3 [in]	Pressure rise at Peak	1.081 [psig]
		Design Reaction	0.75 [nondim]

Blading parameters				
	IGV	Stage 1	Stage 2	Stage 3
Rotor Chord [in]	–	1.780	1.764	1.996
Rotor Stagger [deg]	–	42.800	43.500	44.600
Rotor Mu [nondim]	–	0.215	0.216	0.249
Stator Chord [in]	0.791	1.236	1.232	1.236
Stator Stagger [deg]	8.100	11.000	12.000	5.500
Stator Mu [nondim]	0.071	0.112	0.112	0.110
Rotor Stator Gap [in]	–	0.7874	0.7874	0.7087
Rotor Stator Mu [nondim]	–	0.0698	0.0698	0.0628
Interstage Gap [in]	3.945	0.7874	0.7874	–
Interstage Mu [nondim]	0.3498	0.0698	0.0698	–

Other parameters	
Duct Area	102.192 [in^2]
Upstream Duct Length	33.750 [in]
Downstream Duct Length	$17.250 + L_d$ [in]
Compressor Length	26.250 [in]
Total Length	$77.250 + L_d$ [in]
Plenum Volume (High B)	341.264 [ft^3]

Table 3.1: GTL-LS3 design parameters

3.2 The compression system

The overall picture and description of the compression system before any change is depicted in Figure 2-1. For this project, all the injectors were turned off; the distortion screen was not used and the rig was modified to add an actuation ring with bleed valves and a downstream duct to improve the control power of bleed valve actuators.

3.2.1 The compressor

The compressor is shown in an unwrapped view in Figure 3-4.

3.2.2 The valves, actuation ring and downstream duct

For active control, the bleed valves whose design and testing are fully explained in Chapter 2 were installed on the rig. Four valves were installed. Although the actuation ring was designed to house as many as twelve actuators, the eight

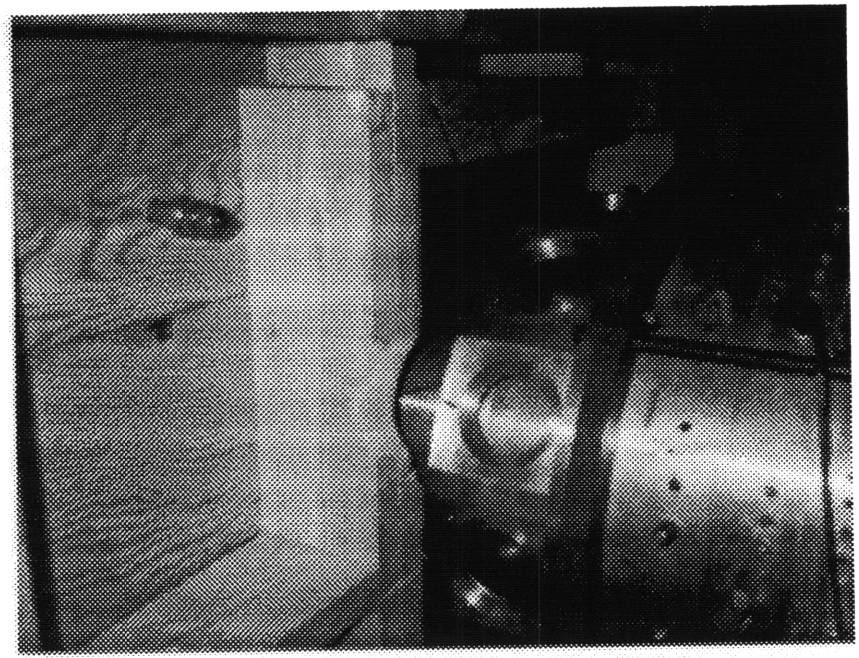

Figure 3-1: View of the actuation ring

remaining holes were closed by adequate plugs. This actuation ring, connected to the existing wooden plenum, is depicted in Figure 3-1.

A photograph of one of the actuators, which includes a motor, a rotory valve and a support frame is presented in Figure 3-2.

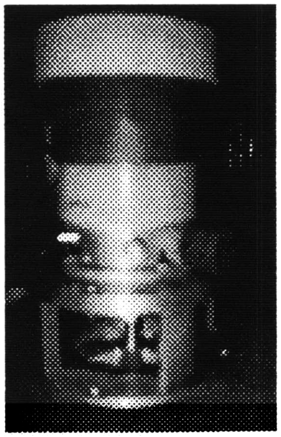

Figure 3-2: View of one actuator (system motor-valve)

The rotory valve is connected to the motor shaft and opens or closes, more or less, the counterpart holes in the support frame. A minimum clearance gap insures no rubbing and minimal leakage.

Detailed drawings of the valve, valve casing (which consists of three parts) and actuation ring are presented in Appendix A.

The downstream duct, whose length was chosen as detailed in Chapter 2, sits on a cradle inside the plenum. This can be seen in Figure 3-3.

The detailed drawings of the inner and outer duct of the downstream duct are also presented in Appendix A.

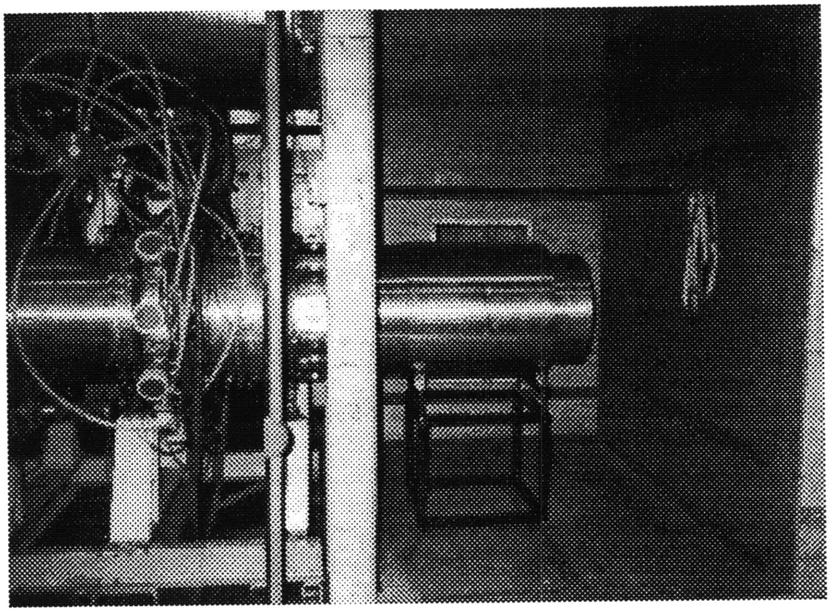

Figure 3-3: View of the system

3.2.3 The exhaust plenum and throttle

The compressor exhausts into a downstream plenum. Prior experiments used a small plenum throttled by a conical valve. The plenum was modified by Protz [26] in order to achieve a value of the B parameter high enough to introduce surge dynamics. The B parameter is proportional to the compressor rotor speed and to the square root of the plenum volume. Safety concerns limit the top compressor speed to 2600 RPM. At this speed the previous (see Ref. [31]) plenum gave a B parameter of only 0.18. J.M. Protz (see Ref. [26]) designed a new bigger plenum (by increasing the previous one by a factor of roughly 30). The plenum is a 113.50 in. x 83.50 in. x 61.75 in. plywood box with an internal volume of 340 cubic feet.

The downstream throttle regulates airflow out of the plenum. The throttle is a roller gate valve manufactured by Salina Vortex Corp. When fully open, the gate valve has an area of 144.0 square inches. A Warner Electric Electrotrak 100 motorized linear actuator moves the gate at the constant speed of 0.86 in/sec. A linear transducer and electronic amplifier measure the gate displacement as a percentage of fully open.

The sensor has an accuracy of +/- 0.015% of fully open. The actuator controls gate position with an accuracy of +/- 0.05 % of fully open. As is well known, once the compressor is stalled, the mass flow must be increased to clear the stall cell. The mass flow at which stall clears can be considerably higher than the stalling mass flow. This introduces a "hysteresis" in the throttle mass flows necessary to stall and unstall the compressor. The throttle mass flow is proportional to the throttle area and the square root of the plenum pressure. The throttle was designed so that its area when fully open is sufficient to allow the compressor to be unstalled during clean flow experiments. This was indeed the case during this project since the distortion generator was not used.

3.3 Instrumentation

The rig is configured with steady and unsteady sensors to measure local mass flow in the annulus and pressure in the plenum. Figure 3-4 shows the various sensor location in an "unwrapped" way. An analysis of the best sensor location is described in more detail in Chapter 4. In addition to the velocity and pressure probes, torque and rotor speed transducers are located at the compressor inlet.

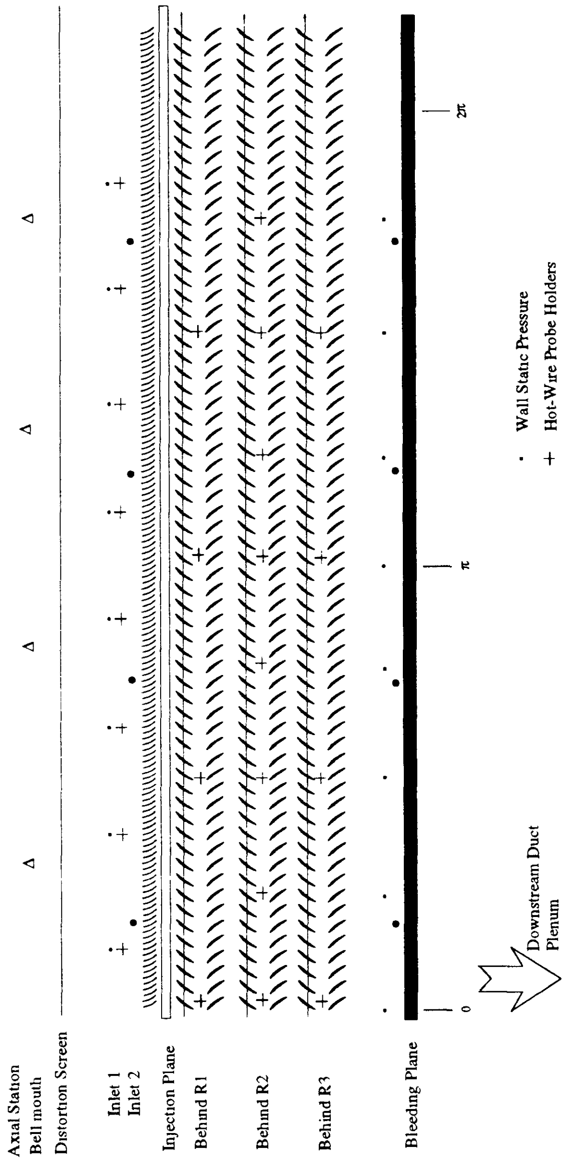
Axial Station
Bell mouth
Distortion Screen
Inlet 1
Inlet 2
Injection Plane
Behind R1
Behind R2
Behind R3
Bleeding Plane
0
π
2π
Downstream Duct
Plenum
· Wall Static Pressure
+ Hot-Wire Probe Holders
● Struts
◁ Total Pressure

Figure 3-4: Sensor Locations

3.3.1 Steady sensors

Steady pressure sensing

Steady pressure measurements were taken by a Scanivalve SSS-48C multi-port pressure sensing system. A stepping rate of 3 ports/sec was chosen (out of a maximum of 8 ports/sec) to allow the pressure to settle before reading. Bellmouth total pressure, bellmouth static pressure, compressor face static pressure, compressor face total pressure, compressor exit static pressure, plenum pressure and orifice plate pressure were measured by the Scanivalve sensing system (see exact location in Figure 3-4.

A calibration curve is used to determine the steady bellmouth mass flow from bellmouth pressure measurements. An MKS Baratron (accurate to within 0.2 Pa) was also available to measure the pressure across the orifice plate. A Scanivalve SDIU-MK3 interface unit controls the stepping of the SSS-48C and digitizes the pressure readings from the Scanivalve and the Baratron. The way the measurements were taken was time consuming since the SDIU-MK3 unit only takes a single measurement for each step of the Scanivalve port, which implied a long time lost in order to acquire multiple measurements for averaging.

The atmospheric pressure was measured at the beginning of each day of runs.

Steady temperature sensing

The two important temperature measurements are the ambient temperature, which is used to calculate the air density and the plenum temperature which was used to get the downstream throttle calibration curve. The ambient temperature was read off a mercury thermometer at the start of each hot-wire calibration run at the beginning and end of each experimental run. The accuracy is $+/-0.05^oC$. The plenum temperature and the bearing temperatures were monitored visually with Omega type K thermocouples and displays.

Torque and RPM measurement

A Lebow 1105H-5K slip ring torque sensor is installed on the compressor drive shaft. A Lebow 7530-100 signal conditioning unit provides the output in Volts. The accuracy is +/- 1 lb-in or 0.14 % of the operating torque. A 60 tooth gear and magnetic pick-up is provided with the torque-meter to permit rotational frequency measurement via a frequency counter with an accuracy of +/- 1 RPM.

3.3.2 Unsteady sensors

A single Druck 820 strain-gauge type pressure probe, located near the center of one plenum side wall, measured unsteady plenum pressure. The voltage drop across the Druck pressure probe gives a linear measure of gauge pressures up to 2.5 psi. The probe has a natural frequency of 28 kHz. The millivolt output of the probe is amplified using an Analog Devices AD2B31 filter. The probe is calibrated against the Scanivalve system at the beginning of each day of runs.

Two hot-wire arrays of eight probes, each equally distributed along the annulus, measure the unsteady mass flow in the compressor annulus. The first array is located at a distance of 0.6 times the mean compressor radius upstream of the inlet guide vanes. The other array is located at the first stage rotor-stator interstage gap. Each hot-wire anemometer consists of a Dantec 56C17 bridge and a Dantec 55-P11 hot-wire. They have a bandwidth of 50 kHz. The Dantec 55-P11 hot-wire probes have a 20 μm tungsten wire of 1.2 mm in length, placed at the mid-span of the annulus, which is the most effective radial location for detecting stall precursors as reported by Haynes [11]. The hot-wires were calibrated at the beginning of each experimental session. A prediction of the transfer functions of the system $(\frac{\text{velocity}}{\text{valve opening}})$ based on a theoretical model of the system showed that upstream (relative to the actuation) sensing is the one to choose since the surge dynamics give non-minimum phase zeros (which is undesirable for control) if downstream sensing is chosen. The derivation of the model and result of simulations is described in Chapter 4.

3.4 Data acquisition and control

An overall view of the data acquisition system is depicted in Figure 3-5. It shows the different subsystems and signal paths between the different blocks. Two computers are used for data acquisition. An industrial computer Pentium-133 PC acquires data from the unsteady sensors and implements the control loop. It also records the outputs of the unsteady sensors. This computer is responsible for the control logic and commands the inputs of the four high-speed servo-valves. The PC stores the unsteady data in a 16 second circular buffer.

An eight-channel Datel D/A (Digital to Analog) board allows the sensor signals to be output to an oscilloscope or spectrum analyzer. The PC Pentium-133 also samples the throttle position and controls the position of the throttle via the D/A system and relay box.

A Hewlett-Packard RS20 80386 PC records the steady data from the Scanivalve system. An RS232 serial port links both computers. During calibration, the link is used to synchronize data acquisition.

An analogic HSDAS-16 A/D (Analog to Digital) converter samples the unsteady sensor outputs. The 30 sensor signals are multiplexed to the 16 channels of the HSDAS-16 using a DASMUX-64 multiplexer. A total of 32 channels were sampled at a rate of 1 kHz. For additional details, consult Ref. [26] and [31].

All sensor signals were low-passed filtered to prevent aliasing. The output of the Druck pressure probe was amplified and filtered using an Analog Devices AD2B31 3-pole analog low-pass Bessel filter with a cutoff frequency of 500 Hz. All other signals were filtered using Frequency Devices 744 PL4-pole analog low-pass Bessel filters with unity gain and a cutoff frequency of 250 Hz.

The four high-speed bleed valves used in this project were driven by Pacific Scientific 4VM62-220-1 low inertia DC motors. The motors were controlled by DMC 430 digital PID servo-motion controllers. Each controller ran at a sampling rate of 2000

Hz., and the digital encoders have an accuracy of 4096 counts/rev. to measure valve opening position.

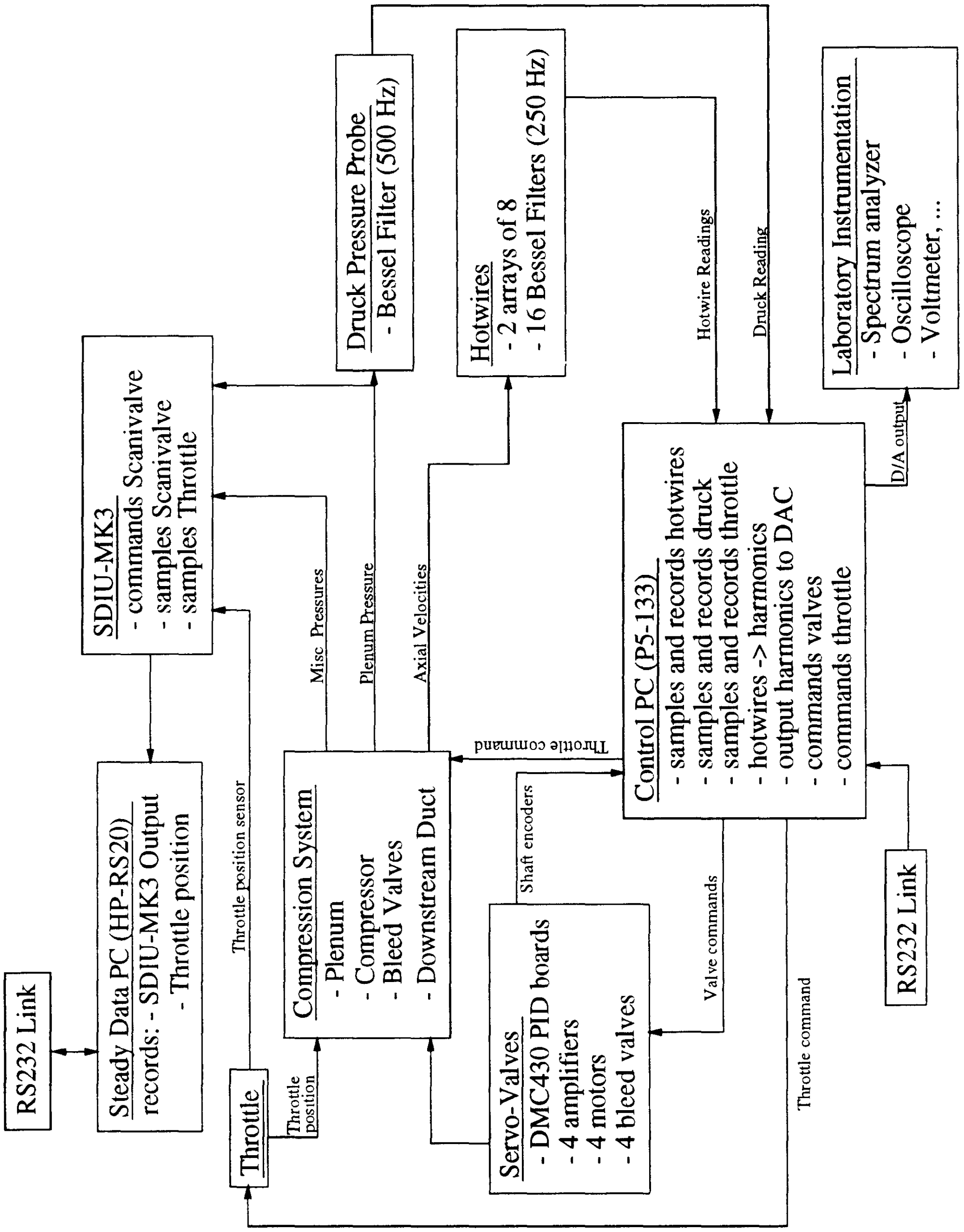
RS232 Link
Steady Data PC (HP-RS20)
records: - SDIU-MK3 Output
- Throttle position
SDIU-MK3
- commands Scanivalve
- samples Scanivalve
- samples Throttle
Throttle
Throttle position sensor
Throttle position
Compression System
- Plenum
- Compressor
- Bleed Valves
- Downstream Duct
Misc Pressures
Plenum Pressure
Axial Velocities
Druck Pressure Probe
- Bessel Filter (500 Hz)
Hotwires
- 2 arrays of 8
- 16 Bessel Filters (250 Hz)
Servo-Valves
- DMC430 PID boards
- 4 amplifiers
- 4 motors
- 4 bleed valves
Shaft encoders
Throttle command
Control PC (P5-133)
- samples and records hotwires
- samples and records druck
- samples and records throttle
- hotwires -> harmonics
- output harmonics to DAC
- commands valves
- commands throttle
Hotwire Readings
Druck Reading
Valve commands
Throttle command
Laboratory Instrumentation
- Spectrum analyzer
- Oscilloscope
- Voltmeter, ...
D/A output
RS232 Link

Figure 3-5: Data acquisition system

3.5 Calibration and Measurement Technique

3.5.1 Calibration Procedure

At the start of each day of runs, the hot-wires and unsteady pressure probes were calibrated against the Scanivalve system. The compressor was run at 750, 1400, 1800, and 2400 RPM. At each speed, the throttle was closed to five different positions between full open and the peak of the compressor characteristic. At each operating point, a ten second average of the unsteady sensor output was recorded. The Scanivalve output was also recorded. The unsteady sensors were calibrated against the steady sensors using these measurements.

The steady compressor mass flow (upstream) was measured using the steady bellmouth static and total pressures. The throttle was calibrated only once, using calibration against the steady bellmouth mass flow measurement with the bleed valves closed (plugged).

The Scanivalve output was also recorded. The unsteady sensors were calibrated against the steady sensors using these measurements.

The throttle behavior was modeled using the following relation for pressure loss across a sharp-edged orifice:

$$\dot{m} = \rho C_d A_{throt} \sqrt{\Delta P}, \tag{3.1}$$

where ΔP is the difference between the total pressure upstream and downstream of the throttle. The throttle regulates the flow from the plenum into the exhaust duct (see Figure 2-1). Atmospheric pressure was assumed in the exhaust duct. Using this assumption, ΔP is equivalent to the plenum pressure. The coefficient C_d was determined using an ordinary least square fit. Neglecting leakage in the plenum, the steady throttle mass flow equals the steady downstream (of the compressor) mass flow.

The throttle calibration is depicted in Figure 3-6. The throttle calibration curve was done only once after removing the four bleed valves and using plugs to close all the holes on the actuation ring. This allowed the bellmouth mass flow to be equated with the downstream mass flow. The throttle calibration is depicted in Figure 3-6. This curve, along with equation 3.1, was used each time mass flow downstream of the bleed valves) was to be assessed.

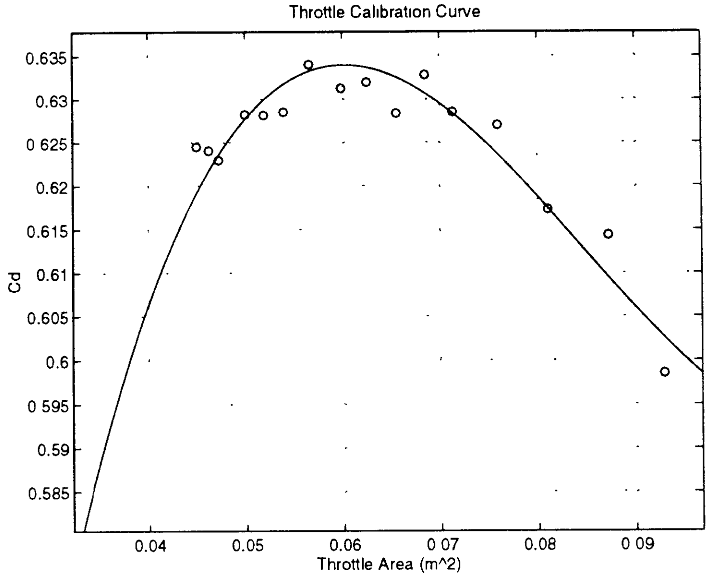

Figure 3-6: Throttle Calibration Curve

Since all the experiments were done with clean inlet flow, the hot-wires were calibrated against the steady bellmouth mass flow measurements. The bellmouth mass flow was divided by density and compressor area to give an annulus averaged velocity. King's law was used to determine the hot-wire voltage, v, for a given velocity, u.

$$v = (c_o + c_1|u|)^{c_3} \tag{3.2}$$

The calibration coefficients were determined using a nonlinear least squares routine as outlined in [27]. The calibration covered velocities between 0 ft/s and 200 ft/s, giving a minimum flow coefficient range of 0-0.8 at a rotor speed of 2600 RPM.

3.5.2 Stalling Mass Flow Measurement

The stalling mass flow was measured by slowly stepping the throttle closed until the compressor entered stall. At each step of the throttle, the upstream mass flow (compressor mass flow), throttle position and discharge coefficient were measured. The lowest measured throttle position prior to stall was considered the stall point. Three different mass flows are available at the stall point:

1. Bellmouth mass flow
2. Orifice plate mass flow
3. Throttle mass flow

The bellmouth mass flow is used for calibration and upstream compressor mass flow measurement. This mass flow is calculated from the Scanivalve pressure measurements using a bellmouth calibration curve.

The orifice plate mass flow is calculated from Scanivalve or Baratron measurements of the steady static pressure drop across the orifice using an orifice plate calibration curve.

The downstream steady mass flow through the throttle was calculated using the plenum pressure, the throttle position, and the throttle calibration curve. The throttle area was controlled to within +/- 0.05 % of the fully open area. Accounting for the errors in throttle area and the plenum pressure measurement, the stalling throttle mass flow measurement has an error of +/- 0.5 %. For additional details on these measurements, see Ref. [31].

The throttle and the orifice plate both measure the downstream mass flow. The throttle measurement was chosen since it can give both steady and unsteady mass flow measurements. Also, the measurements of the orifice plate mass flow were subject to sporadic errors.

3.5.3 Unsteady Mass Flow Measurement

The compressor unsteady annulus average mass flow measurement is done by two means.

- hot-wire spatial averaging:

  This method is very easy to implement and practical during control runs. Indeed, the averaging can easily be done in real time. According to Protz [26], this method gives good results for unsteady flow velocities in the range of 65-200 ft/sec.

- plenum mass conservation:

  This method was only used for post-run data processing since it requires extensive signal processing. The principle of this technique is to measure the instantaneous rate of change of mass in the plenum. This rate must equal the sum of the mass flow through the compressor and throttle. Since the throttle mass flow is known from the throttle calibration curve, one can solve for an estimate of the compressor mass flow. Assuming isentropic compression in the plenum, one finds:

  $$\dot{m}_c = \frac{V_p}{\gamma RT}\dot{p} \tag{3.3}$$

  where V_p is the plenum volume; p and T are respectively the plenum pressure and plenum temperature. The annulus average velocity being $\overline{C}_x = \frac{\dot{m}_C}{\rho A_c}$. A steady temperature measure was enough since the temperature does not fluctuate significantly during a typical surge event. The unsteady plenum pressure measurements had substantial noise at and above the rotor frequency. Because the estimation method requires the derivative of the plenum pressure, the Druck pressure probe output was low-pass filtered. After the data for a given run was acquired, the pressure measurements were filtered using a four-pole forward-backward Butterworth filter with a cut-off frequency of 17Hz. More details about this procedure can be found in [26], as well as in Greitzer [9].

CHAPTER 4

THEORETICAL MODEL

In this chapter, a theoretical model of the compression system is presented. It is a nonlinear two-dimensional model with the addition of bleed valves as the actuation. Distortion is not considered here. The original Moore-Greitzer model [21] is the template for this analysis. The linearized version of the model is then used as a tool to state the "optimal" sensor location by computing the transfer functions between the sensor and the actuation. This analysis is performed fo the zeroth as well as higher harmonics.

4.1 General 2D Bleed Model

A sketch of the compression system is depicted in Figure 4-1.

The model is based on a component by component analysis. Each component is described by a pressure-difference equation. The final overall model is found by assembling the components of the system. There are five elements to account for in the analysis before putting them together:

- Upstream Duct, upstream flow field
- Downstream Duct, downstream flow field

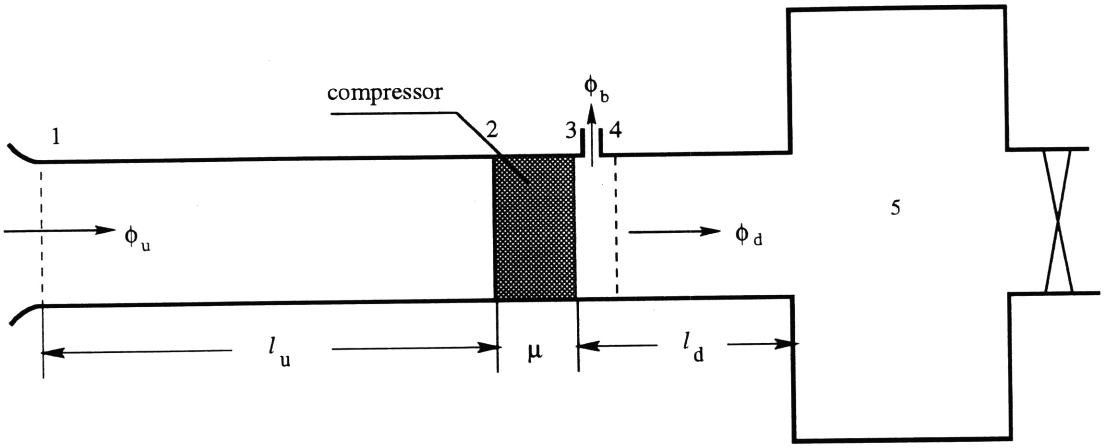

Figure 4-1: Sketch of the compression System

- Across the Compressor
- Bleed valves
- Plenum-Throttle

For the remainder of this Chapter, notation is as defined in Section 2.2.1 and any new notation will be described.

4.1.1 Upstream Duct - Upstream Flow Field

The flow in the upstream duct is assumed to be incompressible and potential. The unsteady Bernoulli equation (see [21]) gives:

$$\frac{P_{t1} - P_{t2}}{\rho U^2} = \frac{\partial(\delta\Phi)}{\partial t} + l_u \frac{\partial \bar{\phi}_u}{\partial t} \tag{4.1}$$

where P_{t1} and P_{t2} are dimensional total pressure at stations 1 and 2 respectively; $\delta\Phi$ is the potential of the non-axisymmetric velocity disturbances; $\bar{\phi}_u$ is the non-dimensional upstream velocity.

4.1.2 Downstream Duct - Downstream Flow Field

The flow is assumed to exit the compressor axially and circumferentially uniformly. According to the Moore and Greitzer's model derivation, the equation for the downstream flow field is similar to that for the upstream flow.

$$\frac{P_5 - P_4}{\rho U^2} = -l_d \frac{\partial \bar{\phi}_d}{\partial t} - (m-1)[\frac{\partial \delta \Phi}{\partial t}]_{\eta=0} \tag{4.2}$$

Where P_4 and P_5 are the dimensional static pressure at stations 4 and 5 respectively; m is called the pressure redistribution parameter and takes value 2.0 for a long duct and 1.0 for a short duct. In our case, the value 2.0 will be used.

4.1.3 Across the compressor

The compressor blade-row model used by Moore and Greitzer will be used to model the compressor as a semi-actuator disk. That means that the inertia of the fluid in the blade passages will be taken into account in the compressor pressure rise.

$$\frac{P_3 - P_{t2}}{\rho U^2} = \Psi_c(\phi_u) - \lambda \frac{\partial \phi_u}{\partial \theta}|_{\eta=0} - \mu \frac{\partial \phi_u}{\partial t}|_{\eta=o} \tag{4.3}$$

Where P_3 and P_{t2} are respectively dimensional static pressure at station 3 and dimensional total pressure at station 2, μ is the cumulative fluid inertia of all the blade-rows and λ is the cumulative fluid inertia of the rotors only. $\Psi_c(\phi_u)$ is the total-to-static empirical pressure rise across the compressor as a function of local mass flow and accounts for the cumulative pressure change due to ideal turning, deviation, and blade-row losses.

4.1.4 Bleed Valve relation

The flow field in the region near the bleed valve is very complex. It would have been useful to have velocity profile or CFD computations of the flow field in this region. However, this type of investigation is beyond the scope of this research. For the present analysis, the model will consider mass flow and momentum removal due to the bleed valve. The bleed valves are then treated as an actuator disk that removes mass and momentum. Figure 5-5 is a simple view of the bleed region.

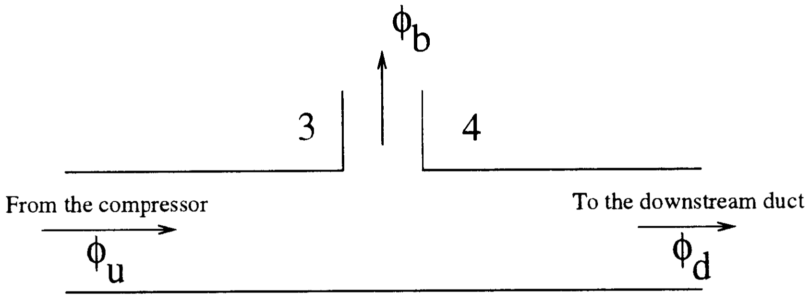

Figure 4-2: Bleed region

The continuity equation gives:

$$\phi_4 = \phi_3 - \phi_b \tag{4.4}$$

with, $\phi_b = \dfrac{A_b u_b}{AU}$

For the momentum removal, we use the assumption of incompressible, inviscid flow, such that the Bernoulli equation can be used and gives:

$$P_3 + \frac{1}{2}\rho {u_3}^2 = P_4 + \frac{1}{2}\rho {u_4}^2 = P_b + \frac{1}{2}\rho {u_b}^2 \tag{4.5}$$

After nondimensionalization by ρU^2 for the pressures and $A_c U$ for the mass flows (see Section 2.2.1), and a small algebraic treatment, we find the pressure difference across the bleed valve due to momentum removal:

$$\psi_4 - \psi_3 = \phi_3\phi_b - \frac{1}{2}\phi_b^2 \tag{4.6}$$

As usually assumed for the throttle (see Section 2.2.1), a quadratic characteristic is used for the bleed valve:

$$\phi_b = \gamma\sqrt{\psi_3} \tag{4.7}$$

4.1.5 Plenum-throttle relations

The plenum is modeled as a spatially uniform isentropic air spring of relatively large volume, such that fluid velocities are negligible. The rate of change in pressure in such a system is given by the relation (see Ref. [9]):

$$\frac{d\psi}{dt} = \frac{1}{4l_c B^2}[\bar{\phi}_d - \phi_T(\psi)] \tag{4.8}$$

Where B is the Greitzer's system stability parameter and $l_c = l_u + l_d + \mu$ is the total nondimensional effective length of the compression system; and with ϕ_t coming from the throttle characteristic. The throttle is assumed to have a quadratic behavior:

$$\phi_t = \sqrt{\frac{2\psi}{K_t}} \tag{4.9}$$

4.1.6 Overall system of equations

Pressure balance before the valves

Adding equations 4.1 and 4.3, one finds:

$$\frac{\partial(\delta\Phi)}{\partial t} + l_u\frac{\partial\bar{\phi}_u}{\partial t} + \lambda\frac{\partial\delta\phi_u}{\partial\theta} + \mu\frac{\partial\delta\phi_u}{\partial t} = \psi_c(\phi_u) - \psi_3 \tag{4.10}$$

Pressure balance after the valves

Rewriting 4.2, one finds:

$$\frac{\partial\delta\Phi}{\partial t} + l_d\frac{\bar{\phi}_d}{dt} = \psi_4 - \psi \tag{4.11}$$

with, $\psi_5 = \psi$.

Separation of the variables

Let's separate the variables that have a circumferential distribution into their mean and perturbation components for linearization purposes. That gives:

$\phi = \bar{\phi} + \delta\phi$
$\phi_b = \bar{\phi}_b + \delta\phi_b$
$\psi_c = \bar{\psi}_c + \delta\psi_c$
$\gamma = \bar{\gamma} + \delta\gamma$
$\delta\phi = \sum_{n>0}\tilde{\phi}_n e^{in\theta}$
$\dfrac{\partial\delta\Phi}{\partial t} = \sum_{n>0}\frac{1}{\lvert n\rvert}\dfrac{d\tilde{\phi}_n}{dt}e^{in\theta}$
$\delta\phi_b = \sum_{n>0}\tilde{\phi}_{b,n}e^{in\theta}$
$\delta\gamma = \sum_{n>0}\tilde{\gamma}_n e^{in\theta}$
$\delta L_r = \sum_{n>0}L_{r,n}e^{in\theta}$
$\delta L_s = \sum_{n>0}L_{s,n}e^{in\theta}$

Table 4.1: Separation of variables in the model

For the compressor pressure rise, the derivation of the Moore-Greitzer model with unsteady losses is used. This takes into account the ideal pressure rise of the compressor and the viscous losses in the rotors and stators. Two additional equations account for the time lag associated with the viscous losses (see Paduano [18]). That gives:

$$\begin{cases} \delta\psi_c = \dfrac{d\psi_i}{d\phi}\delta\phi - \delta L_r - \delta L_s \\ \tau_s\dfrac{\partial\delta L_s}{\partial t} = \dfrac{dL_{s,ss}}{d\phi}\delta\phi - \delta L_s \\ \tau_r(\dfrac{\partial\delta L_r}{\partial t} + \dfrac{\partial\delta L_r}{\partial\theta}) = \dfrac{dL_{r,ss}}{d\phi}\delta\phi - \delta L_r \end{cases} \tag{4.12}$$

System of equations

After algebraic manipulations of the equations 4.6, 4.8, 4.10, 4.11 and 4.12 and using the separations of variables in table 4.1, we get the following systems:

Surge Dynamics:

$$\begin{cases} l_u\dot{\bar{\phi}} = \psi_c(\bar{\phi}) - \psi_b \\ \dot{\psi} = \dfrac{1}{4l_cB^2}\left(\bar{\phi} - \bar{\phi}_b - \sqrt{\frac{2}{K_t}\psi}\right) \\ l_d\dot{\bar{\phi}}_b = \dfrac{l_d}{l_u}\bar{\psi}_c + \psi - \bar{\phi}\bar{\phi}_b + \dfrac{1}{2}\bar{\phi}_b^2 - \dfrac{l_c}{l_u}\psi_b \end{cases} \tag{4.13}$$

Higher Mode Dynamics – Rotating Stall:

$$\begin{cases} (\mu + \tfrac{2}{n})\dot{\tilde{\phi}}_n - i\lambda n\tilde{\phi}_n = \dfrac{d\psi_i}{d\phi}\tilde{\phi}_n - \tilde{L}_{r,n} - \tilde{L}_{s,n} + \bar{\phi}\tilde{\phi}_{b,n} \\ \qquad\qquad\qquad\qquad + \bar{\phi}_b\tilde{\phi}_n - \bar{\phi}_b\tilde{\phi}_{b,n} + \tfrac{1}{n}\dot{\tilde{\phi}}_{b,n} \\ \tau_s\dot{\tilde{L}}_{s,n} = \dfrac{dL_{s,ss}}{d\phi}\tilde{\phi}_n - \tilde{L}_{s,n} \\ \tau_r\dot{\tilde{L}}_{r,n} - in\tilde{L}_{r,n} = \dfrac{dL_{r,ss}}{d\phi}\tilde{\phi}_n - \tilde{L}_{r,n} \end{cases} \qquad (4.14)$$

At this point, we split the analysis between the surge part of the dynamics and its rotating stall part.

4.1.7 Surge Dynamics Analysis

In this section, a theoretical linear analysis of the one-dimensional behavior of the four bleed-valve actuation scheme is described. The idea is to consider surge only, use the system of equations 4.13 for the surge dynamics and linearize it. In all the equations in this "surge" section, the sign "-" overlining the averaged quantities will be omitted for clarity of the writing since surge only is considered here. Let's detail one example of linearization; the other terms being linearized in a similar manner.

$$\psi_b = \frac{{\phi_b}^2}{\gamma^2}$$

$$\psi_b = \frac{(\phi_b + \delta\phi_b)^2}{(\gamma + \delta\gamma)^2}$$

Removing the second order terms,

$$\psi_b = \frac{(\phi_b + 2\phi_b\delta\phi_b)}{\gamma^2(1+\frac{\delta\gamma}{\gamma})^2}$$

Using Taylor expansion to the first order, this derivation finally gives:

$$\delta\psi_b = 2\frac{\phi_b\delta\phi_b}{\gamma^2} - 2\frac{{\phi_b}^2\delta\gamma}{\gamma}$$

The term $\psi_c(\phi)$ is linearized in this manner:

$$\psi_c(\bar{\phi}) = \psi_c(\bar{\bar{\phi}} + \delta\bar{\phi}) \cong \psi_c(\bar{\bar{\phi}}) + \frac{\partial\psi_c}{\partial\bar{\phi}}\delta\bar{\phi}$$

with the notation $\frac{\partial\psi_c}{\partial\bar{\phi}} = m_c$.

Hence, after linearization, the surge dynamics can be written in state-space form:

$$\begin{cases} \frac{dx_1}{dt} &= A_{11}x_1 + A_{12}x_2 + A_{13}x_3 + B_1u \\ \frac{dx_2}{dt} &= A_{21}x_1 + A_{22}x_2 + A_{23}x_3 + B_2u \\ \frac{dx_3}{dt} &= A_{31}x_1 + A_{23}x_2 + A_{33}X_3 + B_3u \\ \\ y &= C_1x_1 + C_2x_2 + C_3x_3 + Du \end{cases} \qquad (4.15)$$

For this analysis, two variables were considered as the output y: the upstream averaged mass flow perturbation ($\delta\phi$) and the downstream averaged mass flow perturbation ($\delta\phi_d = \delta\phi - \delta\phi_b$).

The other quantities in equation 4.15 are described in Table 4.2.

$x_1 = \delta\phi$	$x_2 = \delta\psi$	$x_3 = \delta\phi_b$	$u = \delta\gamma$
$A_{11} = \frac{m_c}{l_u}$	$A_{12} = 0$	$A_{13} = -2\frac{\bar{\phi}_b}{l_u\bar{\gamma}^2}$	$B_1 = 2\frac{\bar{\phi}_b^2}{l_u\bar{\gamma}^3}$
$A_{21} = \frac{1}{4l_cB^2}$	$A_{22} = -\frac{1}{4l_cB^2\sqrt{2K_t\bar{\psi}}}$	$A_{23} = -\frac{1}{4l_cB^2}$	$B_2 = 0$
$A_{31} = \frac{m_c}{l_u} - \bar{\phi}_b$	$A_{32} = \frac{1}{l_d}$	$A_{33} = \bar{\phi}_b - \bar{\phi} - \frac{2l_c}{l_ul_d\bar{\gamma}^2}$	$B_3 = \frac{2l_c}{l_ul_d}\frac{\bar{\phi}_b^2}{\bar{\gamma}^3}$
$C_{1,us} = 1$	$C_{2,us} = 0$	$C_{3,us} = 0$	$D = 0$
$C_{1,ds} = 1$	$C_{2,ds} = 0$	$C_{3,ds} = -1$	$D = 0$

Table 4.2: Surge linearization

The vectors C_{us} and C_{ds} respectively give the outputs $y_{us} = \delta\phi_{upstream}$ and $y_{ds} = \delta\phi_{downstream}$.

4.1.8 Rotating Stall Analysis

From equation 4.14, we get the following equation after taking the Laplace transform:

$$(\mu + \frac{2}{n})\ s\ \tilde{\phi}_n - i\lambda n\tilde{\phi}_n = \frac{d\psi_\imath}{d\phi}\tilde{\phi}_n - \tilde{L}_{r,n} - \tilde{L}_{s,n} + \bar{\phi}\tilde{\phi}_{b,n} + \bar{\phi}_b\tilde{\phi}_n - \bar{\phi}_b\tilde{\phi}_{b,n} + \frac{1}{n}\ s\ \tilde{\phi}_{b,n} \tag{4.16}$$

Bleed Characteristic Linearization

We had:

$$\phi_b = \gamma\sqrt{\psi_3}$$

For linearization:

$$\phi_b + \delta\phi_b = (\bar{\gamma} + \delta\gamma)(\sqrt{\bar{\psi}_b} + \frac{1}{2\sqrt{\bar{\psi}_b}}\delta\bar{\psi}_b)$$

$$\Longrightarrow \delta\phi_b = \delta\gamma\sqrt{\bar{\psi}_b} + \frac{\bar{\gamma}}{2\sqrt{\bar{\psi}_b}}\delta\psi_b$$

Now we use the assumptions that:

- The bleed valves actuators are located about one radius downstream of the last stage of the compressor; therefore, any circumferentially nonuniform pressure perturbation is damped at the location of the actuation → $\delta\psi_b \cong 0$.

- Some lag in bleed flow must exist and that will be taken into account with a first order lag system.

Then, we have, after taking the Laplace transform:

$$\tilde{\phi}_{b,n} = \sqrt{\bar{\psi}_b}\frac{\tilde{\gamma}_n}{\tau_b s + 1} \tag{4.17}$$

4.2 Transfer Functions Results - Sensor Locations

4.2.1 Surge Transfer Functions

In Section 4.1.7, the surge dynamics were put in a SISO form. This SISO form allows us to get the transfer function between the output y (y_{us} or y_{ds}) and the input $\delta\gamma$.

Indeed, from the form,

$$\begin{cases} \dot{x} = & A.x + B.u \\ y = & C.x \end{cases} \tag{4.18}$$

it follows after having taken the Laplace transform:

$$\frac{Y(s)}{U(s)} = C.(sI - A)^{-1}.B \tag{4.19}$$

The values of the parameters used in this analysis are shown in Table 4.3.

l_u	6.85
l_d	3.85
$\bar{\phi}$	0.46
m_c	-1
$\bar{\phi}_b$	0.0464
$\bar{\gamma}$	0.0483
ψ	0.95
B (2400 RPM)	0.85

Table 4.3: Surge model parameters

The pole-zero map of both upstream and downstream transfer functions are depicted in Figure 4-3 with a zooming near the origin in Figure 4-4.

This analysis gives a way to choose the sensor location for surge control. After deriving the transfer functions from the actuation to the sensing for the two situations (upstream and downstream sensing), one can use it to qualitatively find the sensor location to avoid in terms of bad closed loop behavior.

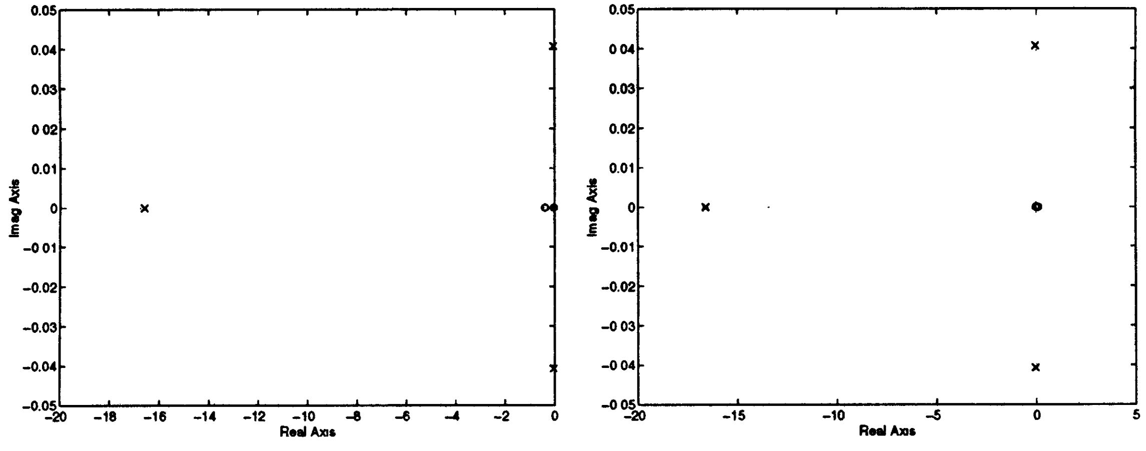

(a) Pole-Zero Map:upstream sensing

(b) Pole-Zero Map:downstream sensing

Figure 4-3: Pole-Zero Map: Surge dynamics

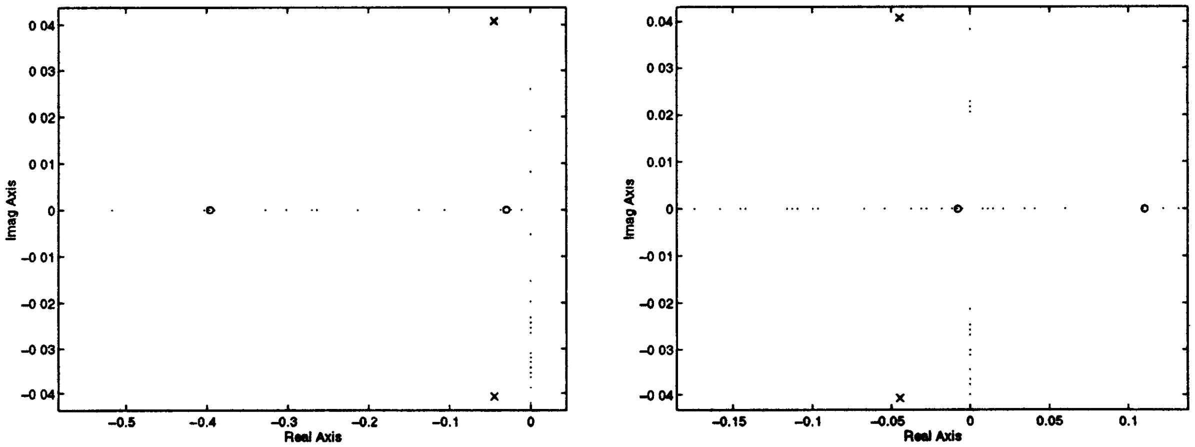

(a) Pole-Zero Map:upstream sensing

(b) Pole-Zero Map:downstream sensing

Figure 4-4: Pole-Zero Map Zoomed: Surge dynamics

One can see that in the case of downstream sensing, the surge dynamics present a non-minimum phase zero close to the origin, which is never a good sign for the closed loop behavior. For that reason, upstream (of the bleed valves location) sensing was chosen.

A comparison with surge transfer functions from Protz [26] can be made. In the case with no downstream duct and with injection as the actuation, the experimental and modeled results for the surge dynamics gave a surge frequency (Protz's model: 2.4 Hz.; Protz's experiments: 2.8 Hz.) higher than in this case (Bleed model: 1.7 Hz; Experiments (see Chapter 5): 1.8 Hz) . This is easy to understand since the added downstream duct increases the fluid inertia of the system which slows down the surge dynamics.

Another comparison can be made. Protz's poles-zeros map show a non-minimum phase zero in the case of downstream sensing and minimum phase zero in the case of upstream sensing which is the opposite in the case of bleed actuation. That is once again explainable by looking at the actuation physics. The one-dimensional effect of injection is to add mass to the flow, whereas bleeding has the effect of removing mass from the flow. That means that what is sensed upstream of the actuation in the case of injection is similar to what is sensed downstream of the actuation in the case of bleed actuation.

Another discussion of the model results will be detailed In Chapter 5 where a comparison of the model with experiments on the rig will give a quantitative validation of this model of bleed actuation.

4.2.2 Rotating Stall Transfer Functions

Since this is the first time 2D bleed actuation has been attempted and since the primary goal of this research thesis is to demonstrate the 2D effectiveness of the asymmetric bleed actuation, the efforts of this first analysis will be on first mode excitation and effect (n=1).

The last two equations of the system 4.14 give, after taking the Laplace transform:

$$\widetilde{L}_{s,n} = \frac{\frac{dL_{s,ss}}{d\phi}\widetilde{\phi}_n}{\tau_s s + 1}$$

and,

$$\tilde{L}_{r,n} = \frac{\frac{dL_{r,ss}}{d\phi}\tilde{\phi}_n}{\tau_r s + 1 - in}$$

Using these last two equations with 4.16 and using the notation in Table 4.4 and the linearized bleed characteristic and lag in equation 4.17, it follows:

$$\frac{\tilde{\phi}_n}{\tilde{\gamma}_n} = \frac{\sqrt{\bar{\psi}_b}}{\tau_b s + 1} \frac{\frac{s}{n} + \bar{\phi} - \bar{\phi}_b}{\xi s - K_i + \frac{K_s}{\tau_s s + 1} + \frac{K_r}{\tau_r s + 1 - in}}$$

$$= \frac{\sqrt{\bar{\psi}_b}}{\tau_b s + 1} \frac{(\frac{s}{n} + \bar{\phi} - \bar{\phi}_b)(\tau_s s + 1)(\tau_r s + 1 - in)}{(\xi s - K_i)(\tau_s s + 1)(\tau_r s + 1 - in) + K_s(\tau_r s + 1 - in) + K_r(\tau_s s + 1)} \tag{4.20}$$

The values of the parameters used in this analysis are shown in Table 4.5.

$$\begin{aligned} K_i &= \frac{d\psi_i}{d\phi} + i\lambda n + \bar{\phi}_b \\ K_s &= \frac{dL_{s,ss}}{d\phi} \\ K_r &= \frac{dL_{r,ss}}{d\phi} \\ \xi &= \mu + \frac{1}{n} \end{aligned}$$

Table 4.4: Rotating stall notation

n	=	1	μ	=	1.2937
λ	=	0.6787	$\frac{d\psi_i}{d\phi}$	=	-3.1
K_r	=	-1.8	K_s	=	-0.5
τ_s	=	2.85	τ_r	=	2.85
τ_b	=	0.6	$\bar{\phi}$	=	0.46
$\bar{\phi}_b$	=	0.0464	$\bar{\psi}_b$	=	0.95

Table 4.5: Higher mode analysis parameters

A more complete study of the first mode behavior with varying throttle position is depicted in Figure 4-5.

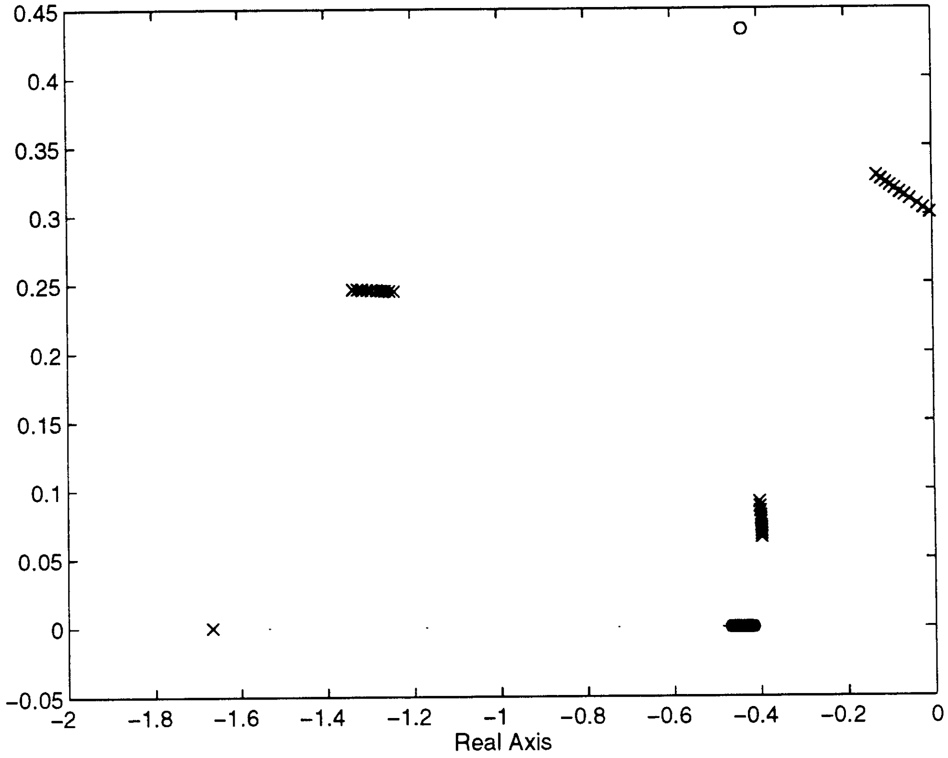

Figure 4-5: Pole-Zero Map with throttle closing (Upstream sensing)

The same analysis can be done for the case of downstream sensing with the transfer function being:

$$\frac{\widetilde{\phi}_{d,n}}{\widetilde{\gamma}_n} = \frac{\widetilde{\phi}_n - \widetilde{\phi}_{b,n}}{\widetilde{\gamma}_n} \tag{4.21}$$

The pole-zero map (see Figure 4-6) for the first harmonic response with downstream sensing shows that as the throttle is closed, the zero close to the dominant pole becomes non-minimum phase which is undesirable as stressed in the previous section. We see then, that the upstream sensing location is also the one to choose in this case.

Comparisons of these theoretical results with experimental results will be presented in Chapter 5. Overall effectiveness will also be discussed in Chapter 5.

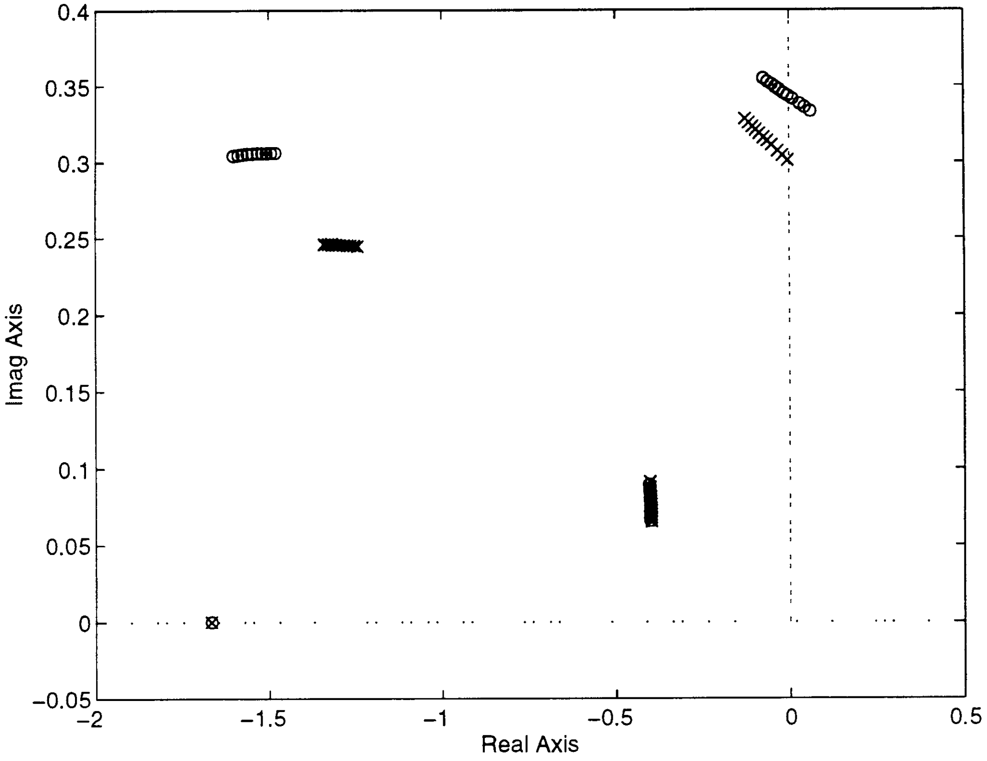

Figure 4-6: Pole-Zero Map with throttle closing (Downstream sensing)

CHAPTER 5

EXPERIMENTAL RESULTS

In this chapter, the experimental results are presented. The first section presents the open loop experimental results without actuation: the steady behavior of the system, the unsteady surge-stall coupling behavior and the unsteady pre-stall behavior. Section 2 presents the transfer functions measurements of the actuated system for both surge and rotating stall dynamics, along with a comparison with the model predictions presented in Chapter 4. Section 3 presents the control results.

5.1 Open-loop behavior of the unactuated system

This section describes the open-loop performance of the GTL-LS3, including the effect of the bleed valves and the downstream duct. Three aspects of the open-loop behavior were investigated. The first is the effect of bleed on the speedlines. The second is the effect of the downstream duct on the surge-stall transients. The third is the pre-stall behavior without control.

5.1.1 Steady Behavior – Speedlines

Figures 5-1 and 5-2 give the speedlines as well as the non dimensionalized plenum pressure against the upstream nondimensionalized mass flow. They respectively represent the case of fully closed bleed valves and the one of fully open bleed valves.

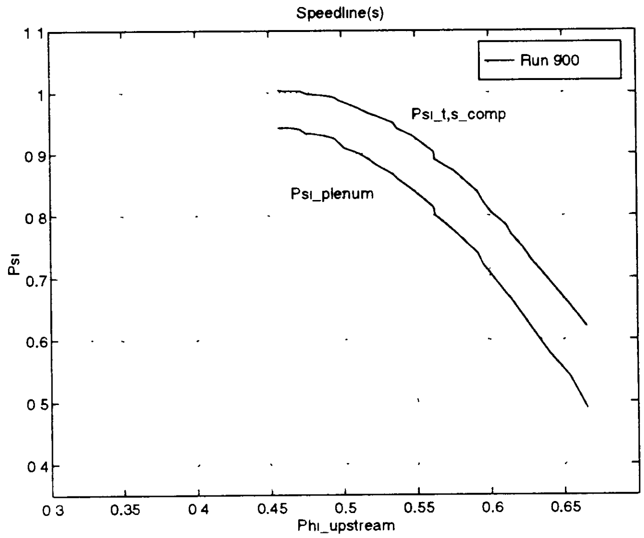

Figure 5-1: Compressor speedline & Plenum pressure – Fully closed bleed valves

The plenum pressure was expected to be higher in the case of fully open bleed valves. Indeed, for the same upstream mass flow, the throttle downstream of the plenum has to be more closed in the case of fully open bleed valve. This increases the resistance between the plenum and the exhaust duct, which causes the plenum pressure to rise.

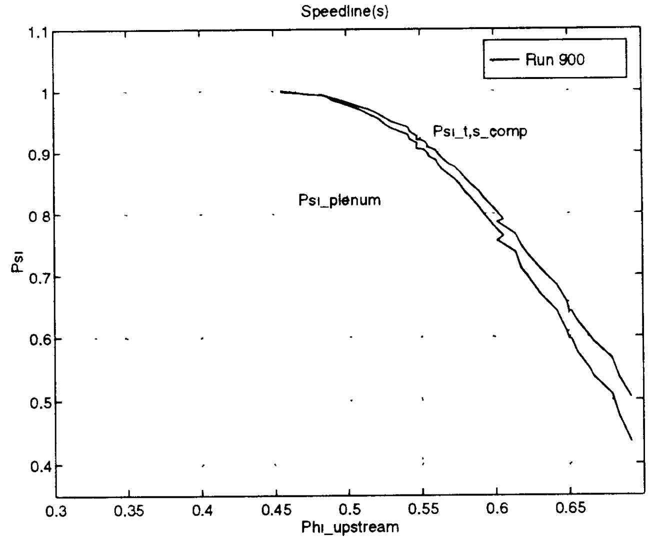

Figure 5-2: Compressor speedline & Plenum pressure – Fully open bleed valves

On the other hand, both total-to-static compressor pressure rise speedlines are the same since the presence of bleed valve downstream of the compressor doesn't affect the compressor pressure rise.

Another observation is the absence of range extension due to a steady bleed effect.

From Figures 5-1 and 5-2, the pressure rise due to a complete opening of the valves, can be assessed from the difference in plenum pressure from both plots. Indeed, everything else being the same (cf. the total-to-static compressor pressure rise being identical), the rise in plenum pressure is uniquely due to the opening of the valve.

Bleed pressure rise changes with upstream mass flow and can be compared to the bleed model steady state behavior (see relation 4.6). In this relation, ϕ_b was computed from the flow charts (see figures 2-14 to 2-19) assuming the bleed supply pressure equal to the static pressure just downstream of the compressor, also coming from Figure 5-1. This is depicted in Figure 5-3.

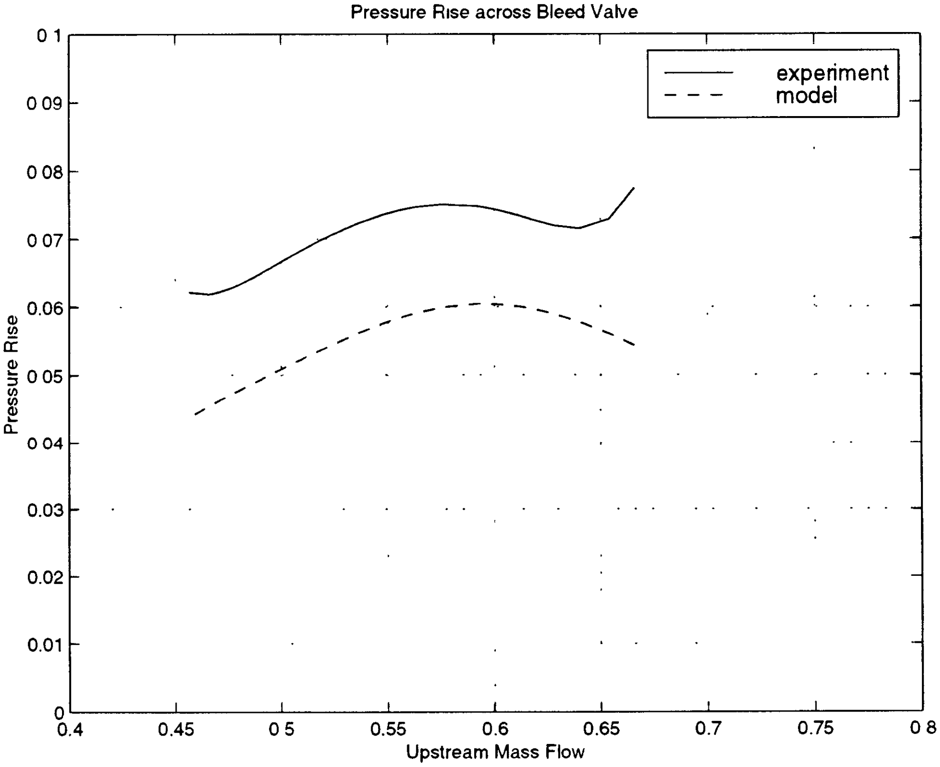

Figure 5-3: Comparison between experimental and model pressure rise across the fully open bleed valves

From Figure 5-3, we see that the bleed pressure difference is underestimated by the model. However, the trend when upstream mass flow varies is very well captured by the model.

5.1.2 Unsteady Behavior – Transients Analysis

Surge-Stall Interaction

In Chapter 3, we saw that one of the design requirements was to keep the surge ability of the compression system without actuation. Transients analysis runs were thus done in order to quantify this ability to surge. Whereas deep surge was not reached, coupling between surge and rotating stall was clearly demonstrated during these runs. Figure 5-4 shows the averaged mass flow and plenum pressure transients at 2400 RPM with time. The surge component of the instability is clearly demonstrated in this figure.

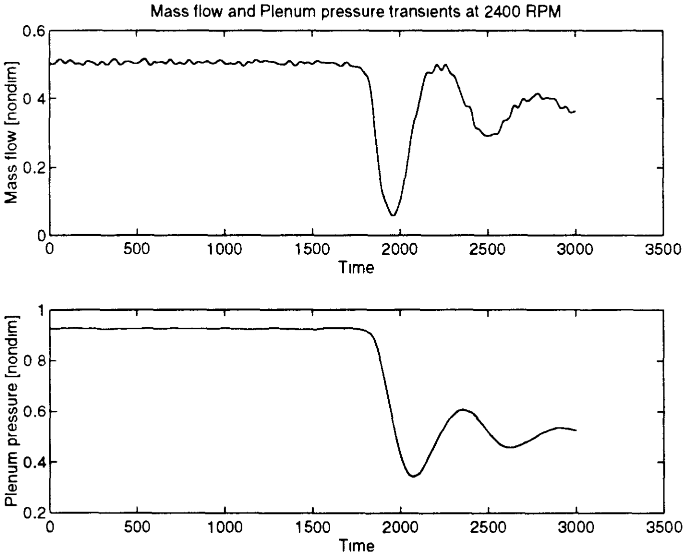

Figure 5-4: Open-loop system transients with time

Transients in a $\Phi - \Psi$ plane of the unstable behavior of the system show again the strong coupling between surge and rotating stall dynamics, even if the system never goes into surge (see Figure 5-5).

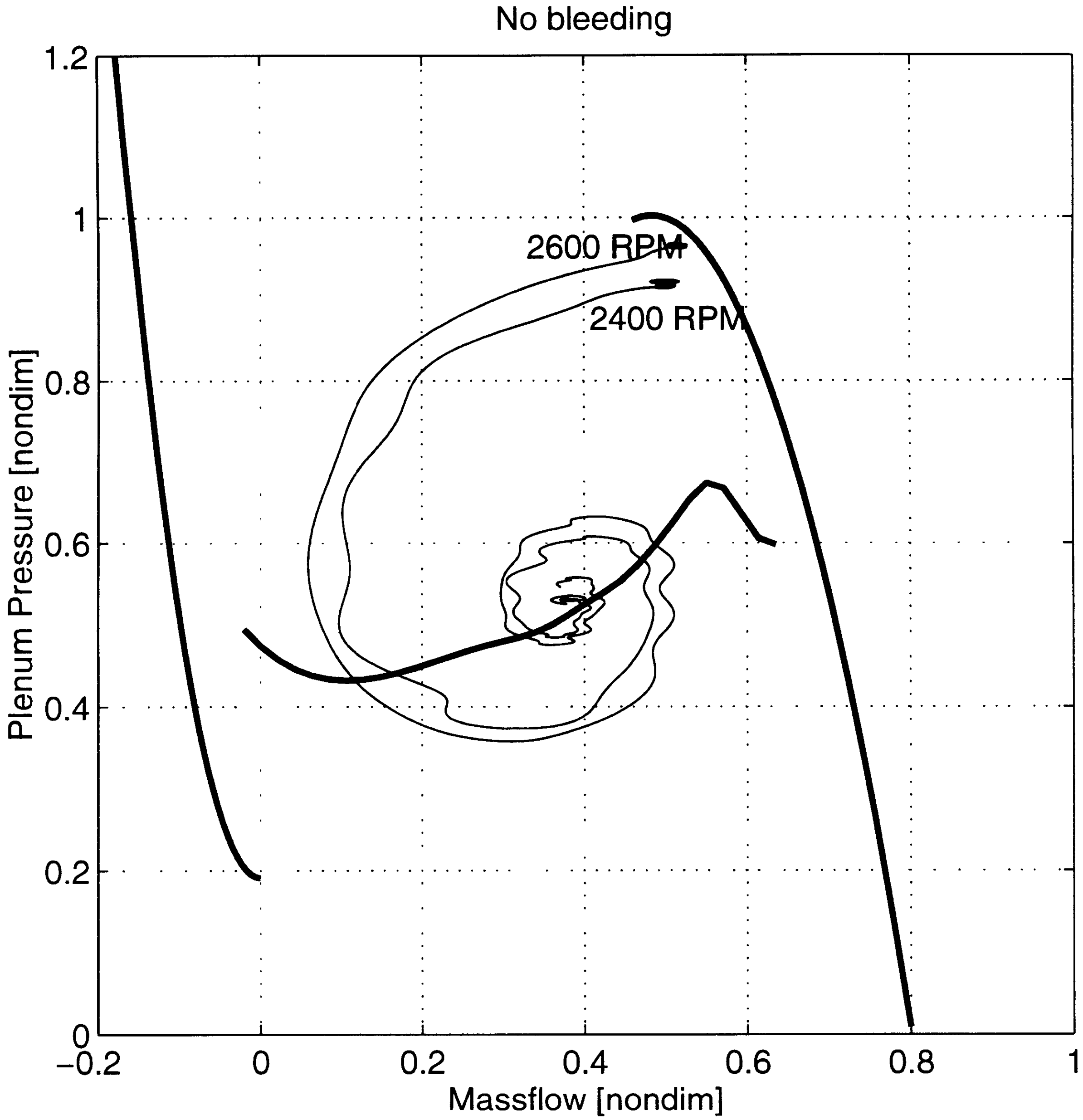

Figure 5-5: Open-loop system transients in a $\Phi - \Psi$ plane

The absence of deep surge was not surprising. Protz [26] was able to barely reach surge transients at a speed of 2600 RPM. In our case, the speed required to surge should be even higher since the addition of the downstream duct decreases the B parameter from 0.94 to 0.85 at 2400 RPM. However, what was important for this first investigation of asymmetric bleed actuation was to have a compression system with strong rotating stall-surge coupling.

Hot-wires traces and averaged pre-stall behavior

Analysis of the pre-stall behavior is very important for control. Figure 5-6 shows typical hot-wire traces for an initial transition into stall-surge. These measurements were done with valve opening of 12 degrees since it is the mean valve position at which the control scheme (see Section 5.3) was tested.

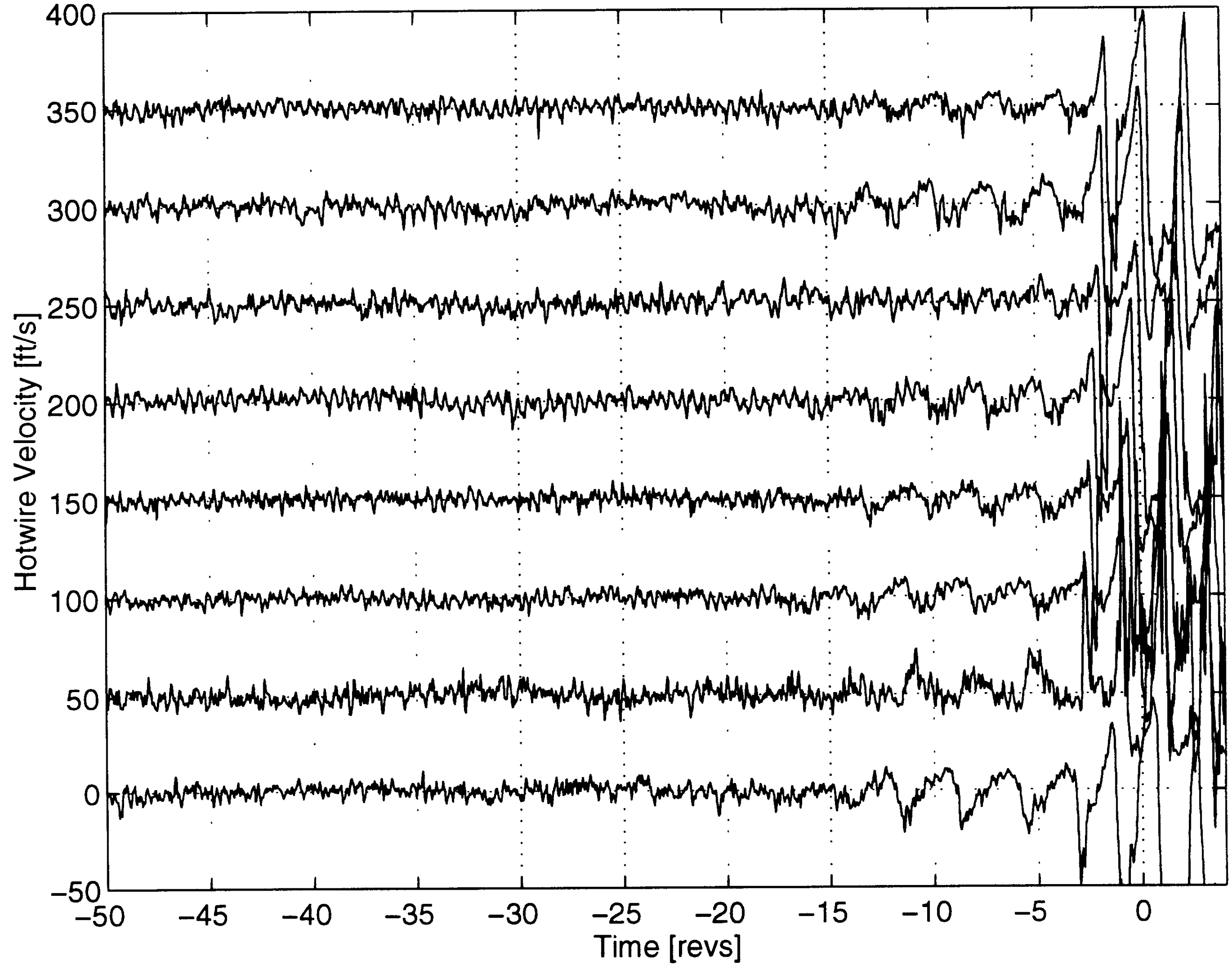

Figure 5-6: Hot-wire traces for open-loop compressor.

The stall cell precursor is visible in the hot-wire traces 20 rotor revolutions prior to surge-stall.

One can also analyze the pre-stall behavior using a spectral approach. The power spectral density captures its frequency content. By looking at the PSD of compressor sensors prior to surge, one can deduce which linear modes are loosing stability. The modes come from the computed Spatial Fourier Coefficients (SFC, see [22]) based on the array of eight hot-wires reading. The PSD presented here comes from averaging 16 seconds of data taken at a throttle setting just prior to the stability limit. They were calculated using Welch's method with a 2048 point Hanning window and a sampling frequency of 1 kHz.

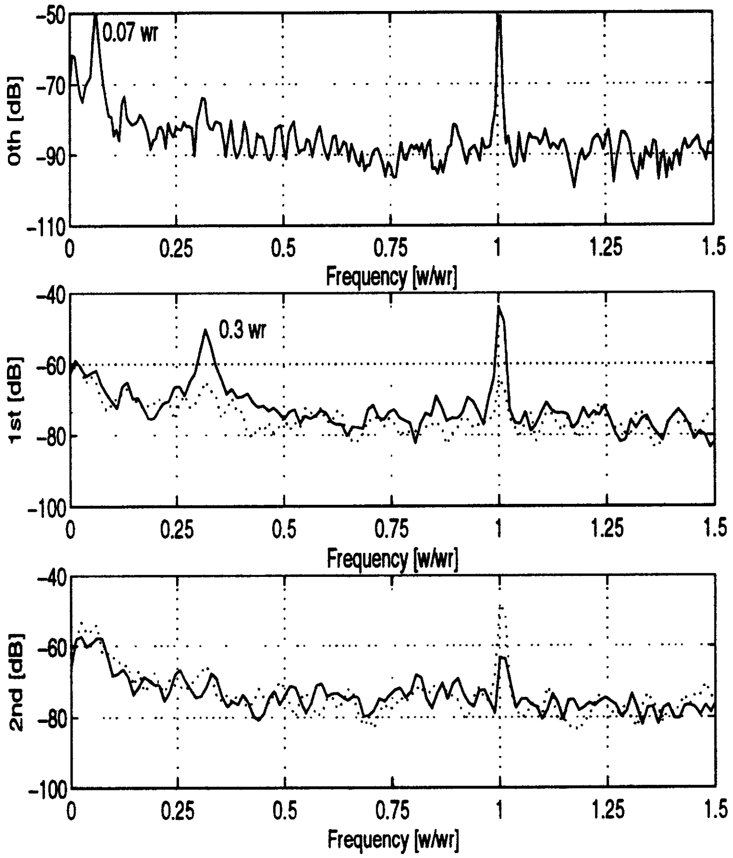

Figure 5-7: PSD of open-loop compressor prior to the stability limit. Solid and dashed lines represent forward and backward traveling waves respectively.

From Figure 5-7, one can see that the first harmonic has a peak at approximately $0.3\omega_r$ corresponding to the Moore-Greitzer Stall mode. The zeroth harmonic has a peak at approximately $0.07\omega_r$. Furthermore, in Figure 5-7, the second harmonic appears to well damped, which suggests that the zeroth and first harmonics are the critical modes. The next section will however give a better insight regarding this issue.

Time Spectral Analysis of Pre-Stall Behavior

An easy way to identify the most unstable mode of the compressor, or more generally of the compression system, is to look at the time variation of the power spectral densities. This method uses the same approach as explained in the previous section but it gives the evolution with time along with the stall ramp event.

It thus allows the analysis with time and frequency for each harmonic. The following figures (Figures 5-8, 5-9 and 5-10) show the power spectral densities (PSD) during a stall ramp for the zeroth, first and second mode.

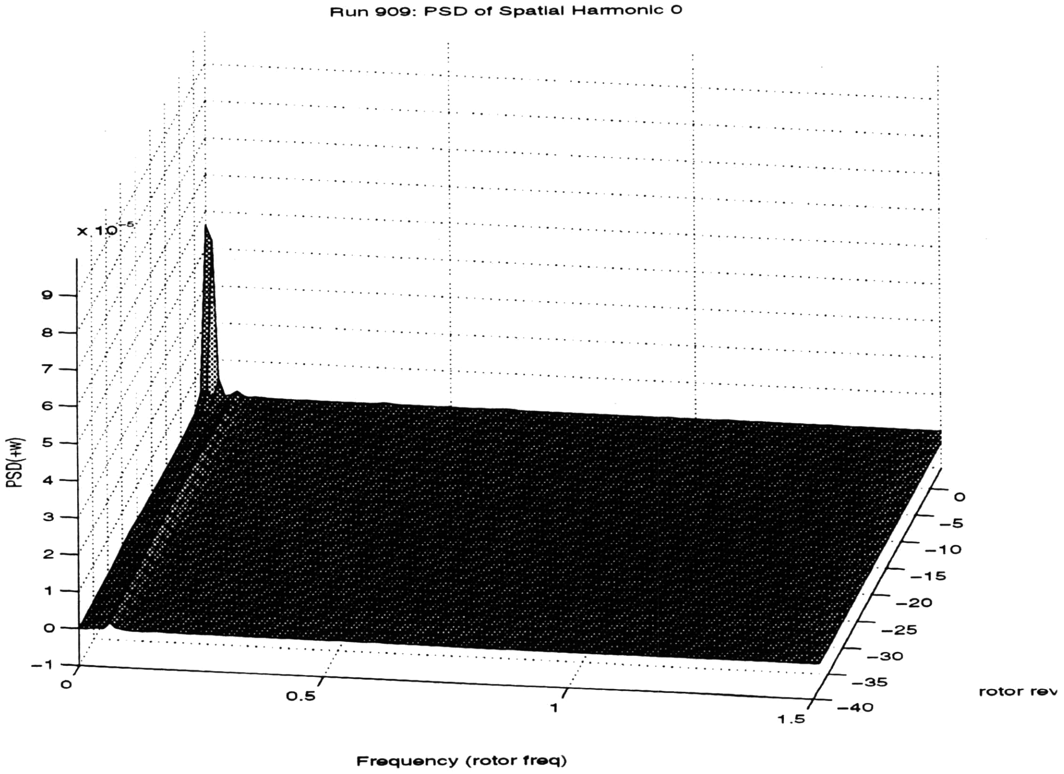

Figure 5-8: Surge mode PSD

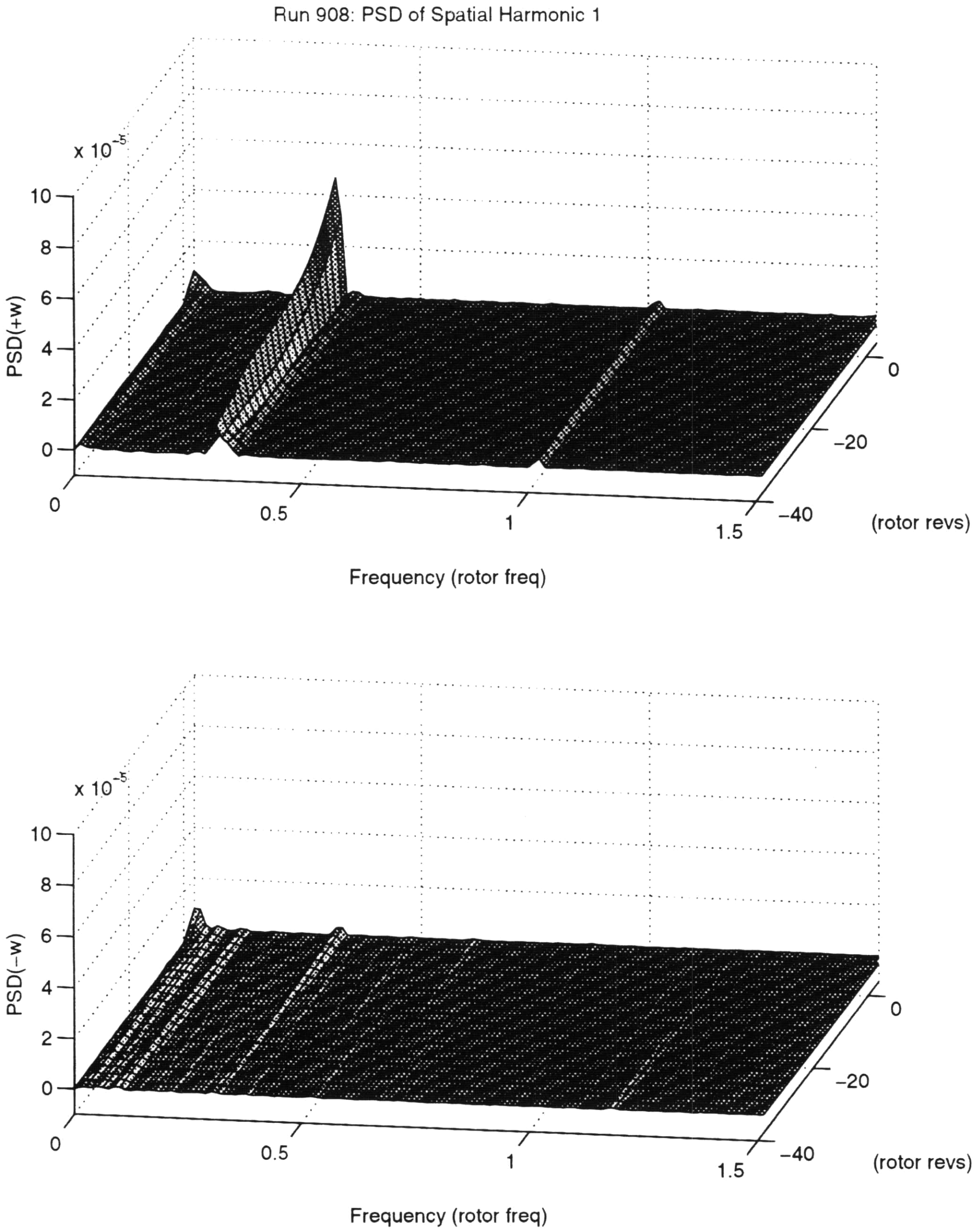

Figure 5-9: First mode PSD

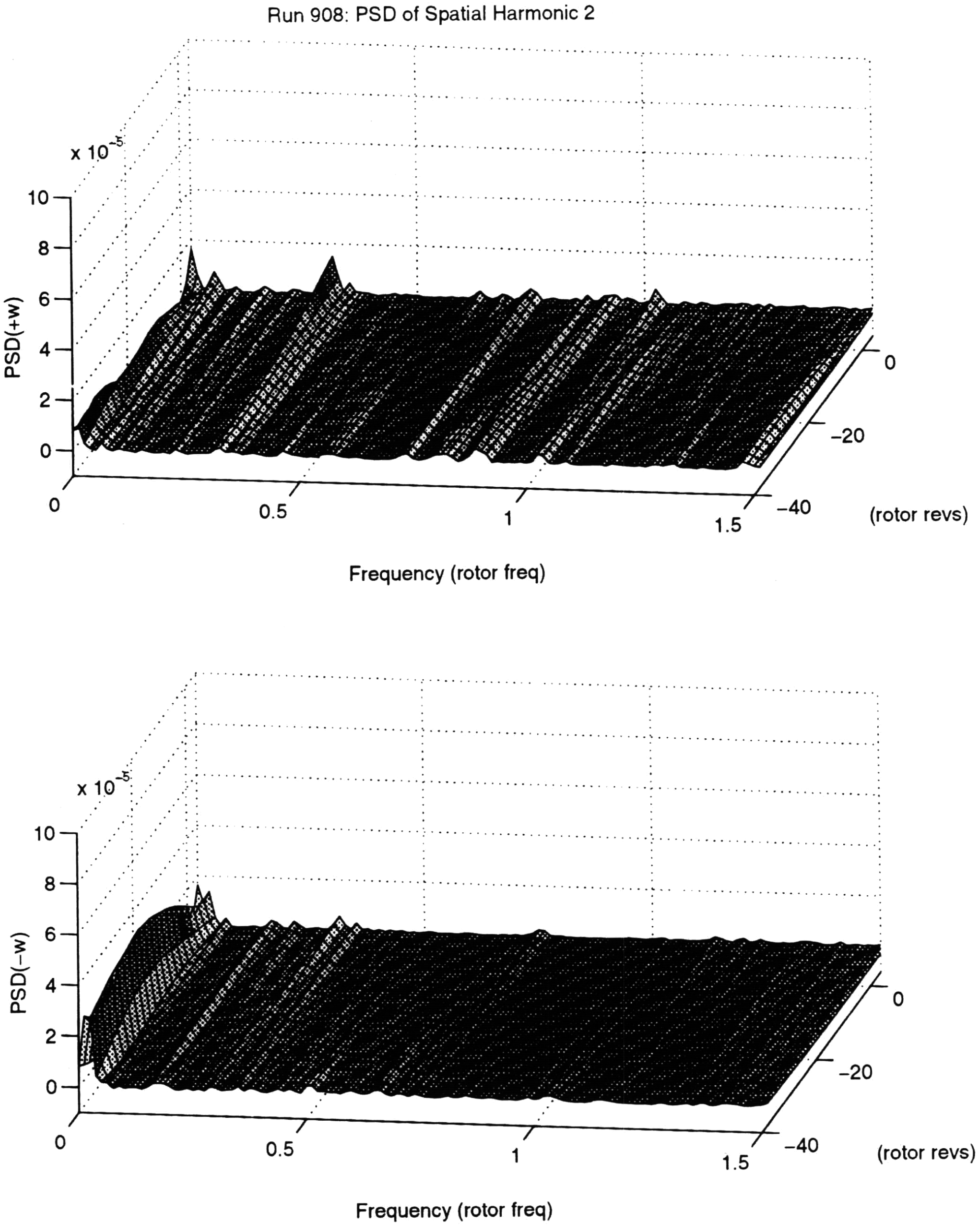

Run 908: PSD of Spatial Harmonic 2

Figure 5-10: Second mode PSD

From these figures, one can see that the first mode is the one to control first to have a stall stabilization effect. This dictated the first choice of control scheme to test.

Indeed, these figures show that the first harmonic clearly dominates in magnitude and rotates steadily at about 0.3 times rotor revolution $(0.3\omega_r)$.

5.2 Forced Response of the actuated compression system

This section presents the results of the forced response tests. The purpose of this set of tests is to measure the response of the actuated system and investigate the 2D effect of the actuation system. A comparison with the model presented in Chapter 4 is also given.

Tests of the surge and first rotating stall harmonic was done and compared with the modeled forced responses (see Chapter 4).

5.2.1 Identification Methodology

The system identification runs were performed with an input temporal frequency sweep on the amplitude of a stationary spatial cosine bleeding wave for one harmonic at a time. The temporal variation of the SFC, in the form of the coefficient of the spatial cosine and sine wave, of the corresponding harmonics are computed from the hot-wire measurements.

The output of the system should contain both positive and negative frequencies which represents clockwise and counter-clockwise rotational disturbances. In the identification method used, a transfer function for the positive frequencies part was obtained by the following treatment:

$$G(\omega) = G_{cos \rightarrow cos}(\omega) + iG_{cos \rightarrow sin}(\omega)$$

with,

- ω: temporal frequency of sweep
- $G_{cos \rightarrow cos}(\omega)$: measured transfer function from the amplitude of the cosine ve-

locity disturbance input to the amplitude of the cosine velocity disturbance measured by the hot-wires

- $G_{cos \rightarrow sin}(\omega)$: measured transfer function from the amplitude of the cosine velocity disturbance input to the amplitude of the sine velocity disturbance measured by the hot-wires

The main problem was to get a good coherence between the input and output signals. For that reason, the frequency sweep was cut into many frequency ranges sweeps in order for the system to stay at a given frequency longer and so, to have a better average behavior.

The surge transfer function was taken with two sweeps; the first from .1 to 15 Hz and the second one from 1 to 40 Hz. The first mode transfer function was taken with 7 sweeps regularly distributed between 1 to 65 Hz.

The open-loop transfer functions presented here were taken at nominal bleed valve opening of 12 degrees. The transfer functions were taken from the measured valve position to the measured hot-wire velocity. They do not include the dynamics associated with the valves and can be directly compared to the transfer functions from the model described in Chapter 4. The amplitude command to the valve corresponded to a valve angle movement of +/- 12 degrees.

5.2.2 Zeroth mode – surge mode

The surge mode is excited by opening and closing all the valves simultaneously. If we take a snapshot at a certain time and plot the opening of the valves, we get the plot presented in Figure 5-11. In dashed line is plotted the idealistic bleed opening if we had a continuous actuation along the whole circumference.

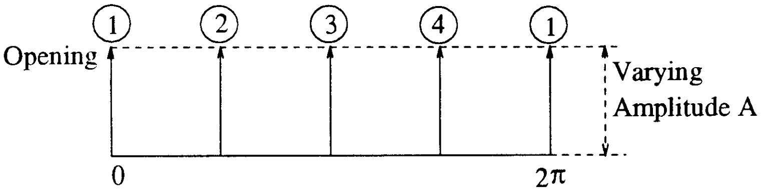

Figure 5-11: Opening of the valves (zeroth mode)

Figure 5-12 shows measured and model surge transfer functions at a throttle setting near the open-loop stall point of the compressor.

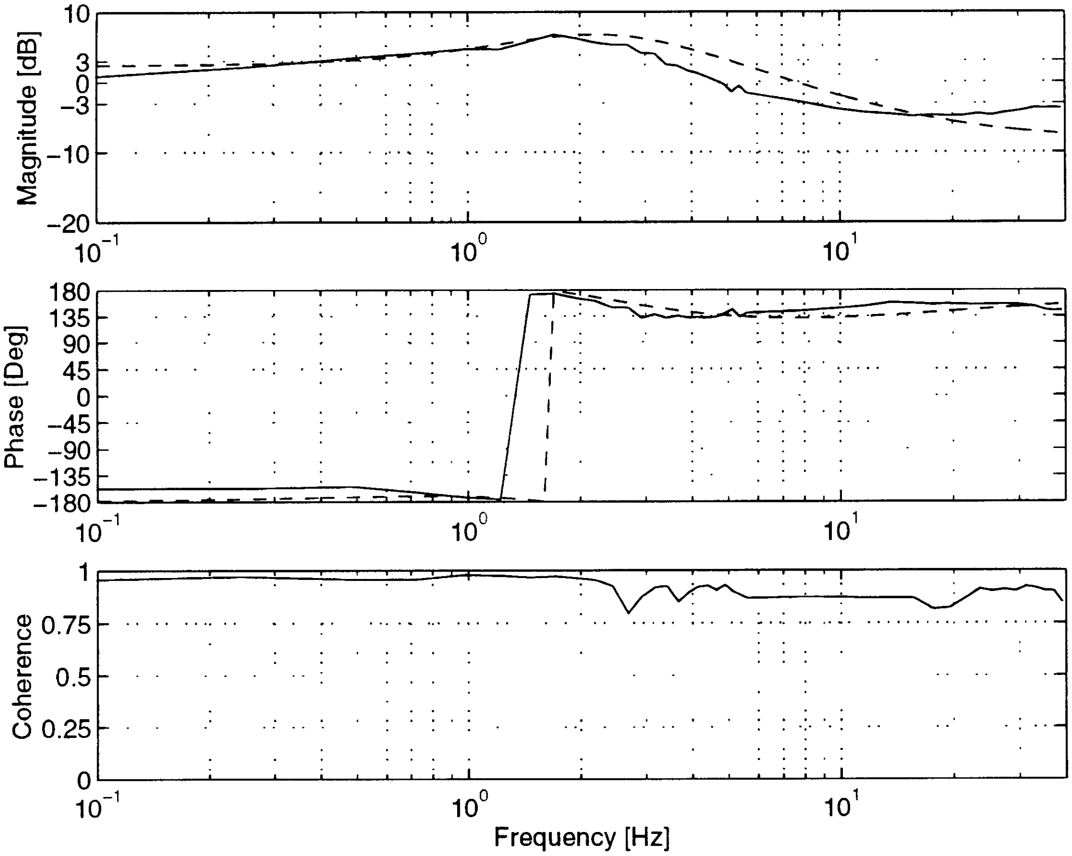

Figure 5-12: Surge mode forced response. Solid and dashed lines represent experimental and model transfer functions respectively.

The model transfer functions were computed using the same characteristic point on the compressor curve and the parameters in Table 4.3.

From that frequency response, we see that the surge frequency is around 2Hz., very close to the model prediction (see Chapter 4) and it also confirms that compressor exit bleed valves have a quantitative effect on the surge dynamics.

The fitted model gives a very good fit with the experimental results; which is important because it validates the dynamics of the 1D bleed model. Another proof of the good fitting of the experimentally measured surge dynamics with the 1D bleed model, comes from the comparison in a pole-zero map. The experimental data was fitted using a transfer function with three poles and two zeros similarly to the model. The fit to the transfer function minimizes the squared error with uniform weighting over all frequencies. Figure 5-13 shows the pole-zero map corresponding to the fitted transfer function with comparison to the model (see Chapter 4).

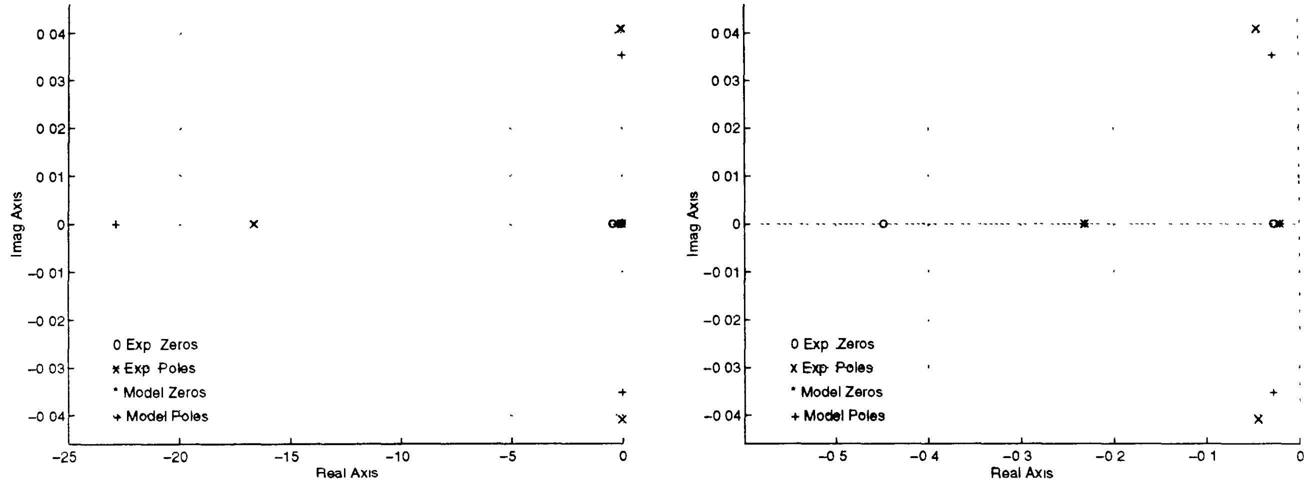

(a) Pole-Zero Map: experimentally and model

(b) Pole-Zero Map zoomed near the origin: experimentally and model

Figure 5-13: Pole-Zero Map Comparison: Surge dynamics

5.2.3 First mode

The most interesting result comes from this forced response. Indeed, one of the goals of this research is to investigate the two-dimensional stabilizing effect of the actuation.

Once again,if we take a snapshot at a certain time and plot the opening of the valves, we get Figure 5-14 and in dashed line is plotted the idealistic bleed opening if we had a continuous actuation along the whole circumference.

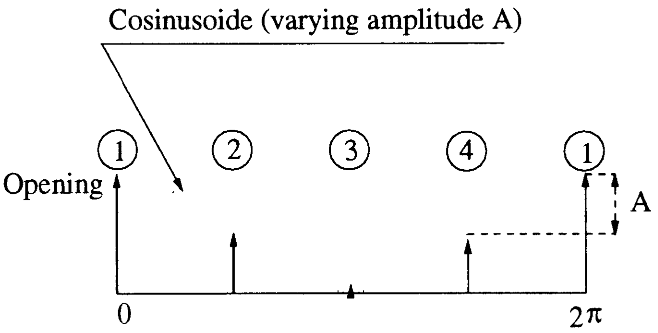

Figure 5-14: Opening of the valves (first mode)

Figure 5-15 shows measured and model first mode transfer functions at a throttle setting near the open-loop stall point of the compressor.

The first observation to make on the first mode transfer function, is that the first mode is indeed excited by the actuation system. The quantitative effect on the first mode shows that asymmetric bleed actuation is therefore a valid way of investigation for rotating stall control.

The response shows a strong peak corresponding to the dominant pole at a frequency of about one third of the rotor frequency and which is the first mode stall frequency for this compressor. That corresponds to the $\omega = .3\omega_r$ that the PSD plots present.

The model transfer functions came from the transfer function derived in Chapter 4 with some values of the parameters coming from Haynes [11], the others (K_r, K_s, τ_s, τ_r, τ_b – see Table 4.5) varied to get the best fit possible while keeping their values physically reasonable. The tuned model gives a good fit with the experimental results, which is important because it validates the dynamics of the general 2D bleed model.

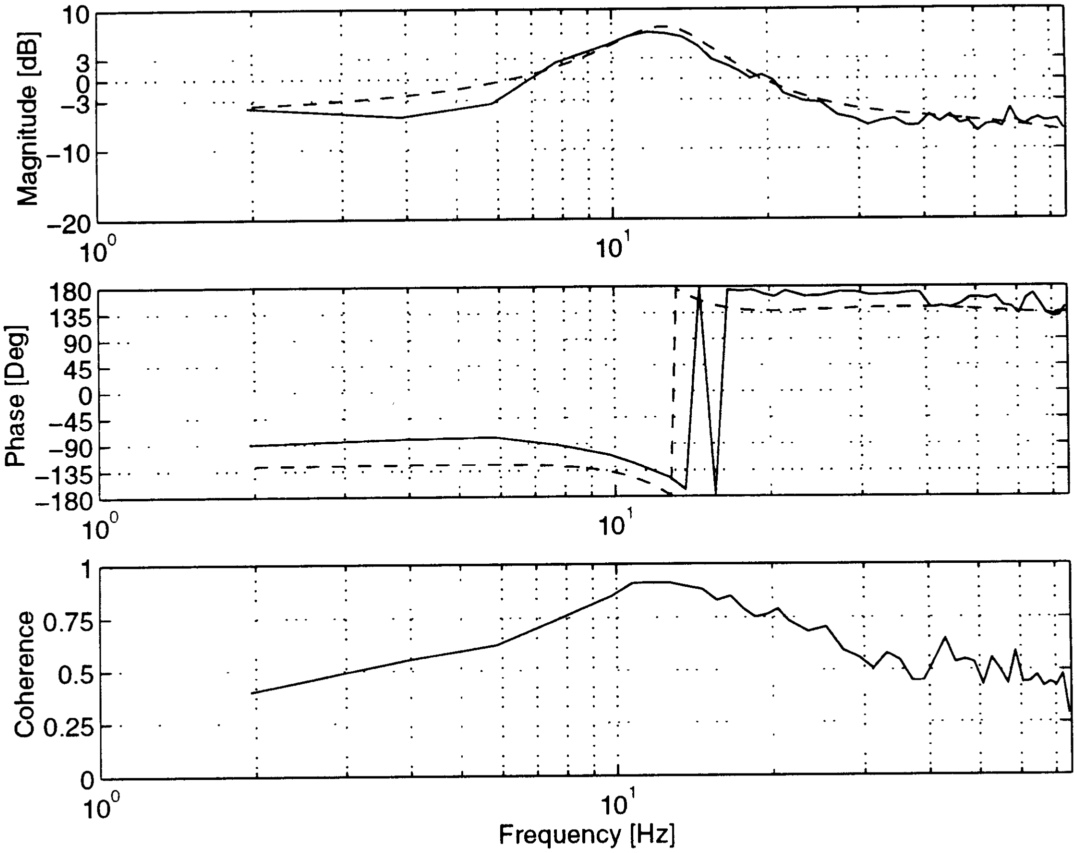

Figure 5-15: First mode forced response. Solid and dashed lines represent experimental and model responses (after parameters are tuned to values in Table 4.5 respectively.

5.3 Closed-loop behavior of the actuated compression system

The previous section presented measurements of the actuated system dynamics, when the compressor is allowed to operate without feedback, i.e. the open loop dynamics. This section discusses the results for the closed-loop compression system with actuation; that is, when the perturbations are being fed back to the actuators for stabilization. If the perturbations being fed back into the compressor counteract the flow phenomena that cause the compressor flow field to become unstable, stable closed-loop operation can be maintained at operating points that would otherwise be unstable.

Open-loop transient measurements suggested that the first mode was going unstable first. Since the flow is undistorted for this research, all the modes evolve independently (see [27]). Based on these observations, a first harmonic proportional control system was tried. This system was indeed the simplest method of obtaining first mode stabilization. If we use the notation from Chapter 4, one can write the complex-coefficient proportional control law in the following manner (see [11]):

$$\tilde{\gamma}_1 = K e^{\imath \phi} \tilde{\phi}_1 \tag{5.1}$$

The procedure used to optimize the parameters K and ϕ is the one used by Paduano ([22]):

- Pick a reasonable initial value for K to have a certain effect on the Power Spectral Density of the first harmonic (PSD1).

- Optimize the phase ϕ to decrease the resonant peak of PSD1.

- Increase the gain to have the best stabilizing effect.

Executing this procedure at the exact same value of the throttle position as in Figure 5-7 with K=80 and $\phi = -180 deg$. The resonant peak for the first harmonic was thus decreased by about 10 dB, as shown in Figure 5-16, which should be compared to Figure 5-7. Notice that the control software nondimensionalizes the velocity by the rotor speed and that it treats the motor command in counts.

The control parameters were then fixed to the values (K=80, $\phi = -180$) and 3% range extension was achieved which is shown graphically in Figure 5-17.

To be complete, Figure 5-18 depicts the PSD of closed-loop compressor immediately prior to the closed loop stability limit.

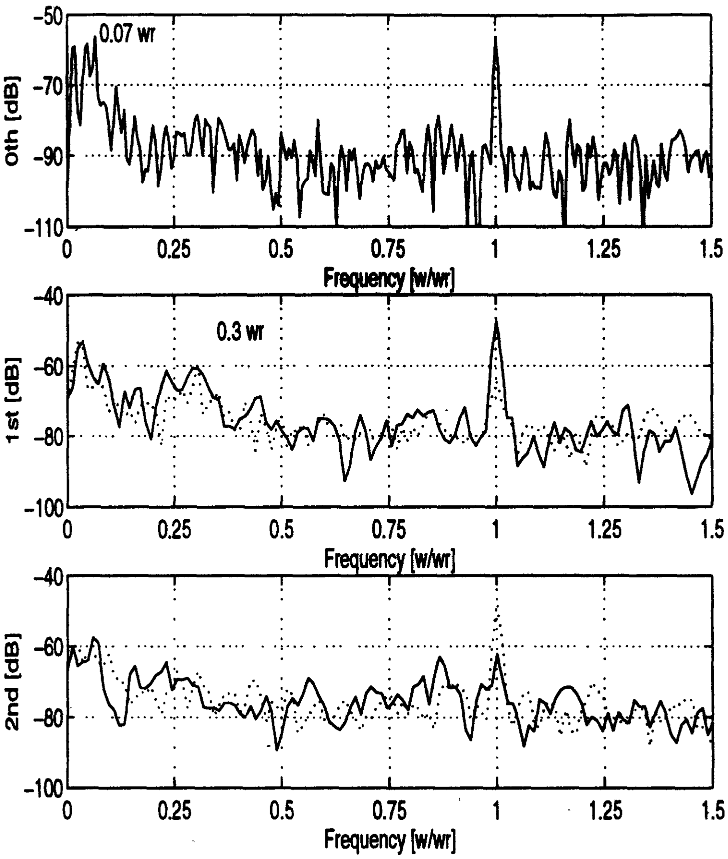

Figure 5-16: PSD of closed-loop compressor prior to the open-loop stability limit. Solid and dashed lines represent forward and backward traveling waves respectively.

From Figure 5-18, we see that the second mode is still more damped than the two others. But we also see that the relative importance between zeroth and first mode has changed. This increase in importance of the zeroth mode compared to the first suggests that 1D control (for instance a Liaw-Abed controller) should be added to the previous control system to further improve stability performance of the GTL-LS3 with bleed actuation.

It should be noted that performance improvement might be possible using the same first harmonic proportional controller and spending more time in optimizing the parameters. In particular, increasing the gain may yield additional range extension, but was not attempted because of possible stress on the valves and overheating of the servos.

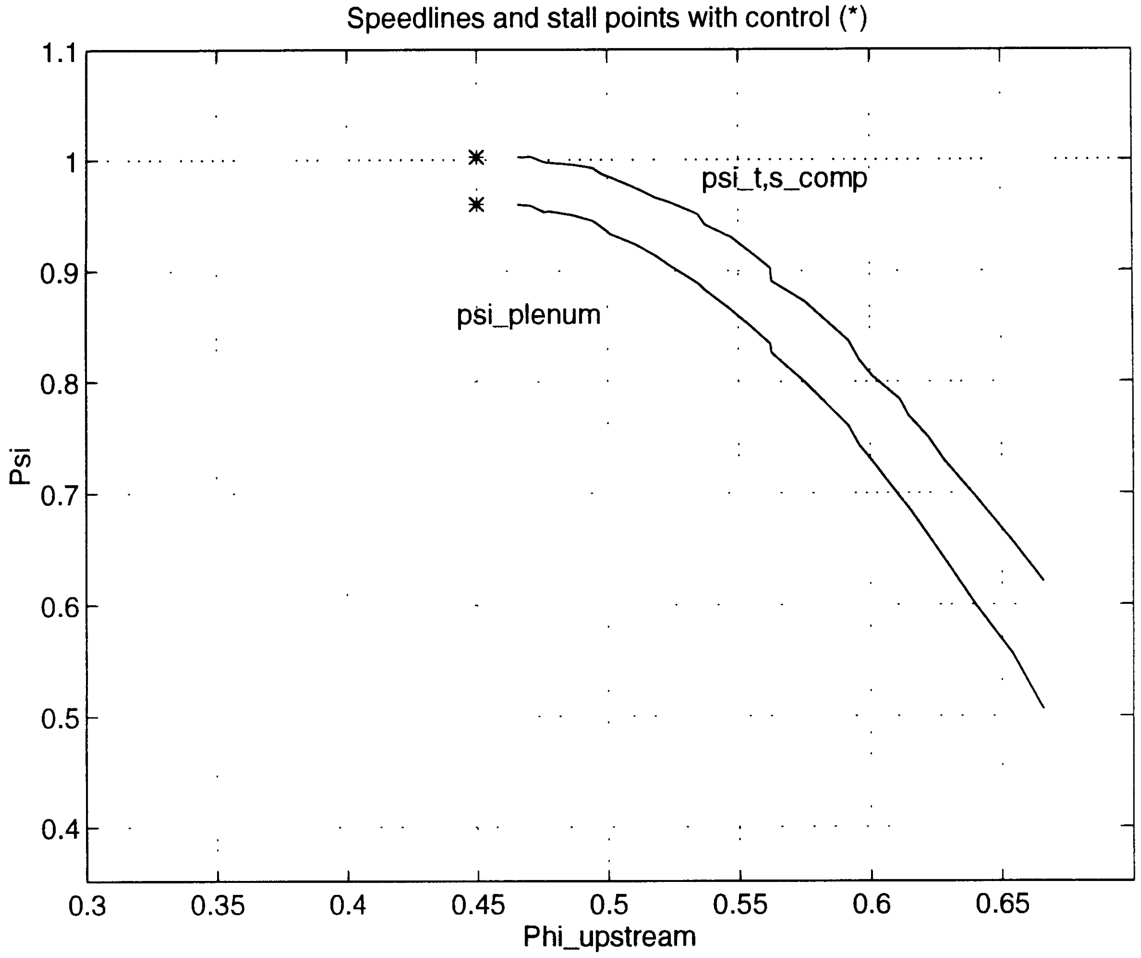

Figure 5-17: Speedlines and closed-loop stall points (*).

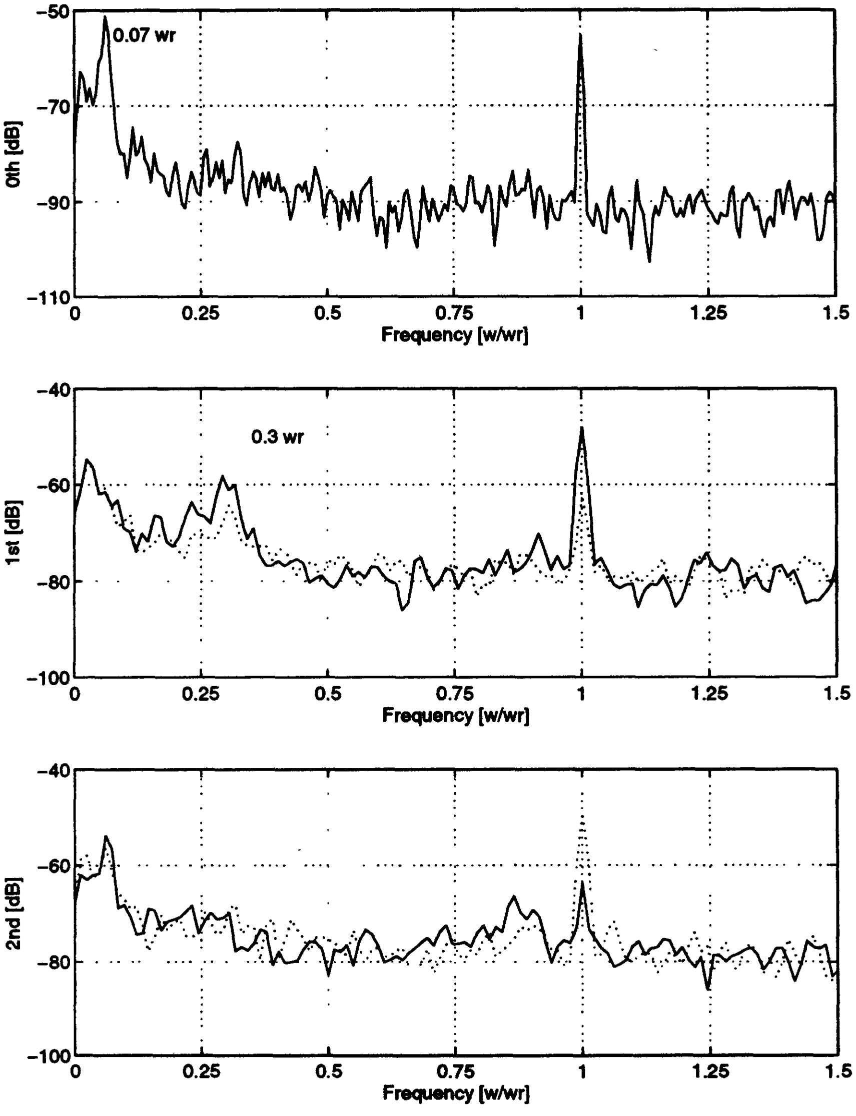

Figure 5-18: PSD of closed-loop compressor prior to the closed-loop stability limit. Solid and dashed lines represent forward and backward traveling waves respectively.

CHAPTER 6

SUMMARY AND CONCLUSIONS

Experimental study and investigation of the two-dimensional effect of asymmetric bleed actuation was performed to evaluate active control concepts in a high-B multi-stage compressor.

Design of the actuation using Greitzer's one-dimensional model was carried out prior to the actual building of the actuation. Use of a downstream duct for improvement of the control power was used and theoretically evaluated. The actuation consisted of a set (here 4) of high-speed bleed valves at the compressor exit. Characterization of the actuation (bandwidth, rate limit and calibration measurements) was done and led to a successful implementation on the GTL-LS3 compression system.

A general two dimensional model of the actuated system based on the Moore-Greitzer compressor model was derived. Sensor location analysis for surge and first harmonic control was done based on that model.

The open-loop behavior of the high-B compression system with and without actuation was measured to verify the impact of actuation and ducting modifications. Transfer function measurements were used to validate the surge portion of the compression system model. First harmonic transfer functions demonstrated the two-dimensional effect of the bleed actuation and were used to validate the dynamics of the rotating stall part of the model.

A proportional controller was then tested and demonstrated the two-dimensional effect of the actuation as suggested by the transfer functions measurements. 3 % range extension was achieved with that very simple controller.

6.1 Future research

The results presented in this thesis are very promising: the model seems to be a very good predictive tool and two-dimensional stabilizing effect of the asymmetric bleed actuation was demonstrated. However, some issues were raised during this research project and should be addressed in future experiments.

The first problem is due to limit cycle behavior of the actuator. For high frequency and high amplitude, the servo-valve presented very poor performance. That forced the valve opening to half of its possibility. Hence, significant benefit may be possible with better actuator behavior. The possibilities for improving the actuators are diverse: an inner loop around the actuator could be used; another type of valve with 8 holes instead of 4 could be used to decrease the 45 degrees needed for full opening; better behaved amplifiers or stronger motors could be used in order to increase the input current and hence the torque; more valves than four could be used and also decrease the opening of one valve.

Active control with first harmonic proportional control was successful in improving the stability performance. However, it is thought that the gain and phase of this controller could be better optimized. PSD plots of the closed-loop compression system just before stall showed an increase of relative zeroth mode resonant peak compared to the first mode. That suggests that 1D control, in conjunction with first harmonic control would be successful in further improving the stable operating range. Single-sided actuation (in opposition to two-sided as used in this research) could also be a very interesting approach since it could allow a reducing of the total mass flow that must be bled in order to control rotating stall.

This type of actuation seems very promising and its easy implementation on a full-scale engine should make it an important approach to pursue in this rig and future experiments.

APPENDIX A

BLEED VALVES, ACTUATION RING AND DOWNSTREAM DUCT DRAWINGS

In this appendix, the drawings of the valve, the valve casing, the actuation ring and the downstream duct are presented.

Figure A-1 is the assembly drawing, with a description of all the different components of the actuation, from A-2 to A-14, with:

- A-2: drawing of the valve.
- A-3: drawing of part I of the valve casing.
- A-4: drawing of part II of the valve casing.
- A-5: drawing of part III of the valve casing.
- A-6: drawing of the actuation ring overall view.

- A-7: drawing of the actuation ring detail 1.

- A-8: drawing of the actuation ring detail 2.

- A-9: drawing of the actuation ring side view.

- A-10: drawing of the actuation ring section G-G.

- A-11: drawing of the downtream outer duct.

- A-12: drawing of the dowsntream outer duct detail.

- A-13: drawing of the downstream inner duct.

- A-14: drawing of the downstream inner duct detail.

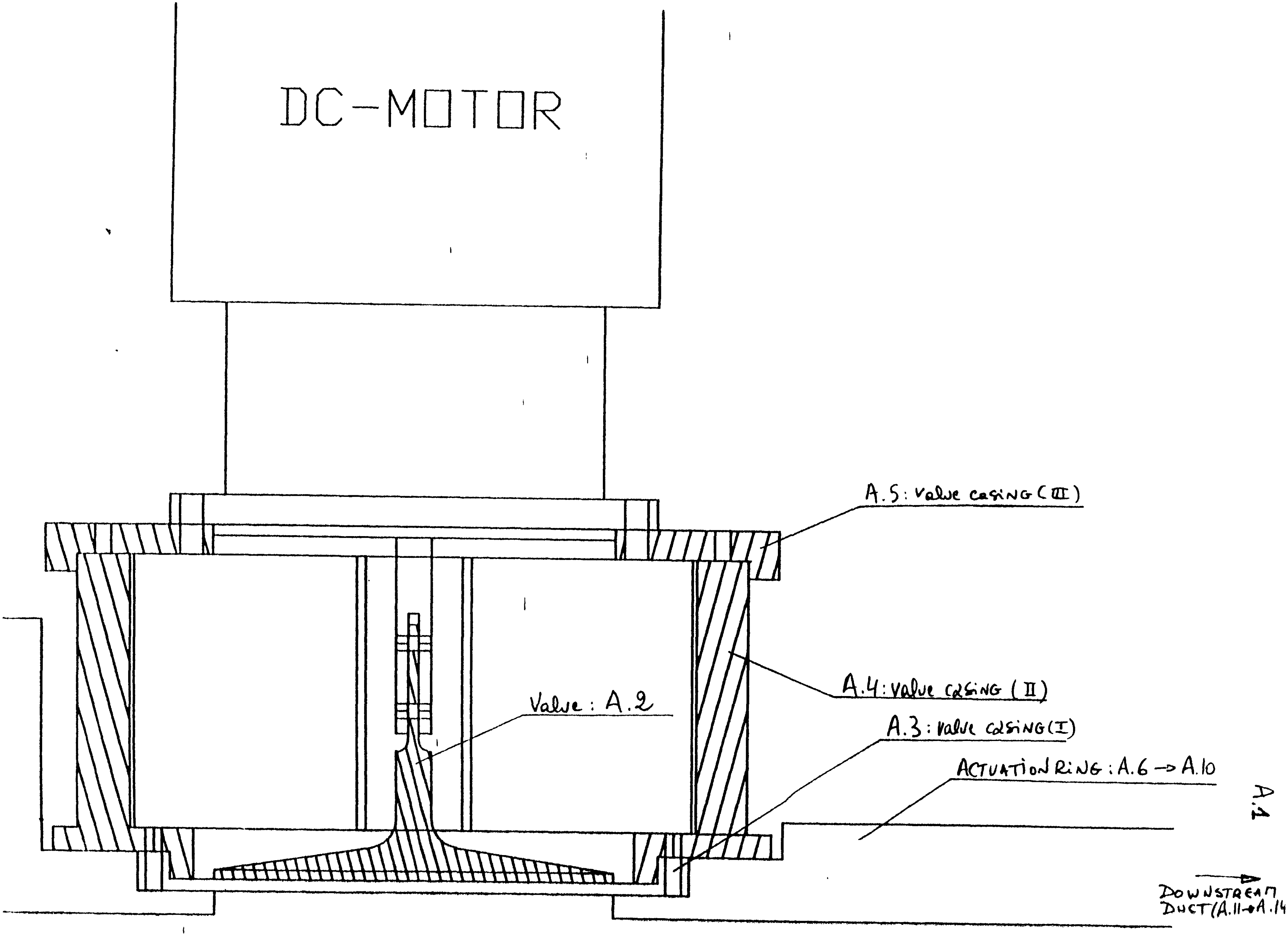
DC-MOTOR
A.5: valve casing (III)
A.4: valve casing (II)
Valve: A.2
A.3: valve casing (I)
ACTUATION RING: A.6 -> A.10
DOWNSTREAM DUCT (A.11 -> A.14

A.1

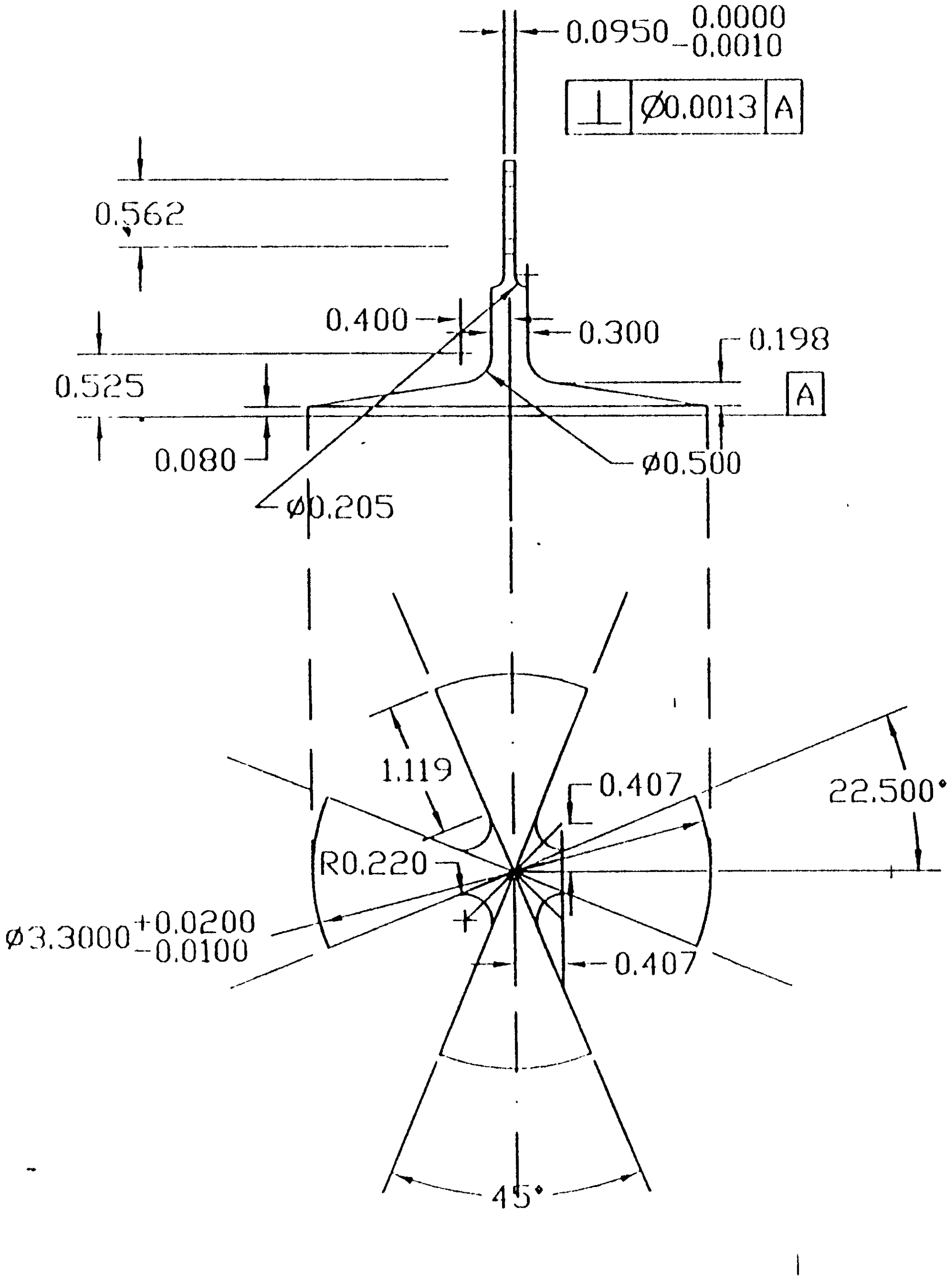
0.0950 $^{0.0000}_{-0.0010}$
⊥ Ø0.0013 A
0.562
0.400
0.300
0.198
A
0.525
0.080
Ø0.205
Ø0.500
1.119
0.407
22.500°
R0.220
Ø3.3000 $^{+0.0200}_{-0.0100}$
0.407
45°

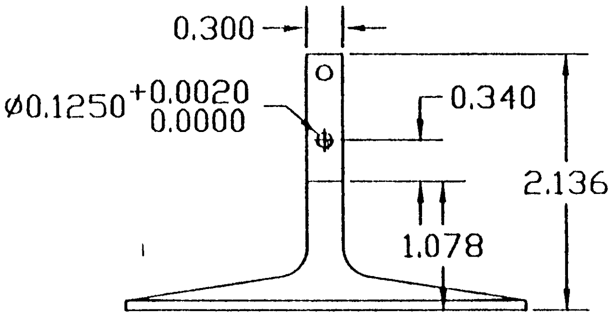
0.300
Ø0.1250 $^{+0.0020}_{0.0000}$
0.340
2.136
1.078

M.I.T. GAS TURBINE LAB

VALVE

TOLERANCES
(unless otherwise specified)

.X	+-	0.015
.XX	+-	0.010
.XXX	+-	0.005

DRAWN BY: A. FAHIM

DATE:

MATERIAL: ALUMINUM

DATE:

SCALE:

DRAWING NO: A.2

A.3

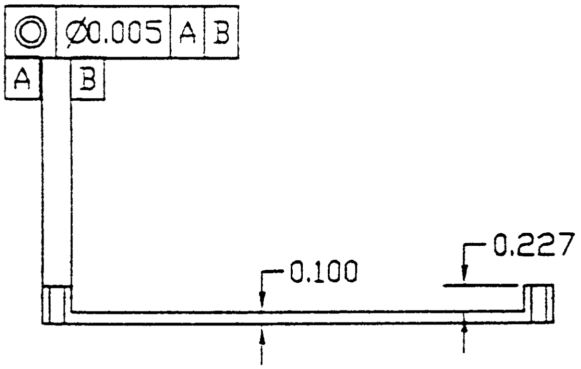
◎ Ø0.005 A B
A
B
0.100
0.227

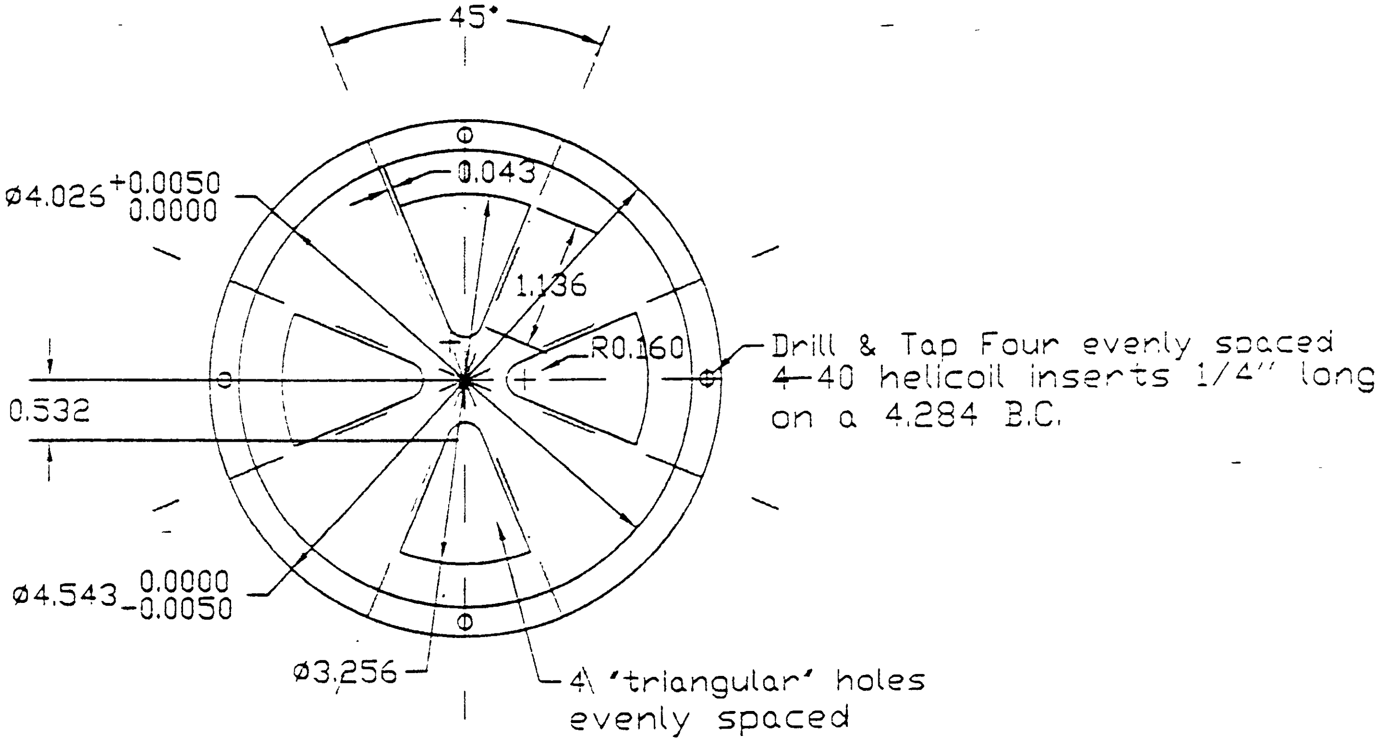
45°
Ø4.026 +0.0050 0.0000
0.043
1.136
R0.160
Drill & Tap Four evenly spaced 4-40 helicoil inserts 1/4" long on a 4.284 B.C.
0.532
Ø4.543 0.0000 -0.0050
Ø3.256
4 'triangular' holes evenly spaced

M.I.T. GAS TURBINE LAB		
VALVE CASING (part I)		
TOLERANCES (unless otherwise specified) X +- 0.015 .XX +- 0.010 .XXX +- 0.005	DRAWN BY: A. FAHIM	DATE:
	MATERIAL: ALUMINUM	DATE:
	SCALE:	DRAWING NO: A.3

M.I.T. GAS TURBINE LAB

VALVE CASING (part II)

TOLERANCES (unless otherwise specified) .X +- 0.015 .XX +- 0.010 .XXX +- 0.005	DRAWN BY: A. FAHIM	DATE:
	MATERIAL: ALUMINUM	DATE:
	SCALE:	DRAWING NO. A.4

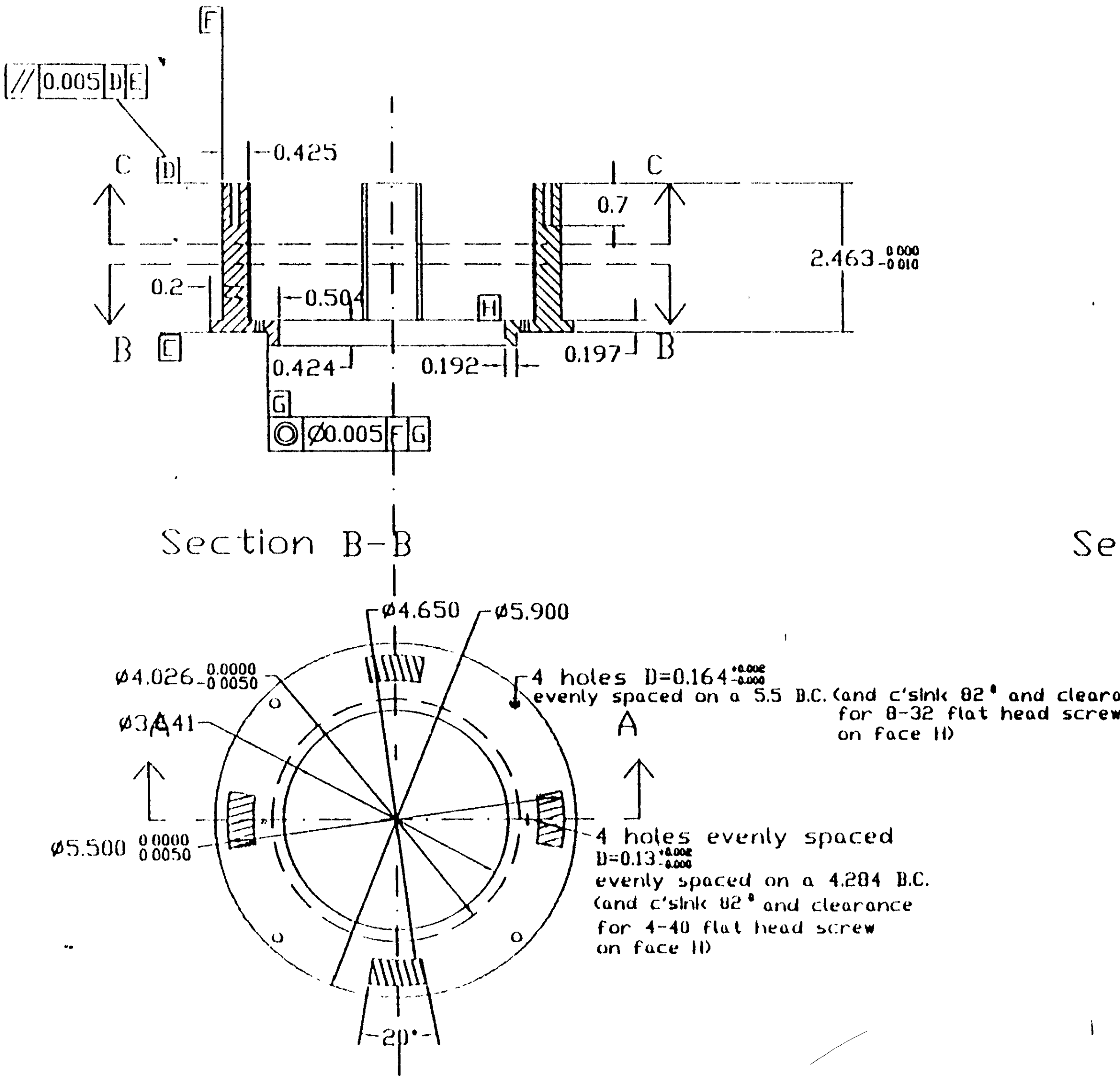

F
// 0.005 D E
C
D
0.425
C
0.7
2.463 +0.000 -0.010
0.2
0.504
H
B
E
0.424
0.192
0.197
B
G
◎ Ø0.005 F G
Ø4.650
Ø5.900
Ø4.026 +0.0000 -0.0050
Ø3.441
A
A
Ø5.500 +0.0000 -0.0050
20°

Section B-B

4 holes D=0.164 +0.002 -0.000 evenly spaced on a 5.5 B.C. (and c'sink 82° and clearance for 8-32 flat head screw on face H)

4 holes evenly spaced D=0.13 +0.002 -0.000 evenly spaced on a 4.284 B.C. (and c'sink 82° and clearance for 4-40 flat head screw on face H)

Section C-C

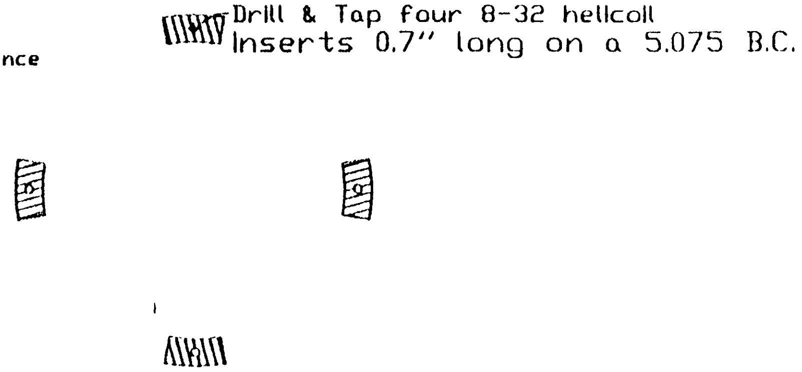

Drill & Tap four 8-32 helicoil Inserts 0.7" long on a 5.075 B.C.

A.4

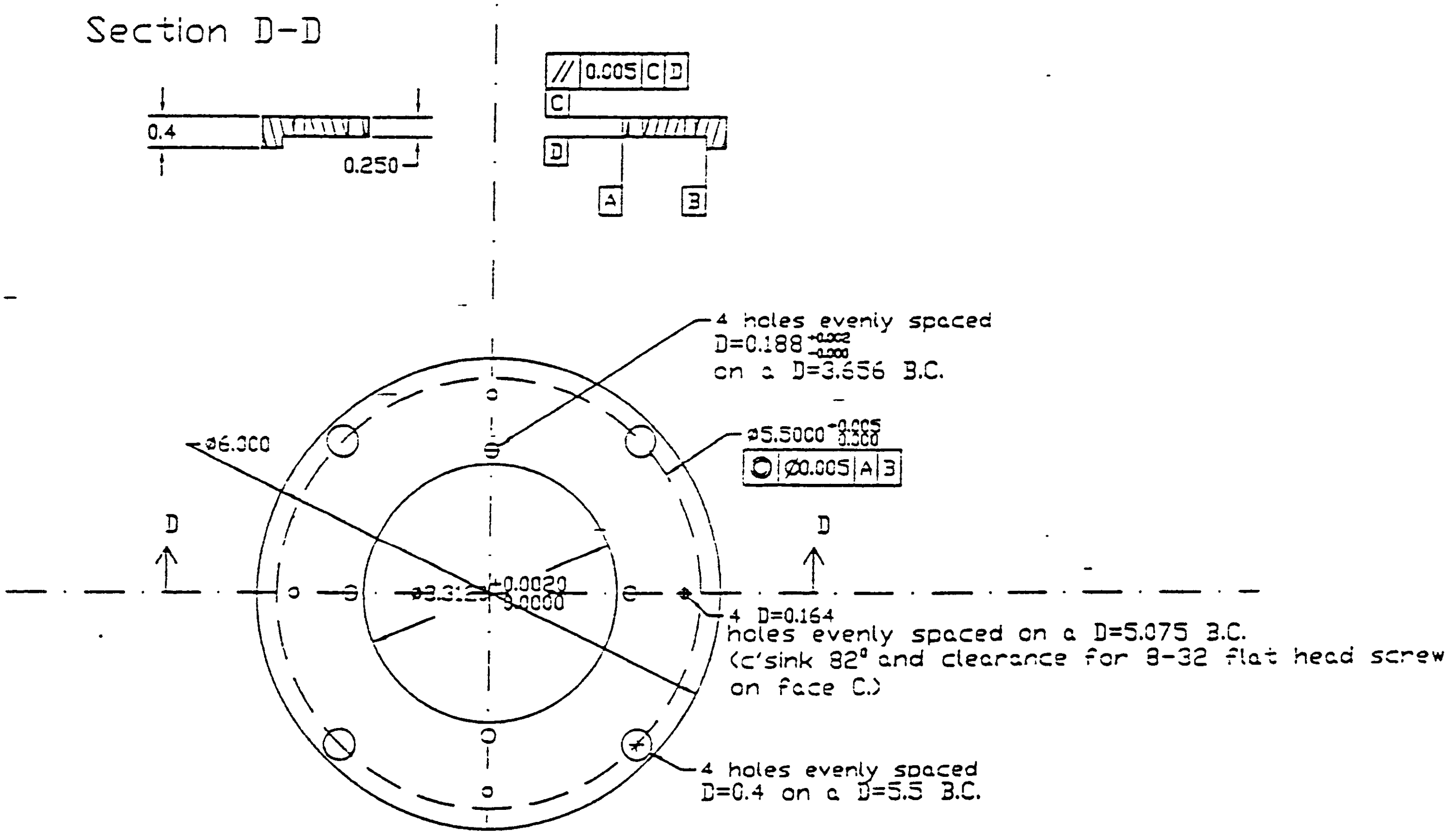
Section D-D
0.4
0.250
// 0.005 C D
C
D
A
B
4 holes evenly spaced
D=0.188 +0.002 −0.000
on a D=3.656 B.C.
⌀6.000
⌀5.5000 +0.005 0.000
◎ ⌀0.005 A B
D
D
⌀3.3125 +0.0020 0.0000
4 D=0.164
holes evenly spaced on a D=5.075 B.C.
(c'sink 82° and clearance for 8-32 flat head screw
on face C.)
4 holes evenly spaced
D=0.4 on a D=5.5 B.C.

M.I.T. GAS TURBINE LAB

VALVE CASING (part III)

TOLERANCES
(unless otherwise specified)
.X ← 0.015
.XX ← 0.010
.XXX ← 0.005

DRAWN BY:
A. FAHIM

DATE:

MATERIAL:
ALUMINUM

DATE:

SCALE:

DRAWING NO: A.5

1/5

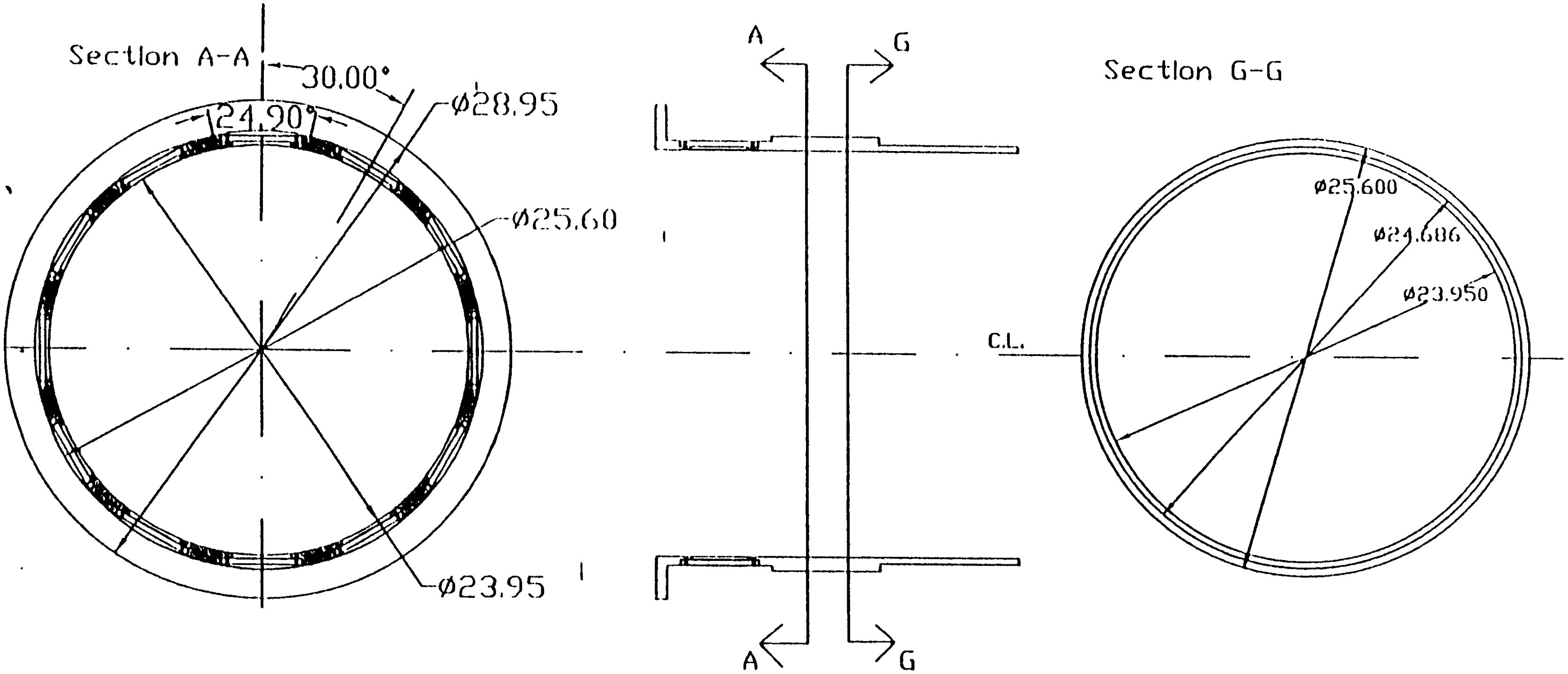
Section A-A
30.00°
Ø28.95
24.20°
Ø25.60
Ø23.95
A
G
A
G
C.L.
Section G-G
Ø25.600
Ø24.686
Ø23.950

MIT/GTL/ ACTUATION RiNG

Part: overall view	Quantity: one
Drawn by: Ahmed FAHIM	Date: 07/01/97
Design by: Ahmed FAHIM	Drawing No: GTL-140/A.6

Comments:

Projection

Material: [redacted] Aluminum

Tolerances: .x ±0.015
.xx [redacted] ±0.05
.xxx [redacted] ±0.005

Dimensions: Inches

A.6

1/5

Section A-A

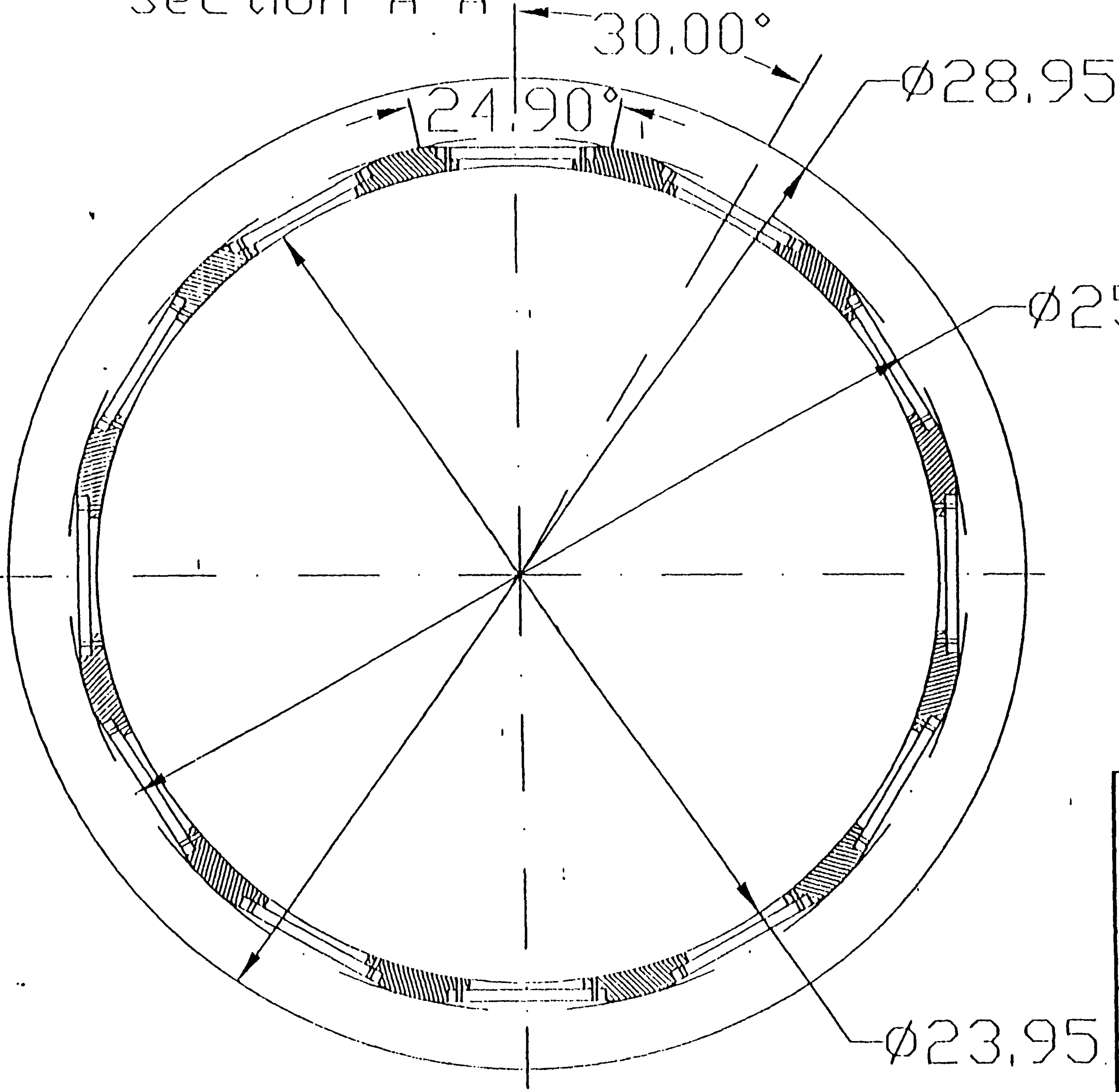

MIT/GTL/.ACTUATION RING

Part: DETAIL 1
Quantity: one

Drawn by: Ahmed FAHIM
Date: 07/01/97

Design by: Ahmed FAHIM
Drawing No: GTL-140 /A.7

Comments:

Projection:

Material: [redacted] Aluminum

Tolerances: .x ±0.015
.xx [redacted] ±0.015
.xxx [redacted] ±0.015

Dimensions: Inches

A.7

3/5

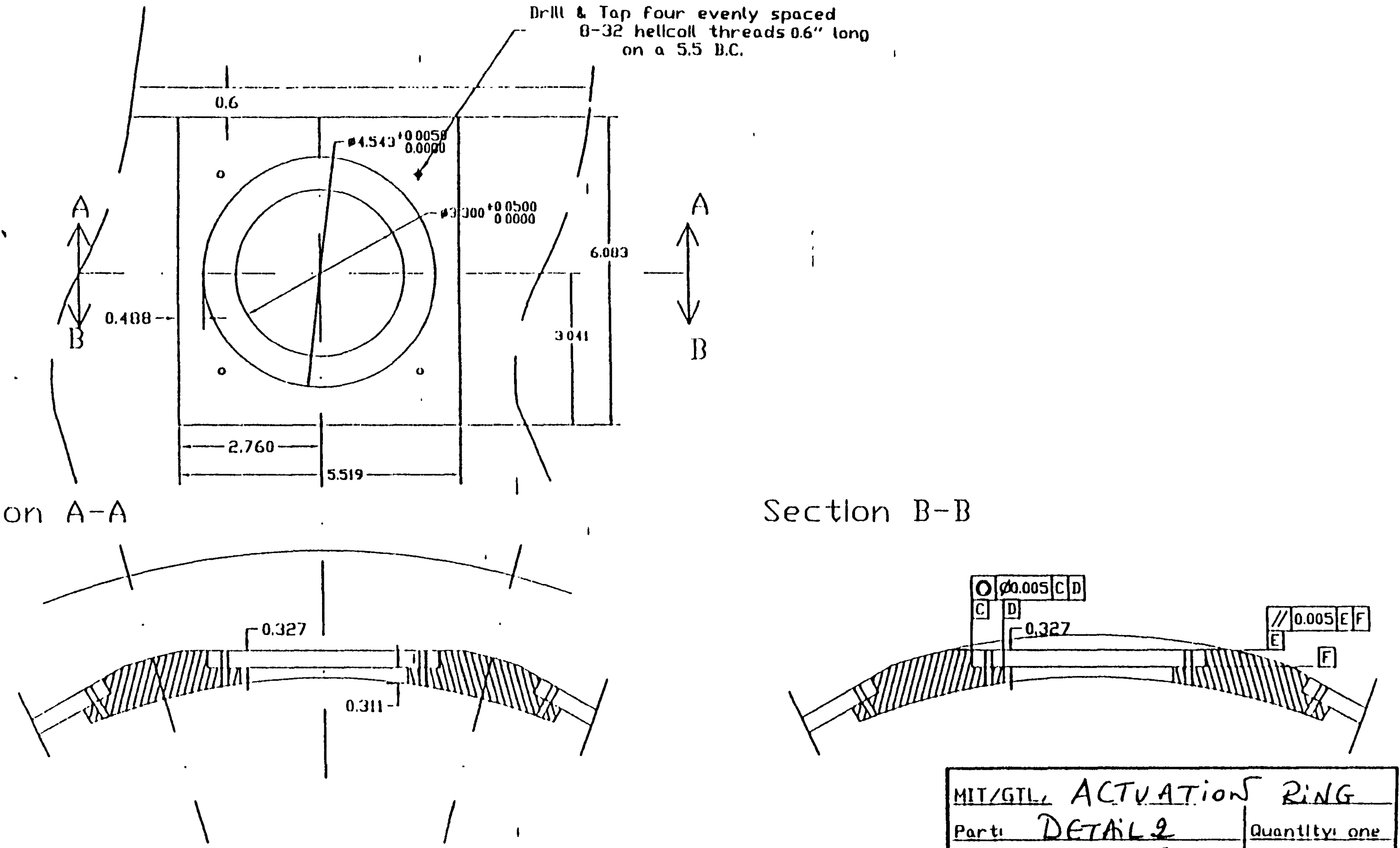

Drill & Tap four evenly spaced 8-32 helicoil threads 0.6" long on a 5.5 B.C.
0.6
ø4.543 +0.0050 0.0000
ø3.300 +0.0500 0.0000
6.083
3.041
0.488
2.760
5.519
A
B
A
B
Section A-A
Section B-B
0.327
0.311
○ ø0.005 C D
C
D
0.327
// 0.005 E F
E
F

MIT/GTL, ACTUATION RING
Part: DETAIL 2
Quantity: one
Drawn by: AHMED FAHIM
Date: 07/01/97
Design by: AHMED FAHIM
Drawing No: GTL-140/A8
Comments:

Projection

Material: Aluminum
Tolerences: .x ±0.015
.xx ±0.010
.xxx ±0.005
Dimensions: Inches

4.8

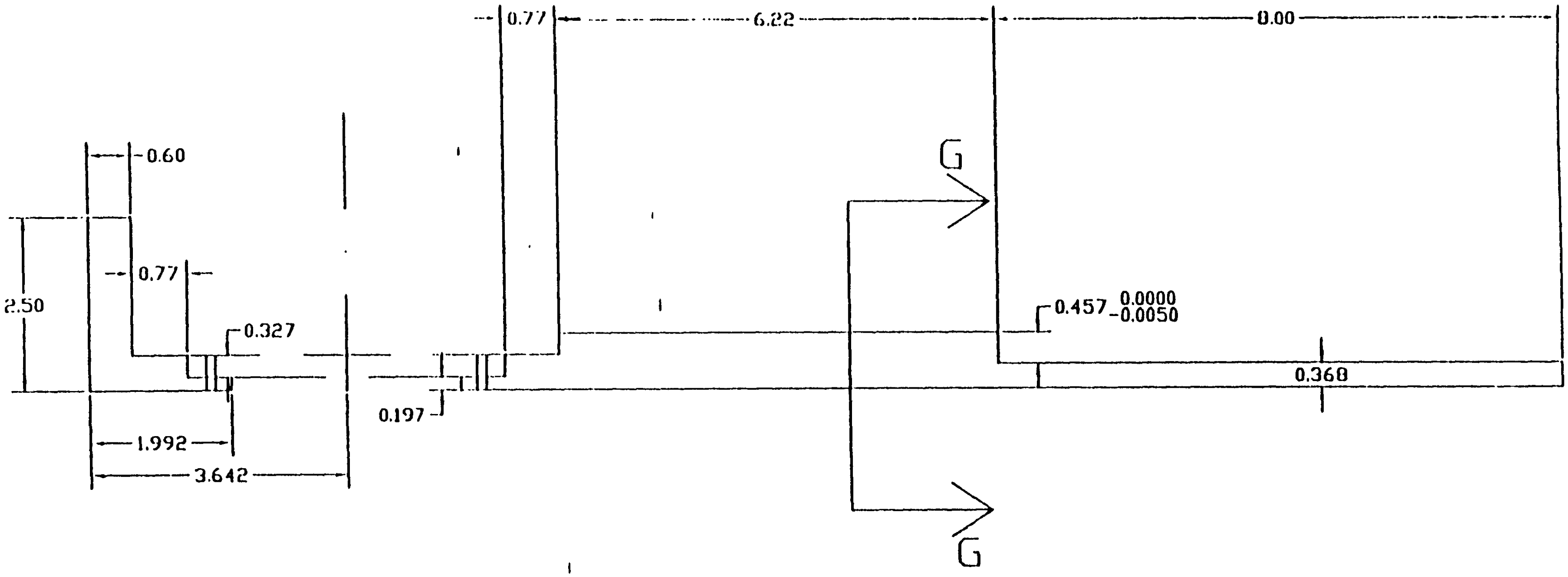
0.77
6.22
8.00
G
0.60
0.77
2.50
0.327
$0.457^{\,0.0000}_{\,-0.0050}$
0.368
0.197
1.992
3.642
G

MIT/GTL/ ACTUATION RING

Part: SIDEVIEW | Quantity: one

Drawn by: Ahmed FAHIM | Date: 07/01/97

Design by: Ahmed FAHIM | Drawing No: GTL-140 /A.9

Comments: Zoom of the sideview

Projection

Material: Aluminium

Tolerances: .x ±0.015
.xx ± 0.015
.xxx ± 0.015

Dimensions: Inches

5/5

SECTION G-G

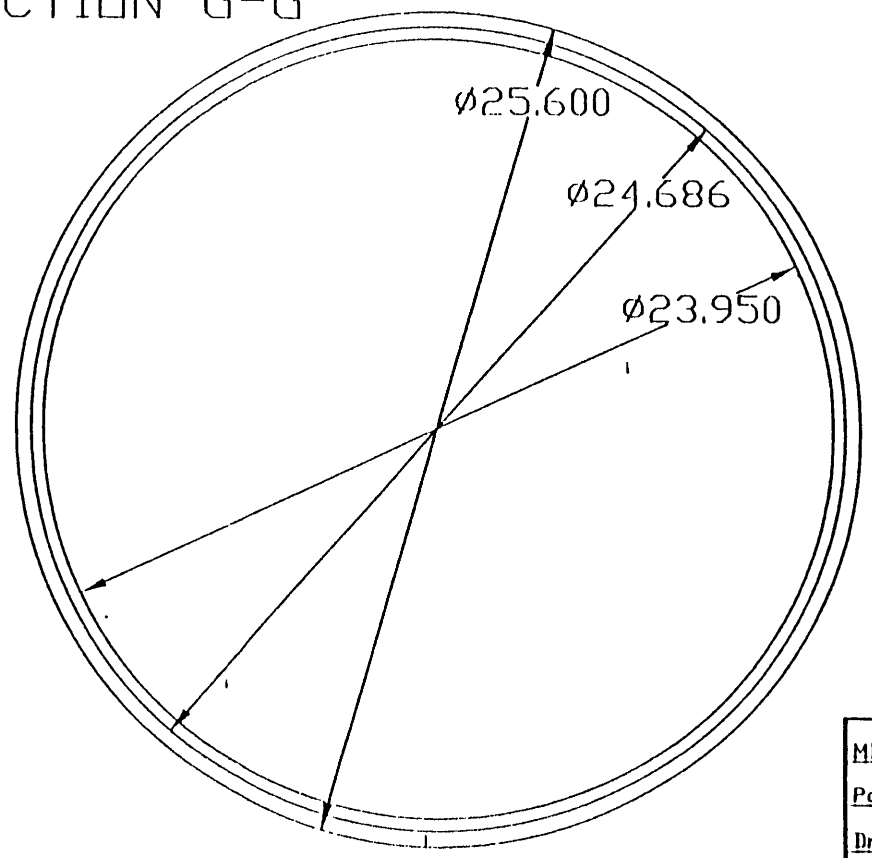

MIT/GTL/ ACTUATION RING

Part: SECTION G-G

Quantity: one

Drawn by: Ahmed FAHIM

Date: 07/01/97

Design by: Ahmed FAHIM

Drawing No: GTL-140/A.10

Comments:

Projection

Material: [redacted] Aluminium

Tolerances: .x ±0.015
.xx [redacted] ± 0.015
.xxx [redacted] ± 0.015

Dimensions: Inches

A.10

1/2

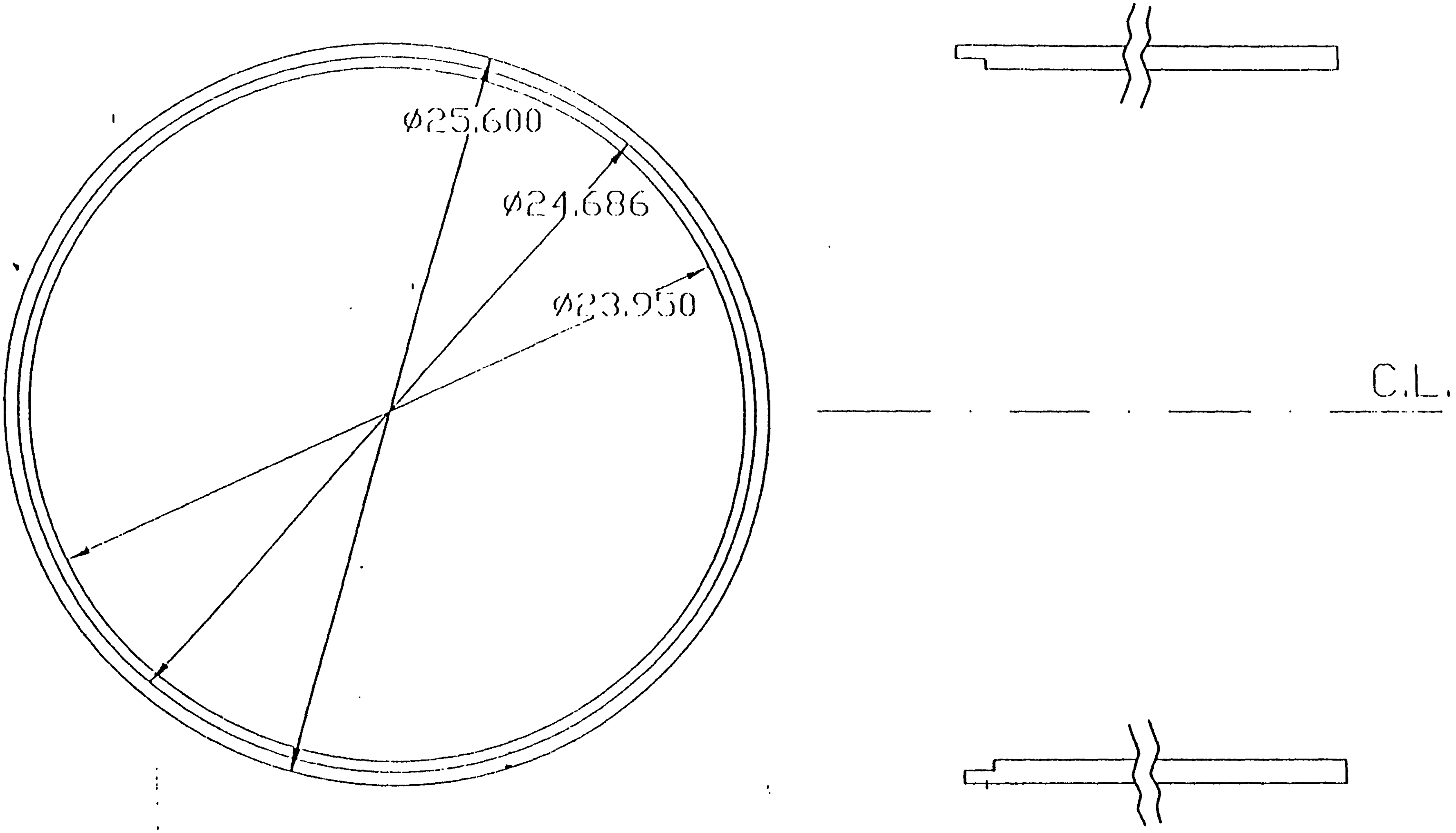

MIT/GTL/ DOWNSTREAM DUCT
Part: Outer DucT
Quantity: one
Drawn by: Ahmed FAHIM
Date: 07/01/97
Design by: Ahmed FAHIM
Drawing No: GTL-142 /A.11
Comments:

Projection
Material: Aluminum
Tolerances: .x ±0.015
.xx ± 0.015
.xxx ± 0.015
Dimensions: Inches

2/8

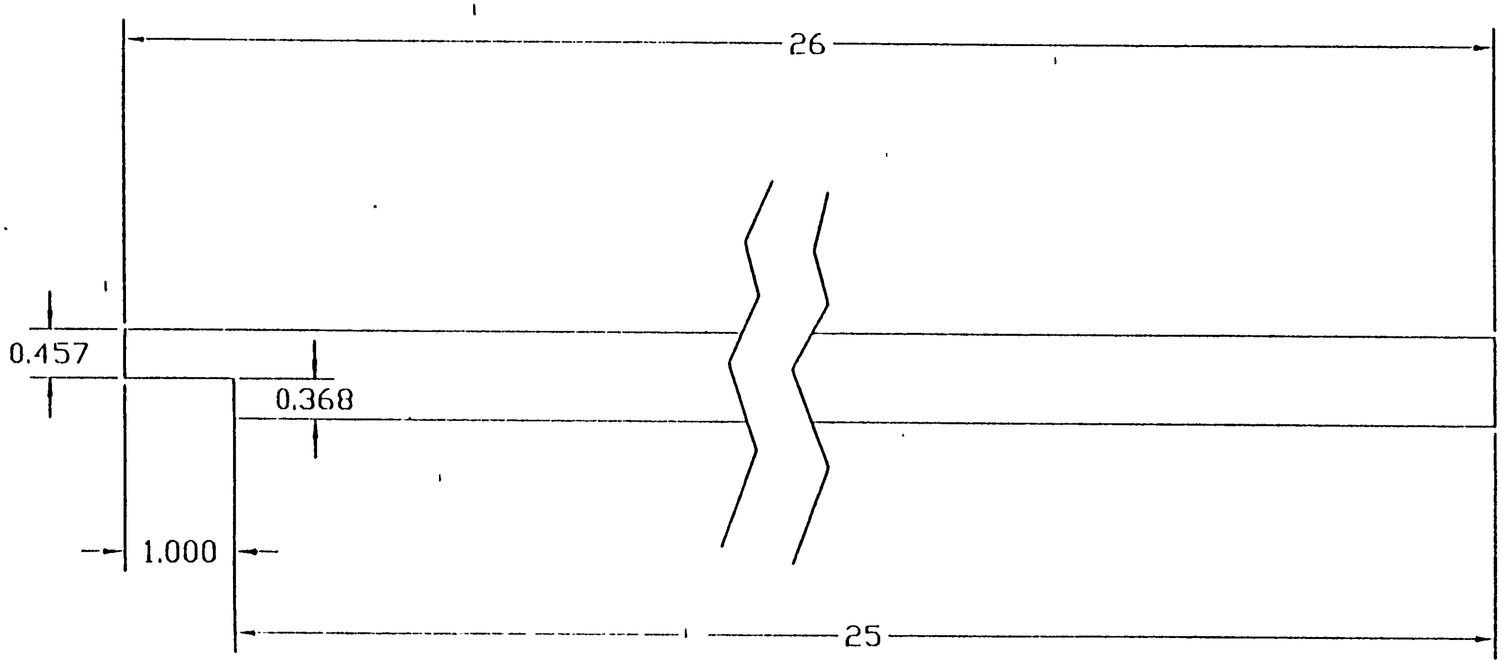

MIT/GTL/ DOWNSTREAM DUCT
Part: Outlet Duct Detail
Quantity: one
Drawn by: Ahmed FAHIM
Date: 07/01/97
Design by: Ahmed FAHIM
Drawing No: GTL-142 /A.12
Comments:

Projection
Material: ~~Steel~~ Aluminum
Tolerances: .x ±0.015
.xx ± 0.015
.xxx ± 0.015
Dimensions: Inches

H.1/2

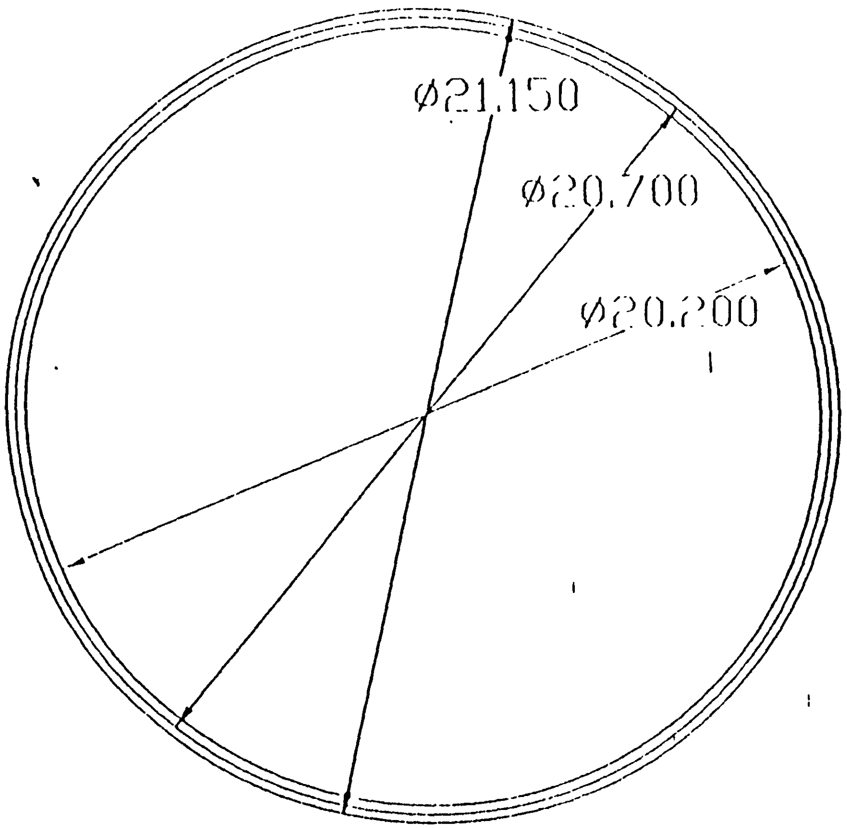
Ø21.150
Ø20.700
Ø20.200

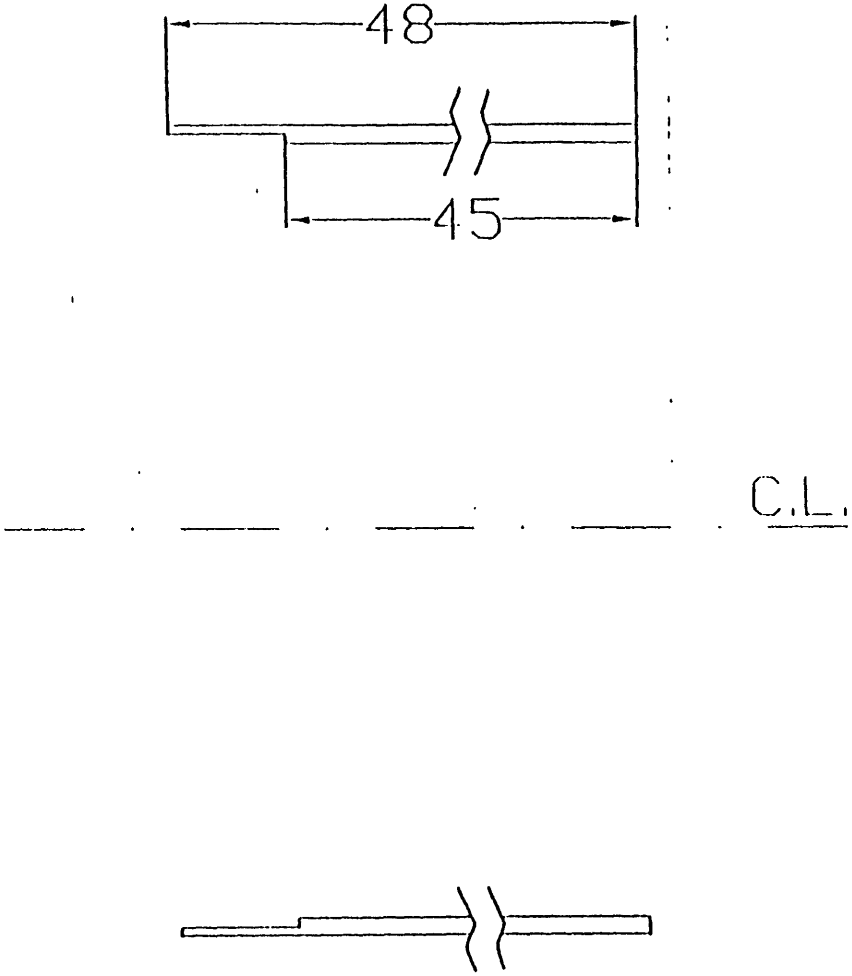

MIT/GTL/. DOWNSTREAM DUCT
Part: INNER DUCT
Quantity: one
Drawn by: Ahmed FAHIM
Date: 07/01/97
Design by: Ahmed FAHIM
Drawing NO: GTL-143/A.B
Comments:

Projection
Material: [redacted] Aluminum
Tolerances: .x ±0.015
.xx [redacted] ± 0.015
.xxx [redacted] ± 0.015
Dimensions: Inches

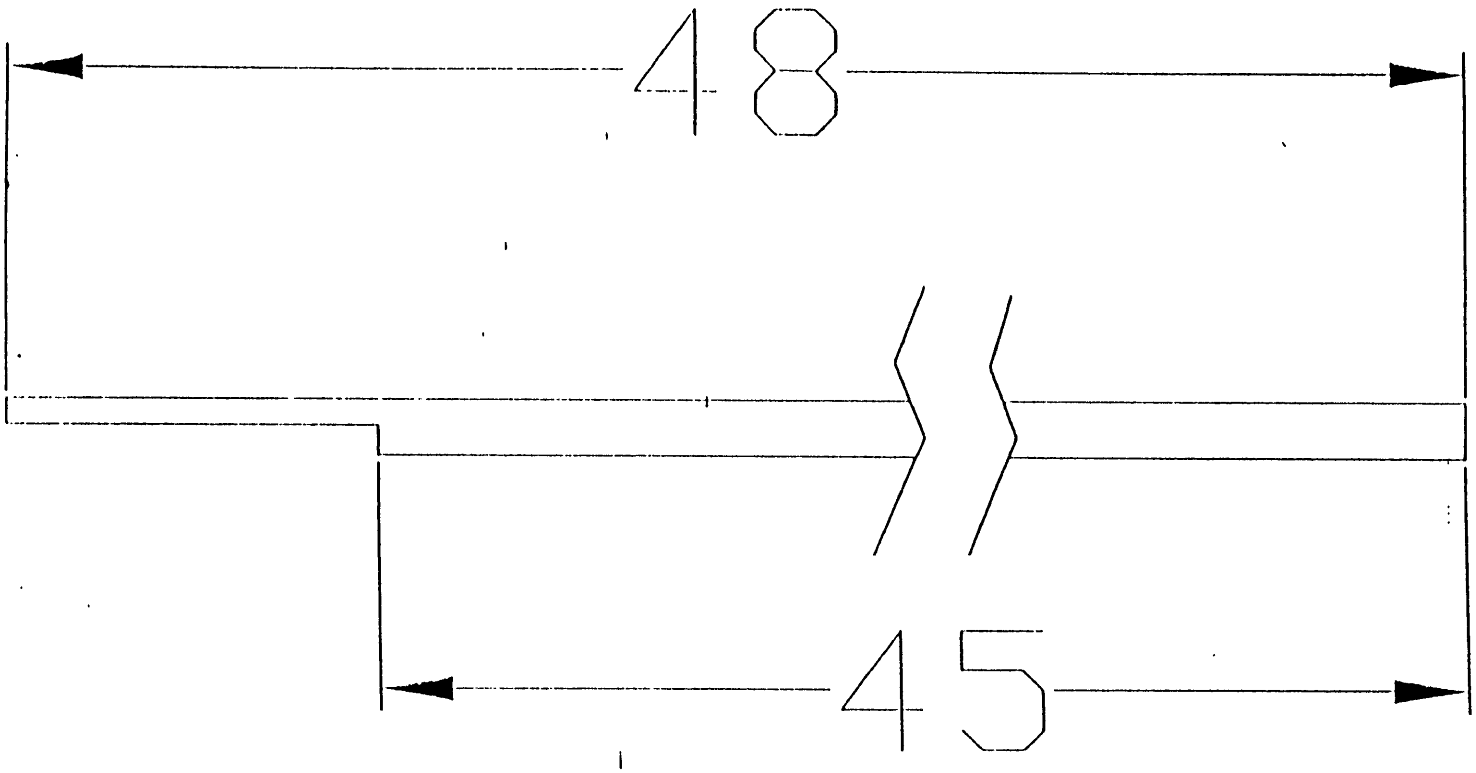

MIT/GTL: DOWNSTREAM Duct

Part: INNER Duct Detail

Quantity: one

Drawn by: Ahmed FAHIM

Date: 07/01/97

Design by: Ahmed FAHIM

Drawing No: GTL-143/A.14

Comments:

Projection

Material: Aluminum

Tolerances: .x ±0.015
.xx [illegible] ±0.005
.xxx [illegible] ±0.002

Dimensions: Inches

BIBLIOGRAPHY

[1] BERNDT, R. G. "Actuation for Rotating Stall Control of High Speed Axial Compressors". Master's thesis, Massachusetts Institute of Technology, February 1995.

[2] DIAZ, D. S. "Design of a Jet Actuator for Active Control of Rotating Stall". Master's thesis, Massachusetts Institute of Technology, May 1994.

[3] EASTLAND, A. H. J. "Investigation of Compressor Performance in Rotating Stall". GTL Report No. 164, Massachusetts Institute of Technology, June 1982.

[4] EPSTEIN, A. H., FFOWCS WILLIAMS, J. E., AND GREITZER, E. M. "Active Suppression of Aerodynamic Instabilities in Turbomachines". *AIAA Journal of Propulsion and Power, Vol. 5*, No. 2 (1989), pp. 204–211.

[5] EVEKER, K. M., GYSLING, D. L., NETT, C. N., AND SHARMA, O. P. "Integrated Control of Rotating Stall and Surge in Aeroengines". *SPIE Conference on Sensing, Actuation, and Control in Aeropropulsion* (1995).

[6] FEULNER, M. R., HENDRICKS, G. J., AND PADUANO, J. D. "Modeling for Control of Rotating Stall in High Speed Multi-Stage Axial Compressors". *Transactions of the ASME, Vol. 94-GT-200* (September 1994).

[7] GAMACHE, R. N. "Axial Compressor Reversed Flow Performance". Phd thesis, Massachusetts Institute of Technology, 1985.

[8] GARNIER, V. H. "Experimental Investigation of Rotating Stall Waves as a Rotating Stall Inception Indication in Compressors". Master's thesis, Massachusetts Institute of Technology, May 1988.

[9] GREITZER, E. M. "Surge and Rotating Stall in Axial Flow Compressors - Parts I-II". *Journal of Engineering for Power, Vol. 98*, No. 2 (April 1976), pp. 190–217.

[10] GREITZER, E. M. "The Stability of Pumping Systems - The 1980 Freeman Scholar Lecture". *Journal of Fluids Engineering, Vol. 103* (June 1981), pp. 193–242.

[11] HAYNES, J. M. "Active Control of Rotating Stall in a Three-Stage Axial Compressor". GTL Report No. 218, Massachusetts Institute of Technology, June 1993.

[12] HAYNES, J. M., HENDRICKS, G. J., AND EPSTEIN, A. H. "Active Stabilization of Rotating Stall in a Three-Stage Axial Compressor". *ASME Journal of Turbomachinery, Vol. 116*, No. 2 (April 1994), pp. 226–239.

[13] HENDRICKS, G. J., AND GYSLING, D. L. "Theoretical Study of Sensor-Actuator Schemes for Rotating Stall Control". *Journal of Propulsion and Power, Vol. 10*, No. 1 (Jan-Feb 1994), pp. 101–109.

[14] IDELCHIK, I. E. *Handbook of Hydraulic Resistance*, 3rd ed. CRC Press Ins, U.S.A., 1994.

[15] KERREBROCK, J. L. *Aircraft Engines and Gas Turbines*, 2nd ed. The MIT Press, Cambridge, Massachusetts, 1992.

[16] LAVRICH, P. L. "Time Resolved Measurements of Rotating Stall in Axial Flow Compressors". Phd thesis, Massachusetts Institute of Technology, 1996.

[17] LIAW, D., AND ABED, E. "Stability Analysis and Control of Rotating Stall".

[18] LONGLEY, J. P. "A review of non-steady flow models for compressor stability". *ASME Journal of Turbomachinery, Vol. 116* (1994), pp. 202–215.

[19] MANSOUX, C. A., GYSLING, D. L., SETIAWAN, J. D., AND PADUANO, J. D. "Distributed Nonlinear Modeling and Stabililty Analysis of Axial Compressor Stall and Surge".

[20] MOORE, F. K. "A Theory of Rotating Stall of Multistage Compressors - Parts I-II-III". *ASME Journal of Engineering for Gas Turbines and Power, Vol. 106* (April 1984), pp. 313–336.

[21] MOORE, F. K., AND GREITZER, E. M. "A Theory of Post-Stall Transients in Axial Compression systems - Parts I-II". *ASME Journal of Engineering for Gas Turbines and Power, Vol. 108* (1986), pp. 68–76;231–239.

[22] PADUANO, J. D. "Active Control of Rotating Stall in Axial Compressors". GTL Report No. 208, Massachusetts Institute of Technology, June 1993.

[23] PADUANO, J. D., EPSTEIN, A. H., VALAVANI, L., LONGLEY, J. P., GREITZER, E. M., AND GUENETTE, G. R. "Active Control of Rotating Stall in a Low-Speed Axial Compressor". *Transactions of the ASME, Vol. 115* (1993), pp. 48–56.

[24] PINSLEY, J. E. "Active Control of Centrifugal Compressor Surge". Master's thesis, Massachusetts Institute of Technology, October 1988.

[25] PROTZ, J. M. "A Four-State Galerkin Approximation to the Moore-Greitzer Compression Model". PRET working paper M95-7-15, Massachusetts Institute of Technology.

[26] PROTZ, J. M. "Nonlinear Active Control of Rotating Stall and Surge". Master's thesis, Massachusetts Institute of Technology, June 1997.

[27] SCHALKWYK, C. M. V. "Active Control of Rotating Stall with Inlet Distortion". GTL Report No. 222, Massachusetts Institute of Technology, June 1996.

[28] SETIAWAN, J. D. "Distortion Tolerance of Stall/Surge Controllers in Axial Compression Systems". Master's thesis, Massachusetts Institute of Technology, June 1996.

[29] SIMON, J. S., VALAVANI, L., EPSTEIN, A. H., AND GREITZER, E. M. "Evaluation of Approaches to Active Compressor Surge Stabilization". *Transactions of the ASME* (September 1992), pp. 1–12.

[30] Slotine, J. E., and Li, W. *Applied Nonlinear Control.* Prentice Hall, Englewood Cliffs, New Jersey, 1992.

[31] Vo, H. D. "Active Control of Rotating Stall in a Three-Stage Axial Compressor with Jet Actuators". Master's thesis, Massachusetts Institute of Technology, February 1997.

[32] Yeung, S., and Murray, R. M. "Bleed Valve Control of Rotating Stall with Continuous Air Injection on the Caltech Rig". PRET working paper C96-10-10, California Institute of Technology.

533-47